

Trinity College Dublin
Coláiste na Tríonóide, Baile Átha Cliath
The University of Dublin

IL-17 Family Members Coordinate Immunometabolic and Structural Networks

A dissertation submitted to
Trinity College Dublin, The University of Dublin
in candidature for the degree of

Doctor of Philosophy

School of Biochemistry and Immunology
Trinity Biomedical Sciences Institute
Trinity College Dublin

2026

By

Brenneth Stevens

Under the supervision of
Prof. Lydia Lynch and Prof. Tomás Ryan

Declaration

I declare that this thesis has not been submitted as an exercise for a degree at this or any other university and it is entirely my own work unless otherwise stated in the figure legends.

I agree to deposit this thesis in the University's open access institutional repository or allow the library to do so on my behalf, subject to Irish Copyright Legislation and Trinity College Library conditions of use and acknowledgement.

I consent to the examiner retaining a copy of the thesis beyond the examining period, should they so wish (EU GDPR May 2018).



Brenneth Stevens

Date: September 1st, 2025

Abstract

The interleukin-17 (IL-17) cytokine family has an established role in orchestrating barrier defense, leukocyte recruitment, and inflammatory disease. Recently, the two principal members of this family, IL-17A and IL-17F, have been shown to regulate cellular and systemic metabolism. The molecular mechanisms underpinning this immunometabolic axis are not well defined, however. Here, we used genetic, dietary, and pharmacological methods to elucidate the metabolic actions of IL-17A and IL-17F in liver and adipose tissue. IL-17A had a significant impact on carbohydrate utilization and fatty acid synthesis, effects that were most prominent during the postprandial state and following high-carbohydrate feeding. Unexpectedly, we found that biological sex was a critical determinant of IL-17's impact on thermoregulation, substrate utilization, and lipid synthesis in brown adipose tissue and liver. At the whole-body level, male *Il17a/f*$^{-/-}$ mice resisted sucrose-induced weight gain, whereas female *Il17a/f*$^{-/-}$ mice did not show protection and instead exhibited increased susceptibility in our model. Our findings highlight IL-17 as an important player in directing metabolic and immune homeostasis and raise questions regarding sex differences in these pathways.

To gain further insight on the non-canonical roles of IL-17 family members, we constructed a spatially-resolved protein interactome for the receptor subunit IL-17RC. This map, generated via high-resolution proximity proteomics, revealed an extensive network of intracellular partners with significant enrichment for proteins associated with the centrosome and mitochondrial protein complexes. The composition of this interactome pointed towards an unexplored ligand-independent

role for IL-17RC in cellular organization. This suggests that, in addition to its canonical function in cytokine signaling, IL-17RC may physically associate with the core machinery governing cytoskeletal and metabolic homeostasis, providing a new mechanistic framework for the immunometabolic functions of the IL-17 pathway.

Acknowledgements

I would like to express my deepest gratitude to my advisor, Lydia, who took a chance on a haggard musician who figured the best time for a career change was during a global shutdown. Your mentorship has been invaluable.

To Amanda, Cathal, Britta, Claire, and Aine, thank you for showing me how an immunology lab should operate. To Alecia, Ademi, and Will, thank you for some of the best times and laughs I've ever had.

I am grateful for the entire lab at Princeton, it's been a joy to get to know each of you.

To Will, your generosity and loyalty have meant more to me than you know. To the esteemed podcast host, Jaclyn, thank you simply for being such an inspiring and enjoyable person to be around. To Ayu and Alazar, I miss you both so much. To Carmine, thank you for being my most consistent link to my California home. To anyone who was forced to wade through the unending varieties of volcano plots in Chapter 4, your perseverance is noted and appreciated. To Katie and Martin, I will always appreciate your friendship, thank you for making the Boston-Princeton move infinitely more rewarding.

To Brandon, for your chemistry expertise and thoughtful suggestions. To Aaron, for your work ethic and humor. To Jonathan, my oldest friend, thank you for the decades of friendship and, of course, the music recommendations.

To Matt, Leon, and everyone else I was lucky enough to learn from in the Kirshner Lab.

To Mom and Dad, thank you for your patience, understanding, and endless support.

To Ori, thank you for being the best twin anyone could ask for.

Contents

Declaration i

Abstract ii

Acknowledgements iv

List of Figures x

List of Abbreviations xii

Contributions During the PhD xx

1 Introduction 1

1.1 The Interleukin-17 cytokine family 1

1.1.1 Origins 1

1.1.2 Evolutionary Conservation 4

1.1.3 Structural features and established signaling capacity . . . 5

1.1.4 Receptor Complexes 7

1.1.5 Downstream Signaling Pathways 8

1.1.6 Negative Feedback and Resolution 12

1.2 IL-17 at Barrier Surfaces 13

1.3 IL-17 in the field of Immunometabolism 14

1.3.1 Functions in Adipose Tissue 14

1.3.2 Roles in Liver 15
1.4 IL-17 in Neuroimmunometabolism 16
1.5 Interaction with Other Cytokines 17
1.6 Clinical Significance and Correlations with Diseases 18

2 Materials and Methods **20**

2.1 Animal models and Ethical Compliance 20
2.2 General cell culture methods 21
2.3 Cell viability and proliferation assays 21
2.4 Adipose tissue explants 22
2.5 Adipose digestion 22
2.6 Global Proteomics 23
2.7 RNA isolation for quantitative RT-PCR 24
2.8 Immunoblotting 25
2.9 RNA isolation for mRNA-Seq 26
2.10 Triacylglycerol quantification 26
2.11 In vivo metabolic analysis 27
2.12 Bacterial Culture and Plasmid Preparation 27
2.13 Immunofluorescence Staining 27
2.14 Antibody validation 28
2.15 Confocal microscopy 29
2.16 STED microscopy 29
2.17 Live-cell imaging 30
2.18 Image analysis and quantification 31
2.19 µMap proximity labeling 32
2.19.1 Photocatalyst-antibody conjugate preparation 32
2.19.2 µMap labeling on live cells 32

2.19.3 µMap labeling on fixed/permeabilized cells 33
2.19.4 Sample processing and streptavidin enrichment 34
2.19.5 Proteomics sample preparation 34
2.20 End-point PCR 35
2.21 Transfection 36
2.22 Nucleofection 37
2.23 Lentiviral transduction 37
2.24 RNA-seq analysis 38
2.25 Protein Structure Visualization 38
2.26 Statistical analysis 39

3 IL-17 cytokines influence metabolic physiology in a diet- and sex-dependent manner 41

3.1 Results 43
3.1.1 IL-17A/F deficiency is associated with altered thermoregulation and substrate utilization 43
3.2 Transcriptional Profiling Identifies De Novo Lipogenesis as a Primary Target 47
3.2.1 RNA-Seq Analysis of Brown Adipose Tissue 47
3.2.2 Temporal Dynamics of DNL Disruption 50
3.3 IL-17A regulates adipose lipogenesis in a sex-dependent manner . 53
3.4 Functional Assessment of De Novo Lipogenesis 55
3.4.1 In Vivo Flux Measurements 55
3.5 IL-17A/F Modulate the Metabolic Adaptation to Sucrose-Enriched Diets 58
3.5.1 Dietary Carbohydrate Response 58
3.5.2 Molecular Validation of DNL Defects 61

3.6 Systemic Metabolic Integration and Clinical Relevance 63
3.6.1 IL-17's influence on whole-body metabolism and physiology 63
3.6.2 Translational Relevance of the IL-17–DNL Axis in Humans 63

4 The Intracellular Interactome of IL-17RC Bridges Structural Organization and Metabolic Control 66

4.1 Introduction 66
4.2 Results 74
4.2.1 Human IL-17RC deficiency reveals unexpected non-inflammatory transcriptional dysregulation 74
4.2.2 µMap reveals unexpected intracellular protein networks . . 80
4.2.3 Microscopy illuminates IL-17RC's intracellular localization 87
4.2.4 IL-17RC ablation disrupts cytoskeletal architecture and nuclear organization 90
4.2.5 Centrosomal scaffolding defines IL-17RC's localization . . . 94
4.2.6 Ligand engagement remodels the intracellular localization of IL-17RC 95
4.3 Discussion and Conclusions 97

5 Discussion and Conclusions 100

References 106

List of Figures

Structural relationships between IL-17A, IL-17F and an archetypal neurotrophic factor 6

Molecular Mechanisms of IL-17-Mediated signaling 10

IL-17A/F deficiency alters thermoregulation and substrate utilization in a sex-dependent manner 46

Transcripts controlling lipid synthesis are significantly dysregulated in brown adipose tissue from Il17a/f and adipocyte-specific Il17rc (AdIl17rc) KO male mice 49

Lipogenic transcripts are downregulated in Il17a/f$^{-/-}$ male mice specifically during the dark cycle 52

Administration of IL-17A, but not IL-17F, induces robust expression of genes related to de novo lipogenesis in male mice 54

De novo lipogenesis is functionally impaired in the brown adipose tissue of male Il17a/f$^{-/-}$ (DKO) mice 57

IL-17A/F deficiency elicits sexually dimorphic effects on sucrose-driven weight gain 60

Sucrose fails to induce a full lipogenic response in male mice lacking IL-17A 62

IL-17 pathway blockade reduces the expression of DNL-associated genes in human psoriasis patients 65

IL-17RC expression is selectively enriched at barrier mucosa and stromal compartments 67
Protein architecture is largely conserved between human and murine IL-17RC 69
µMap workflow for identifying proximal protein networks 73
Metabolic and ECM-related transcripts are broadly dysregulated in fibroblasts isolated from IL-17RC-deficient patients 76
Silencing of Il17rc disproportionately alters mitochondrial and cytoskeletal networks 78
µMap/µMapx strategy and validation controls for the IL-17RC interactome mapping 81
The intracellular IL-17RC interactome in MEFs shows extensive overlap with centrosomal, mitochondrial and mRNA-processing networks . 83
Subcellular compartment distribution for IL-17RC interactors 86
Imaging validation of perinuclear IL-17RC localization 89
IL-17RC ablation disrupts cellular architecture 92
IL-17A/F treatment promotes rapid loss of centrosome-IL-17RC proximity 96

List of Abbreviations

Abbreviation	Definition
$^{2}H_2O$ (D_2O)	Heavy water; deuterium oxide used for metabolic flux tracing
A20 (TNFAIP3)	Ubiquitin-editing enzyme A20
ACACA (ACC1)	Acetyl-CoA carboxylase alpha; cytosolic isoform
ACACB (ACC2)	Acetyl-CoA carboxylase beta; mitochondrial isoform
ACLY	ATP-citrate lyase
ACN	Acetonitrile
ACT1 (TRAF3IP2)	NF-κB activator 1; adaptor for IL-17 receptors
AdIl17rc	Adipocyte-specific Il17rc knockout
AP-1	Activator Protein-1
Arid5a	AT-rich interactive domain-containing protein 5A (RNA stabilizer)
ARPC3	Actin-related protein 2/3 complex subunit 3
ATTO 647N	Fluorescent dye compatible with 775-nm STED
BAT	Brown adipose tissue
BCA	Bicinchoninic acid (protein assay)
BCKDHA	Branched-chain α-ketoacid dehydrogenase E1 alpha subunit

(continued on next page)

(continued from previous page)

Abbreviation	**Definition**
BCKDHB	Branched-chain α-ketoacid dehydrogenase E1 beta subunit
BSA	Bovine serum albumin
cDNA	Complementary DNA
CD36	Cluster of Differentiation 36 (fatty-acid translocase)
CDK5RAP2	CDK5 regulatory subunit-associated protein 2
CEP152	Centrosomal protein 152
CEP192	Centrosomal protein 192
ChREBP (MLXIPL)	Carbohydrate-responsive element-binding protein
ChREBP-β	Beta isoform of ChREBP
CLAMS	Comprehensive Lab Animal Monitoring System
CMV	Cytomegalovirus promoter (in expression vectors)
CPT1A	Carnitine palmitoyltransferase 1A
CXCL1	C-X-C motif chemokine ligand 1
DAPI	4′,6-Diamidino-2-phenylindole (DNA stain)
DCP1A	mRNA-decapping enzyme 1A
DEG(s)	Differentially expressed gene(s)
DESeq2	Differential expression analysis package for RNA-seq
DMEM	Dulbecco's Modified Eagle Medium
DMSO	Dimethyl sulfoxide
DNA	Deoxyribonucleic acid
DPBS	Dulbecco's phosphate-buffered saline
DTT	Dithiothreitol

(continued on next page)

(continued from previous page)

Abbreviation	**Definition**
DNL	De novo lipogenesis
ECM	Extracellular matrix
EDTA	Ethylenediaminetetraacetic acid
ELOVL6	Elongation of very long chain fatty acids protein 6
EGFR	Epidermal growth factor receptor
FACS	Fluorescence-activated cell sorting
FASN	Fatty acid synthase
FBS	Fetal bovine serum
FCS	Fetal calf serum
FDR	False discovery rate
FIJI (ImageJ)	Image processing package ("Fiji Is Just ImageJ")
GC-MS	Gas chromatography-mass spectrometry
GIGYF2	GRB10-interacting GYF protein 2
HBSS	Hanks' Balanced Salt Solution
HEK293T	Human embryonic kidney 293T cells
HEPES	4-(2-hydroxyethyl)-1-piperazineethanesulfonic acid (buffer)
HPLC	High-performance liquid chromatography
HSL (LIPE)	Hormone-sensitive lipase
IFN-β	Interferon beta
IKK	IκB kinase complex
IKKε	IκB kinase epsilon
IκBα	Inhibitor of NF-κB alpha
IκBζ (NFKBIZ)	NF-κB zeta (encoded by NFKBIZ)

(continued on next page)

(continued from previous page)

Abbreviation	**Definition**
IL-10	Interleukin-10
IL-17	Interleukin-17 (cytokine family)
IL-17A	Interleukin-17A
IL-17F	Interleukin-17F
IL-17A/F	Interleukin-17A/Interleukin-17F heterodimer
IL-17B	Interleukin-17B
IL-17C	Interleukin-17C
IL-17D	Interleukin-17D
IL-17E (IL-25)	Interleukin-17E (also IL-25)
IL-17R	Interleukin-17 receptor (family)
IL-17RA	Interleukin-17 receptor subunit A
IL-17RC	Interleukin-17 receptor subunit C
IL-17RD	Interleukin-17 receptor subunit D
IL-17RE	Interleukin-17 receptor subunit E
IL-23	Interleukin-23
IL-27	Interleukin-27
ILC	Innate lymphoid cell
ILC3	Group 3 innate lymphoid cell
IRDye	Infrared dye (LI-COR detection reagents)
KO	Knockout
LC-MS/MS	Liquid chromatography-tandem mass spectrometry
LED	Light-emitting diode
LFQ/MaxLFQ	Label-free quantification (MaxQuant algorithm)

(continued on next page)

(continued from previous page)

Abbreviation	**Definition**
LIPE (HSL)	Hormone-sensitive lipase
MAPK	Mitogen-activated protein kinase
MaxQuant	Software for quantitative proteomics
MEF(s)	Mouse embryonic fibroblast(s)
m/z	Mass-to-charge ratio
MTHFD1L	Mitochondrial 10-formyltetrahydrofolate dehydrogenase-like
MOI	Multiplicity of infection
mRNA	Messenger RNA
mRNA-seq (RNA-seq)	Messenger RNA sequencing
µMap	Microenvironment mapping (photocatalytic proximity labeling)
µMapx	Permeabilized/fixed-cell µMap variant for intracellular interactors
NA	Numerical aperture (microscopy objective)
NEFA	Non-esterified fatty acid(s)
NF-κB	Nuclear factor kappa-B
NIS-Elements	Nikon imaging software
PBS	Phosphate-buffered saline
PBST (PBS-T)	Phosphate-buffered saline with Tween-20
PCNT	Pericentrin (centrosomal protein)
PCR	Polymerase chain reaction
PEI	Polyethylenimine

(continued on next page)

(continued from previous page)

Abbreviation	**Definition**
PGC-1α (PPARGC1A)	PPARγ coactivator-1 alpha
PKLR	Pyruvate kinase, liver and RBC isoform
PMT	Photomultiplier tube
P-bodies	Processing bodies (cytoplasmic RNA granules)
PNPLA2 (ATGL)	Adipose triglyceride lipase
PVDF	Polyvinylidene difluoride (membrane)
qPCR	Quantitative PCR (reverse-transcription)
RBPs	RNA-binding proteins
RER	Respiratory exchange ratio
RIPA	Radioimmunoprecipitation assay buffer
RNA-seq	RNA sequencing
RNP	Ribonucleoprotein (e.g., Cas9-gRNA complex)
RORγt	RAR-related orphan receptor gamma t
SCARB1	Scavenger receptor class B type I
SCD1	Stearoyl-CoA desaturase-1
SDS	Sodium dodecyl sulfate
SDS-PAGE	SDS polyacrylamide gel electrophoresis
SEFIR	"Similar expression to FGF/IL-17R" domain
siRNA	Small interfering RNA
SOCS3	Suppressor of cytokine signaling 3
SREBP-1c	Sterol regulatory element-binding protein-1c

(continued on next page)

(continued from previous page)

Abbreviation	**Definition**
STAR	Spliced Transcripts Alignment to a Reference (aligner)
STAT1	Signal transducer and activator of transcription 1
STAT3	Signal transducer and activator of transcription 3
STED	Stimulated emission depletion (super-resolution microscopy)
SYBR Green	DNA-binding dye used in qPCR
TAG	Triacylglycerol
TBK1	TANK-binding kinase 1
TBS	Tris-buffered saline
TBS-T	Tris-buffered saline with Tween-20
TF	Transcription factor
Th17	T helper 17 (cell)
TIMS	Trapped ion mobility spectrometry
TLR(s)	Toll-like receptor(s)
TNF (TNF-α)	Tumor necrosis factor (alpha)
TRAF3	TNF receptor-associated factor 3
TRAF6	TNF receptor-associated factor 6
Tris-HCl	Tris(hydroxymethyl)aminomethane hydrochloride
Triton X-100	Nonionic detergent
Trypsin-EDTA	Trypsin with EDTA
TXNIP	Thioredoxin-interacting protein
Tween-20	Polyoxyethylene (20) sorbitan monolaurate (detergent)
UCP1	Uncoupling protein-1
WAT	White adipose tissue

(continued on next page)

(continued from previous page)

Abbreviation	**Definition**
WB	Western blot
WT	Wild-type
ZNF598	Zinc finger protein 598
ZT	Zeitgeber time
α	Alpha (used for isoforms, e.g., TNF-α)
β	Beta (used for isoforms)
β-TrCP	Beta-transducin repeat-containing protein (E3 ubiquitin ligase)
γδ T cell	Gamma-delta T cell
−/−	Homozygous knockout

Contributions During the PhD

1. Brennan, M., Kane, H., Healy, K., **Stevens, B**., Prendeville, H., Xu, C., McIntyre, C., Kline, J., Bamonte, B., Douglas, A., Scott, B., Temesgen, A., Azad, A., Wilk, M., Slattery, K., O'Brien, K., Koay, H.-F. & Lynch, L. (2025). TCRαβ double-negative T cells possess conserved innate features across murine tissues and promote enhanced immunogenicity in the tumor microenvironment. *Journal of Experimental Medicine* (in submission).

2. Trim, W.V., Healy, K., **Stevens, B**., Scanlan, J.G., Faust, H.J., Svensson Akusjärvi, S., O'Brien, K.L., O'Shea, D., Brenner, M.B., Heneghan, H. & Lynch, L. (2025). A transcriptional atlas defining metabolically healthy and unhealthy obesity in human adipose tissue and liver. *Cell Metabolism* (in review).

3. Kunkemoeller, B., Prendeville, H., McIntyre, C., Temesgen, A., Loftus, R.M., Yao, C., Dyck, L., Sinclair, L.V., Rollings, C., Douglas, A., Pernes, G., Mitchelson, K.A.J., Harmon, C., Raverdeau, M., Ward, R., Kane, H., Kline, J., O'Brien, K.L., Brennan, M., Smith, F., **Stevens, B**., Roche, H.M., Lavelle, E.C., Finlay, D.K., Cantrell, D.A., Chouchani, E.T., Kaech, S., Mills, E.L., Haigis, M. & Lynch, L. (2025). The source of dietary fat influences anti-tumour immunity in obese mice. *Nature Metabolism*, 7. DOI: 10.1038/s42255-025-01330-w

4. Douglas, A., **Stevens, B**., Rendas, M., Kane, H., Lynch, E., Kunkemoeller, B., Wessendorf-Rodriguez, K., Day, E.A., Sutton, C., Brennan,

M., O'Brien, K., Kohlgruber, A.C., Prendeville, H., Garza, A.E., O'Neill, L.A.J., Mills, K.H.G., Metallo, C.M., Veiga-Fernandes, H. & Lynch, L. (2024). Rhythmic IL-17 production by γδ T cells maintains adipose de novo lipogenesis. *Nature*, 636, 206–214. DOI: 10.1038/s41586-024-08131-3

5. Douglas, A., **Stevens, B**. & Lynch, L. (2023). Interleukin-17 as a key player in neuroimmunometabolism. *Nature Metabolism*, 5, 1088–1100. DOI: 10.1038/s42255-023-00846-3

6. Kane, H., LaMarche, N.M., Ní Scannail, Á., Garza, A.E., Koay, H.-F., Azad, A.I., Kunkemoeller, B., **Stevens, B**., Brenner, M.B. & Lynch, L. (2022). Longitudinal analysis of invariant natural killer T cell activation reveals a cMAF-associated transcriptional state of NKT10 cells. *eLife*, 11, e76586. DOI: 10.7554/eLife.76586

Chapter 1

Introduction

1.1 The Interleukin-17 cytokine family

1.1.1 Origins

In the early 1990's, researchers at the Centre d'Immunologie de Marseille Luminy (CIML) discovered the ancestral member of a cytokine family with evolutionarily ancient origins (Rouvier et al., 1993). Through subtractive cDNA cloning in activated T lymphocytes, Rouvier and colleagues cloned the CTLA-8 gene (now known as Interleukin-17A), whose predicted amino acid sequence was remarkably akin to the γ-herpesvirus Herpesvirus saimiri protein ORF13. This set the stage for the discovery, only two years later, of a dedicated receptor subunit (now known as IL-17RA) and the existence of a ligand–receptor pair distinct from classical cytokines (Yao et al., 1995).

Over the next decade, advances in genomic screening and homology analysis revealed IL-17A's five siblings, with IL-17B through IL-17F described in rapid succession (Li et al., 2000; Shi et al., 2000; Lee et al., 2001; Hymowitz et al., 2001; Starnes et al., 2002). Of these, IL-17A and IL-17F are the most alike, sharing more than 50% of their amino-acid makeup, and are frequently co-expressed (Hymowitz et al., 2001). This dual production was first described in $CD4^+$ T helper

17 (Th17) cells, a subset identified in the mid-2000s for their notable enrichment of IL-17A (Harrington et al., 2005; Park et al., 2005). In contrast to IL-17F, the cytokines IL-17B, IL-17C, and IL-17D, and IL-17E (known elsewhere as IL-25) show greater divergence from IL-17A, binding to distinct receptor complexes that confer specialized functions in immunity and tissue maintenance (Song et al., 2011).

For example, IL-17E (also known as IL-25) is functionally one of the most divergent members of the family (Lee et al., 2001). In contrast to IL-17A-D and IL-17F, IL-17E acts as a potent driver of Type 2 immunity, functioning as an epithelial alarmin that stimulates the expansion of group 2 innate lymphoid cells (ILC2s) and eosinophils via a heterodimeric receptor complex made up of IL-17RA and IL-17RB (Gu et al., 2013). This network supports host defense during helminth infections, yet it also contributes to allergic airway diseases and can actively subvert classical Th17 responses (Fort et al., 2001; Fallon et al., 2006; Kleinschek et al., 2007; Huangfu et al., 2023).

IL-17B mirrors IL-17E in part by signaling through IL-17RB, albeit with much lower affinity (Li et al., 2000). Owing to these altered binding kinetics, IL-17B fails to generate robust Type 2 immune responses (Lee et al., 2001). By loosely occupying its receptor without fully engaging downstream signaling, IL-17B instead functions as a competitive antagonist to IL-17E at mucosal sites, reducing IL-17E-mediated pathogenicity and neutrophil infiltration in colitis models (Reynolds et al., 2015). By contrast, IL-17B sheds this inhibitory profile within the tumor microenvironment, where it drives cell proliferation and metastasis in malignancies such as pancreatic and breast cancer (Wu et al., 2015; Huang et al., 2013).

IL-17C is derived from epithelial cells and acts in an autocrine fashion to

preserve barrier integrity (Li et al., 2000). Upon binding to the IL-17RA/IL-17RE receptor complex, this epithelial-intrinsic ligand triggers innate immune responses, including the release of antimicrobial peptides and chemokines (Song et al., 2011). These responses frequently precede lymphocyte-derived cytokine networks and can act as a critical first line of host defense (Ramirez-Carrozzi et al., 2011). When this same axis is left unchecked, however, it can precipitate diseases such as psoriasis in a manner that resembles IL-17A and IL-17F (McGeachy et al., 2019).

Finally, IL-17D represents a functional oddity within the family. *Il17d* mRNA is enriched in stromal cells and certain resting hematopoietic cells, including those found in neurological, adipose, and pulmonary tissues (Starnes et al., 2002). Moreover, CD93 has recently been demonstrated to be a functional receptor for IL-17D, an interaction that does not appear to require IL-17RA (Huang et al., 2021). By preserving ILC3-dependent mucosal defense and preventing pathogenic myeloid cell infiltration, this IL-17D-CD93 axis acts as a critical tissue checkpoint of tissue health (Huang et al., 2021; Jiang et al., 2025). Uniquely, IL-17D is induced via the Nrf2-mediated redox pathway in lieu of traditional inflammatory stimuli and effectively functions as a cellular stress sensor and modulator of antitumor surveillance (Saddawi-Konefka et al., 2016).

The physiological relevance of IL-17 extends beyond classic immunology as well. Recent discoveries suggest IL-17 cytokines can serve as metabolic messengers, coordinating energy homeostasis with environmental and nutritional cues. This broad function is observed in the regulation of feeding behavior, where circulating levels of IL-17 rise in the post-prandial period in both mice and humans, suggesting an evolutionarily conserved role in nutrient metabolism and energy allocation decisions (Nogueira et al., 2020; Peluso et al., 2012).

1.1.2 Evolutionary Conservation

The essential nature of IL-17 is not limited to mammals; early precursors regulated neuroimmune interactions and intricate behaviors in primitive metazoans (Chen et al., 2024). This long evolutionary history is traced through numerous taxa of the animal kingdom, with functional homologues found in species ranging from worms to birds to fish (Okamura et al., 2020; Min et al., 2002; Flynn et al., 2020). In the nematode worm, *C. elegans*, IL-17 homologs coordinate nutrient-seeking behaviors in response to environmental stimuli such as oxygen and salt (Chen et al., 2017). Recently, when members of this pathway were selectively ablated, central metabolic processes such as autophagy, lipid localization, and AKT/FoxO1 signaling became severely dysregulated (Singh & Aballay, 2019; Chevalier et al., 2015). Strikingly, IL-17 orthologs in nematodes not only coordinate nutrient-seeking behaviors but also appear to control glucose utilization in lieu of uptake, with IL-17.1 acting via p53 to regulate developmental progression in step with nutrient availability (Cenik et al., 2021). This metabolic gatekeeping, wherein IL-17 integrates signals of nutrient availability and allows for developmental transitions, suggests an intriguing possibility that metabolic regulation was a key ancestral role for IL-17 family, one which preceded its co-option for adaptive immunity in vertebrates.

In the Japanese medaka fish, for instance, IL-17 cytokines regulate antimicrobial peptides and influences the composition of the gut microbiota (Zhang et al., 2020; Okamura et al., 2020). Fish harboring deficient IL-17 receptor expression display reduced body weight and shorter intestinal lengths, accompanied by a robust downregulation of genes related to lipid metabolism and steroid biosynthesis (Zhang et al., 2020).

Meanwhile, a growing body of evidence demonstrates that in vertebrates and

invertebrates alike, IL-17 cytokines regulate processes that reach well beyond the scope of traditional immunology, revealing an intricate dialog between the immune system and basic physiology.

1.1.3 Structural features and established signaling capacity

IL-17 family cytokines have unique physical properties that distinguish them from other immunomodulators. IL-17A was among the first cytokines found to contain a cystine-knot tertiary structure, a complex disulfide-bonded makeup more akin to neurotrophins than classical interleukins (Hymowitz et al., 2001).

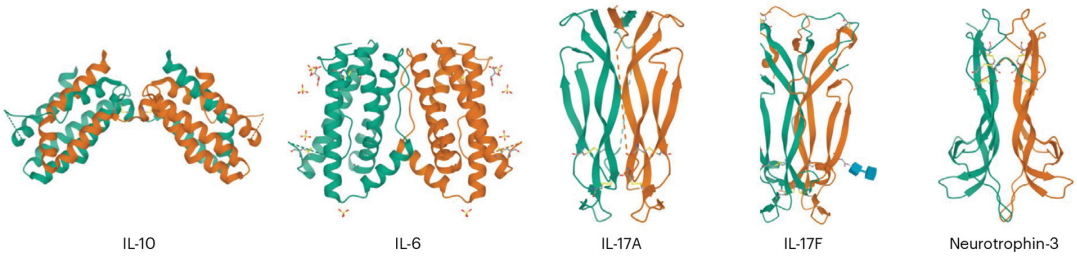


Figure 1.1: Structural relationships between IL-17A, IL-17F and an archetypal neurotrophic factor.

At the level of their 3D protein structures, IL-17A and IL-17F resemble neuronal growth factors, each adopting a similar β-sheet framework and the characteristic cystine knot motif of neurotrophins. Conversely, IL-17 cytokines are structurally distinct from prototypical interleukins, including IL-10 and IL-6. Figure designed and included for publication in “Interleukin-17 as a key player in neuroimmunometabolism” (2023) by the author of this thesis.

This motif, characterized by inter- and intra-chain disulfide bonds, stabilizes IL-17A homodimers and enhances ligand half-lives by maintaining structural stability (Liu et al., 2016; Liu et al., 2013). IL-17A and IL-17F, in particular, can form homodimers or IL-17A/F heterodimers, each of which can signal through alternate receptor complexes (Wright et al., 2007). This capacity for distinct dimeric forms increases functional diversity. When compared by their ability to induce canonical targets (e.g., IL-6 and CXCL1), IL-17A homodimers achieve the most robust responses, IL-17F homodimers are least effective, and IL-17A/F heterodimers elicit an intermediate phenotype (Wright et al., 2007; Wright et al., 2008). The other members of the IL-17 family are also cited to act as dimers but extend beyond the scope of this chapter.

1.1.4 Receptor Complexes

Interleukin-17A (IL-17A) triggers exquisitely controlled signaling events through its interactions with dimeric receptor complexes at the plasma membrane. Classical signaling is mediated by heterodimeric structures of the IL-17 receptor (IL-17R) family that comprises five diverse members named from IL-17RA to IL-17RE (Toy et al., 2006). Remarkably, IL-17RA exists as a shared receptor subunit that is used by each of the family's ligands (Wilson et al., 2022; Ramírez-Carrozzi et al. 2019).

The canonical IL-17A/F receptor complex is formed by IL-17RA and IL-17RC, a combination that is expressed predominantly on non-hematopoietic cells such as fibroblasts, keratinocytes, and epithelial cells (Toy et al., 2006; Kuestner et al., 2007). This distribution accounts for the fact that IL-17A/F signaling is largely relegated to tissue-resident cells in barrier tissues. Although IL-17RA is expressed ubiquitously throughout the body, expression of IL-17RC is more restricted, and,

as a consequence, its presence is a more accurate indicator of IL-17A/F signaling potential (Monin et al., 2018).

The signaling repertoire is expanded through non-canonical pairings of these receptors. It was recently described, for example, that IL-17A (but not IL-17F) is also capable of signaling through IL-17RA/IL-17RD heterodimeric complexes (Su et al., 2019). In mouse models of psoriasis, IL-17RA was found to functionally pair with either IL-17RC or IL-17RD in keratinocytes. Interestingly, these pairings were observed to mediate divergent biological functions: IL-17RD was unique in its control of cholesterol metabolism (at least at a transcriptional level), whereas IL-17RC mediated a more robust but qualitatively similar immune response (Su et al., 2019).

1.1.5 Downstream Signaling Pathways

The primary step in IL-17R signal transduction is the recruitment of NF-κB activator 1 (ACT1), which displays E3 ubiquitin ligase activity (Chang et al., 2006; Qian et al., 2007). ACT1 is an essential component of IL-17 receptor signal transduction, as loss of ACT1 in mice mimics the phenotype of mice lacking IL-17RA (Qian et al., 2007). Following IL-17A, IL-17F, or IL-17A/F binding, ACT1 recruits and ubiquitinates tumour necrosis factor (TNF) receptor-associated factor 6 (TRAF6), which triggers IκB kinase (IKK) activation and degrades IκBα, ultimately activating the transcription factor nuclear factor-κB (NF-κB) (Schwandner et al., 2000; Liu et al., 2009). In addition to increased NF-κB activity, TRAF6 promotes the activation of the mitogen-activated protein kinase (MAPK) intracellular pathway, which upregulates expression of the pro-inflammatory transcription factors activator protein 1 (AP-1), CCAAT/enhancer-binding protein beta (C/EBPβ) and CCAAT/enhancer-binding protein delta (C/EBPδ) (Ruddy et al.,

2004). Together, NF-κB, AP-1, C/EBPβ and C/EBPδ enhance the expression of IL-17A and IL-17F target genes. IL-17A-mediated activation of NF-κB also induces negative feedback loops that regulate NF-κB activity, which includes deubiquitinating enzymes, to end the intracellular signalling cascade. One such negative feedback loop consists of IL-17R-dependent upregulation of TANK-binding kinase 1 (TBK1) and IKKε, which phosphorylate ACT1, resulting in TRAF6 release, which inhibits IL-17 signal transduction (Paul et al., 2018).

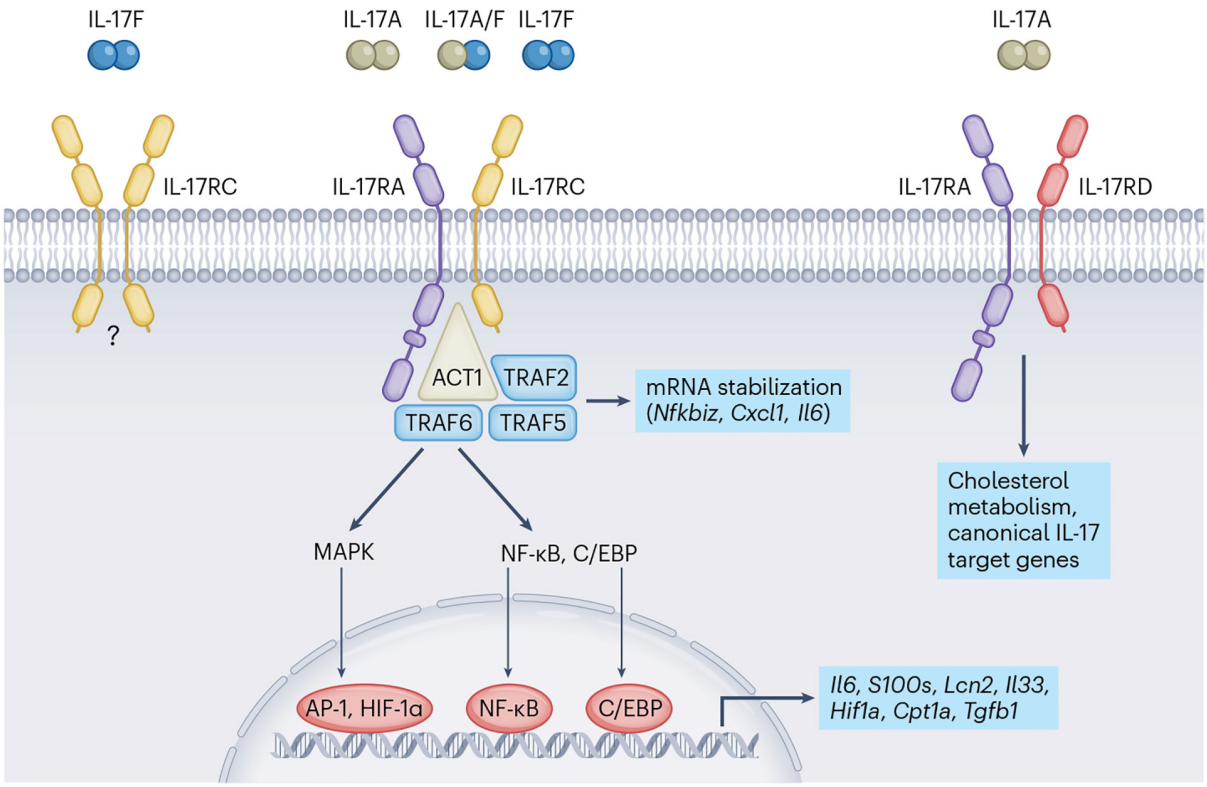


Figure 1.2 Molecular Mechanisms of IL-17-Mediated signaling

IL-17A and IL-17F initiate downstream signalling events by ligating receptor complexes composed of IL-17RA and IL-17RC. Following ligation, IL-17RA-IL-17RC recruits the adaptor protein ACT1, an essential member of the cytosolic IL-17 cascade. ACT1 in turn associates with members of the TRAF family of adaptor proteins, activating multiple transcription factors that direct inflammation, cellular metabolism and tissue repair. Additionally, IL-17 signals through TRAF2 and TRAF5 to stabilize specific mRNA targets. Figure designed and included for publication in “Interleukin-17 as a key player in neuroimmunometabolism” (2023) by the author of this thesis.

A major action of IL-17 cytokine signalling is to stabilize specific mRNA sequences (Hartupee et al., 2007). Pro-inflammatory transcripts commonly exhibit short half-lives to curb inappropriate immune responses. By modulating RNA-binding proteins (RBPs), IL-17 limits decay of select mRNAs, cooperating with transcriptional activators like TNF and IL-6 to prolong their expression. This mechanism stabilizes transcripts encoding IκBζ, a nuclear NF-κB regulator essential for IL-17A-mediated fatty acid oxidation (via Cpt1a upregulation), glucose uptake, oxidative metabolism, and cellular survival in cells such as fibroblastic reticular cells, epithelial cells, and synovial fibroblasts (Majumder et al., 2019). Similarly, it elevates C/EBPβ levels, a key IL-17 target that induces genes for choline metabolism, fatty acid transport, glucose uptake, and acts as a master regulator of adipocyte differentiation (Ruddy et al., 2004). Mechanistically, this post-transcriptional program is mediated in part by IL-17-regulated RNA-binding proteins, including Arid5a, which promotes stabilization of select IL-17 target transcripts and thereby amplifies downstream inflammatory and metabolic outputs (Amatya et al., 2018; Ahmed and Gaffen, 2010).

Beyond these transcriptional outputs, IL-17 exerts profound control over cellular bioenergetics and nutrient handling. For instance, IL-17 supports glucose uptake in fibroblastic reticular cells, an effect that requires both IκBζ and IL-17RA (Majumder et al., 2019). In a similar fashion, IL-17A and IκBζ promote oxidative metabolism in epithelial cells and synovial fibroblasts (Bechara et al., 2021; Majumder et al., 2019). In skin epithelial cells, this signaling axis induces mTOR via AKT signaling, driving HIF1α-mediated glucose uptake and glycolysis to support cell proliferation (Konieczny et al., 2022).

Critically, these metabolic and transcriptional events do not happen independently but instead require the spatial coordination of signaling machinery with

cellular organelles. The assembly of the signalosome influenced by the SEFIR domain, for example, is not simply a static process occurring at the plasma membrane. Here, engagement of ACT1 with the IL-17 receptor complex is strictly controlled by molecular chaperones such as Hsp90 that regulate the assembly and transport of the signaling network along the cytoskeleton (Bulek et al., 2011). In addition, the fact that IL-17 can stabilize specific mRNA transcripts hints at a functional relationship with the cytoplasmic machinery involved in RNA degradation (e.g., processing bodies and stress granules) (Mino et al., 2015). Although organelle-specific localization has not been classically defined for IL-17 receptors, such compartmentalization is a prominent theme in transmembrane receptor biology. In line, recent data strongly indicate that TNFR2 localizes to the inner mitochondrial membrane, where it regulates the survival of cardiac cells. Whereas the epidermal growth factor receptor (EGFR) is now known to act as a transcriptional coactivator by translocating to the cell's nucleus (Al-Lamki et al., 2001; Lin et al., 2001). The notable reliance of the IL-17 signaling complex on structural chaperones, along with its precise localization, may well indicate that this incompletely characterized network also acts as a spatial hub, one that physically intersects with mitochondrial and cytoskeletal networks to tune inflammatory responses and/or basic cellular housekeeping.

1.1.6 Negative Feedback and Resolution

To avert tissue destruction arising from uncontrolled IL-17 signaling, cells developed several negative feedback loops. IL-17R engagement quickly recruits TRAF3 to the receptor complex, where it opposes the pro-inflammatory actions of TRAF6 (Zhu et al., 2010). Deubiquitinases such as A20 and CYLD eliminate K63-polyubiquitin chains from signaling intermediates, preventing the activation

of NF-κB and MAPK pathways (Garg et al., 2013; Wang et al., 2014). At the mRNA level, IL-17-induced Regnase-1 cooperates with Roquin to degrade inflammatory transcripts, composing a feedback loop with the RNA stabilizer Arid5a to provide proper response magnitude and timing (Mino et al., 2015). Furthermore, several research groups have speculated on the existence of soluble isoforms of IL-17RC that may function as decoy receptors (Haudenschild et al., 2002). Elsewhere, the β-TrCP E3 ligase was cited to promote the degradation of Act1 itself, ensuring self-limiting signaling (Cho et al., 2011). These seemingly redundant control pathways are crucial; mouse models deficient in any one of these negative regulators exhibit increased susceptibility to autoimmune diseases due to a failure to control IL-17 signaling (Amatya et al., 2017).

1.2 IL-17 at Barrier Surfaces

At the forefront of IL-17 function are the barrier tissues (the skin, gut, lungs, and oral mucosa) where it orchestrates an active dialogue between the immune system and resident microbiota. IL-17 stimulates epithelial cells to produce antimicrobial peptides, such as β-defensins, S100 proteins, and lipocalin-2, and neutrophil-recruiting chemokines that collectively support barrier defenses (Liang et al., 2006). The commensal microbiota are necessary to temper these IL-17 responses through pattern recognition receptors and metabolites like short-chain fatty acids, which stimulate local immune cells to produce IL-17 in a steady-state, non-pathogenic context (Gaboriau-Routhiau et al., 2009; Ivanov et al., 2009). This commensal-induced IL-17 preserves epithelial integrity and restrains potentially noxious microbes while deftly preventing overt inflammation.

IL-17's essential function in host defense is particularly apparent in immunity to extracellular microbes. Humans bearing inherited loss-of-function mutations

in IL17RA, IL-17RC, or in the adaptor ACT1 exhibit chronic mucocutaneous candidiasis, presenting as recurrent infections of skin, nails, and mucosa, emphasizing IL-17's non-redundant role in antifungal immunity (Puel et al., 2011; Boisson et al., 2013; Ling et al., 2015). When this axis is perturbed, either by genetic deficiency or pathogen subversion, the host becomes extremely vulnerable to otherwise opportunistic microbes.

1.3 IL-17 in the field of Immunometabolism

1.3.1 Functions in Adipose Tissue

Members of the IL-17 family have a broad range of influences on adipose tissue physiology as well. The metabolic roles of IL-17 in adipose tissue demonstrate its function as a rheostatic regulator that maintains energetic homeostasis. Adipose tissue from IL-17-deficient mice shows profound abnormalities, including defects in sympathetic innervation and lipid mobilization. In an initial study, Zúñiga et al. described that IL-17A-deficient mice developed markedly increased weight gain compared to wild-type mice, an age- and diet-dependent phenotype that was linked to deviations in insulin and fasting glucose levels (Zúñiga et al., 2010). More recently, it was shown that$Il17a^{-/-}$ mice developed an overaccumulation of subcutaneous fat (Kohlgruber et al., 2018). IL-17 is also required for thermogenesis. Following cold exposure, adipose-resident γδ T cell-derived IL-17A directly acts on adipocytes to initiate thermogenic programs, UCP1 expression, and lipolytic enzyme activity (Kohlgruber et al., 2018). In parallel, IL-17F promotes TGF-β-driven sympathetic innervation, thus establishing thermogenic capacity on a longer-term basis (Hu et al., 2020). This dual mechanism, direct metabolic reprogramming with simultaneous structural remodeling of tis-

sue innervation, illustrates how IL-17 signaling integrates both immediate and long-term metabolic adaptations.

In line, mice with adipocyte-specific deletions of IL-17RC were unable to mount complete thermogenic responses to cold challenge. In the absence of IL-17RC, brown adipocytes produced lower amounts of TGF-β and other neurotrophic factors that stimulate sympathetic innervation of adipose tissue, with the result of profound defects in BAT innervation and catecholamine biosynthesis (Hu et al., 2020). IL-17F emerged as the primary family member to encourage this neuronal growth (Hu et al., 2020). Altogether, the IL-17 cytokine family controls adipocyte development, insulin signaling, sympathetic innervation, and metabolite partitioning in adipose tissue.

1.3.2 Roles in Liver

The liver is another key organ in which IL-17 signaling is inextricably linked with metabolism and disease. Here, elevated levels of IL-17 directly correlate with devastating states of disease, such as nonalcoholic fatty liver disease (NAFLD) and hepatocellular carcinoma (HCC) (Ma et al., 2020). In a mouse model of HCC, macrophage/Kupffer cell-specific deletion of IL-17RA stalled tumor development, an effect which was accompanied by sharp decreases in cholesterol synthesis, inflammation, and fibrosis (Shalapour et al., 2017). An even more marked decrease in tumor burden and fibrosis was observed with hepatocyte-specific deletion of IL-17RA (Shalapour et al., 2017). Consistent with these findings, a number of studies conducted in mice and humans have revealed that IL-17A-neutralizing antibodies can improve dyslipidemia and hepatic steatosis (Tang et al., 2011).

While these discoveries add to our understanding of liver pathophysiology, relatively little is known about the role of IL-17 in the regulation of hepatic

metabolism in the steady state. It is worth noting that rodent and human liver tissue alike are highly enriched for IL-17RC, which adds further credence to that idea that IL-17A and IL-17F are important regulators of normal liver function (Haudenschild et al., 2002).

1.4 IL-17 in Neuroimmunometabolism

Beyond the peripheral metabolic tissues, IL-17 signaling has become a key mediator at the nexus of neural, immune, and metabolic systems. IL-17 is constitutively expressed by meningeal γδ T cells, which in turn modulates glutamatergic signaling in cortical neurons to govern anxiety-like behaviors and the formation of short-term memories (Ribeiro et al., 2019; Alves de Lima et al., 2020). This neuromodulatory role seems to be under metabolic control, as ketogenic diet states and changes in gut microbiota composition highly impact meningeal IL-17 production (Olson et al., 2018).

The gut-brain-IL-17 axis represents one such striking example of neuroimmunometabolic integration. Specific gut microbiota, in particular segmented filamentous bacteria, promote intestinal IL-17 expression in a feeding-coupled circadian rhythm (Ivanov et al., 2009; Wang et al., 2017). This oscillating IL-17 expression synchronizes intestinal fat absorption while also regulating central nervous system functions via mechanisms that are not yet fully understood. Disruption of this axis has been implicated in disorders ranging from autism-spectrum behaviors in maternal immune activation models to metabolic dysregulation in obesity.

1.5 Interaction with Other Cytokines

IL-17A/F exhibit an intrinsically cooperative nature, and their effects are often influenced by neighboring cytokines and growth factors. This interaction generates a progressively larger set of synergistic outcomes that orchestrate immune responses with precision. One of these phenomena is the synergy between IL-17 and tumor necrosis factor (TNF) (Katz et al., 2001). While both IL-17 and TNFα each induce inflammation in their own rights, their synergy dramatically increases the expression of chemokine-, cell adhesion molecule-, and matrix metalloproteinase-encoding genes above the level induced by either cytokine alone. As discussed above, the foundation for this synergy largely lies in IL-17's ability to stabilize mRNA, which complements TNF's strong transcriptional activation of the NF-$\varkappa$B and MAPK pathways (Hartupee et al., 2007).

Other cytokines oppose IL-17-mediated inflammation. Type I interferons (such as IFN-β) and IL-10 provide two examples of mechanisms by which evolution has acted to limit IL-17-mediated inflammation. IFN-β inhibits the differentiation of pro-inflammatory Th17 cells by blocking the essential transcription factor RORγt through STAT1, while also inducing IL-27 to further antagonize the Th17 program (Fitzgerald et al., 2007; Ramgolam et al., 2009). At the same time, IL-10 signaling acts via STAT3 to directly suppress Th17 cells and induces SOCS3, blunting IL-23 activity necessary for Th17 maintenance (Chen et al., 2006). A detailed molecular grasp of these intersecting pathways will continue to provide a blueprint for the creation of better immunomodulatory therapies, each capable of restoring immune homeostasis in inflammatory disease without the dangers of broad immunosuppression.

1.6 Clinical Significance and Correlations with Diseases

Genetic investigations in humans have illuminated the IL-17/Th17 pathway's central position in immune-mediated disease. Common polymorphisms in genes that encode IL-17A, IL-17F, and their receptors have been linked to enhanced susceptibility to autoimmune and inflammatory conditions such as psoriasis, rheumatoid arthritis, and inflammatory bowel disease (Ellinghaus et al., 2013). The therapeutic success of IL-17-targeted therapies, including secukinumab and ixekizumab (IL-17A neutralizing antibodies) and brodalumab (IL-17RA blocking antibody), has firmly established the IL-23/IL-17 axis as a powerful therapeutic target, with these agents capable of inducing near-complete clearance of cutaneous lesions in a majority of patients with psoriatic disease (Langley et al., 2014; Gordon et al., 2016; Papp et al., 2012).

Despite its pathogenic tendencies in autoimmunity, the IL-17 family's evolutionary persistence arose, in part, from its ability to ward off extracellular pathogens, a role most clearly demonstrated in patients with inborn errors of IL-17 immunity who suffer from chronic mucocutaneous candidiasis (Puel et al., 2011; Boisson et al., 2013). Mechanistically, this defense relies on epithelial-neutrophil crosstalk, wherein the rapid induction of G-CSF and chemokines triggers the emergency granulopoiesis necessary to neutralize fungal pathogens like *Candida albicans* and extracellular bacteria such as *Staphylococcus aureus* and *Klebsiella pneumoniae* (Liang et al., 2006; Conti et al., 2009; Cho et al., 2010). By contrast, in the context of mycobacterial infection, IL-17 drives the formation of inducible bronchus-associated lymphoid tissue (iBALT), optimizing the level of spatial organization required for such finely tuned immune responses (Khader

et al., 2007; McGeachy et al., 2019).

Unsurprisingly, these inflammatory activities exact a trade-off. When uncoupled from microbial triggers, the same neutrophil-recruiting mechanisms that clear fungi can instead drive devastating states of immunopathology, as observed in psoriasis, ankylosing spondylitis, and multiple sclerosis (Ellinghaus et al., 2013). This context-dependent signaling is especially noticeable in the intestine. While IL-17 is a primary driver of cutaneous inflammation, it also has a beneficial role in the gut, promoting epithelial turnover and tight junction maintenance (Lee et al., 2015; Omenetti et al., 2019). As a result, while IL-17 blockade is highly effective against cutaneous and rheumatic disease, it can worsen Crohn's and colitis, highlighting the essential balance that IL-17 maintains between barrier protection and immunopathology (Hueber et al., 2012; McGeachy et al., 2019).

Chapter 2

Materials and Methods

2.1 Animal models and Ethical Compliance

The experimental work described in this thesis was conducted through a collaboration involving TCD, Brigham and Women's Hospital (Boston), and Princeton University. While the *in vivo* studies were performed in the US, the ethical framework governing this research also aligns with the regulatory requirements of TCD. Accordingly, all animal experimentation was conducted in accordance with the principles set forth in the European Union Directive 2010/63/EU on the protection of animals used for scientific purposes and the Irish Statutory Instrument No. 543 of 2012. All procedures performed at Brigham and Women's Hospital and Princeton University were reviewed and approved by their respective Institutional Animal Care and Use Committees (IACUC). These studies adhered strictly to the guidelines of the National Institutes of Health (NIH) as detailed in the *Guide for the Care and Use of Laboratory Animals*. The overarching research project was subject to ethical review by the Trinity College Dublin Animal Research Ethics Committee (AREC). Where applicable, research activities align with the project authorization terms of the Health Products Regulatory Authority (HPRA).

C57BL/6J and *Il17a*$^{-/-}$ mice were obtained from The Jackson Laboratory (Bar Harbor, ME).*Il17a/f*$^{-/-}$ mice were generously provided by Dr. Vijay K.

Kuchroo (Harvard Medical School). All animals were maintained in Specific Pathogen Free (SPF) conditions at the Harvard Institute of Medicine (Brigham and Women's Hospital) or the Lewis-Sigler Institute for Integrative Genomics (Princeton University). Mice were housed on a 12-hour light/dark cycle with *ad libitum* access to standard chow and water, unless subjected to specific dietary interventions described below.

2.2 General cell culture methods

All cell lines were maintained in humidified incubators at 37°C with 5% CO_2. Cells were routinely passaged using 0.05% trypsin-EDTA (Gibco 25300054) when reaching 80–90% confluence for adherent cells, or when density reached $1–2 \times 10^6$ cells/mL for suspension cultures. Cell counting was performed using a hemocytometer with trypan blue exclusion (0.4% trypan blue, Sigma T8154) to assess viability. Only cell preparations with $> 95\%$ viability were used for experiments. Mycoplasma contamination was tested monthly using the MycoAlert Mycoplasma Detection Kit (Lonza LT07-318) according to manufacturer's instructions. All cell lines were authenticated by short tandem repeat profiling and confirmed mycoplasma-negative before use. Culture media were replaced every 2–3 days and cells were used within 20 passages of receipt or thawing.

2.3 Cell viability and proliferation assays

Cell viability was assessed using the MTT (3-(4,5-dimethylthiazol-2-yl)-2,5-diphenyltetrazolium bromide) colorimetric assay (Sigma M5655). Cells were seeded at 5×10^3 cells per well in 96-well plates and allowed to adhere overnight. Following experimental treatments, 20 µL MTT solution (5 mg/mL in PBS) was added to each well and

incubated for 4 hours at 37°C. Media was removed and 150 µL DMSO was added to dissolve formazan crystals. Absorbance was measured at 570 nm using a microplate reader (BioTek Synergy H1). For trypan blue exclusion assays, cells were mixed 1:1 with 0.4% trypan blue and viable (unstained) cells were counted using a hemocytometer. At least 200 cells were counted per sample in duplicate.

2.4 Adipose tissue explants

Interscapular BAT was isolated, minced, and incubated in glucose-free DMEM supplemented with 10% FCS, 2.5 mM L-glutamine, and 5 mM glucose. Tissue explants were then treated with or without recombinant IL-17A (1-50 ng/mL; R&D Systems) and incubated for 18 hours at 37°C. Following media removal, explants were snap-frozen in liquid nitrogen and saved at −80°C for RNA and protein extraction.

2.5 Adipose digestion

Mice were euthanized using carbon dioxide and tissue was carefully isolated and minced in either RPMI or glucose-free DMEM. Homogenized tissues were digested in 1 mg/mL Collagenase Type II (Worthington) for 20-45 minutes at 37°C. Mature adipocytes were removed following centrifugation at 50 g and the remaining stromal vascular fraction (SVF) was washed and filtered through a 70 μm cell strainer.

2.6 Global Proteomics

Cell pellets were resuspended in 200 μl lysis buffer (8 M urea, 50 mM Tris-HCl pH 8.5, 1 mM EDTA, 1× cOmplete™ protease/phosphatase inhibitor) and sonicated on ice (3 × 10-s bursts, 30 s rest). Protein content was quantified by micro-BCA, and 50 μg total protein were reduced for 30 min at 37°C with 5 mM tris(2-carboxyethyl)phosphine (TCEP) and alkylated for 20 min in the dark with 10 mM iodoacetamide. Paramagnetic carboxylate SP3 beads (Sera-Mag SpeedBeads, hydrophilic : hydrophobic 1 : 1) were added at a 10 : 1 (w/w) bead : protein ratio, acetonitrile (ACN) was brought to 70% (v/v), and samples were incubated 10 min at 23°C with gentle agitation to capture proteins. Beads were immobilised on a magnetic rack, washed twice in 80% ethanol and once in 100% ACN, then air-dried $\leq$30 s. On-bead digestion proceeded overnight (16 h) at 37°C in 100 μl 50 mM NH_4HCO_3 containing Lys-C and trypsin (both 1 : 100 w/w to protein); the reaction was quenched with 1% (v/v) formic acid, and peptides were recovered by magnetic separation, desalted on C18 StageTips, and vacuum-dried.

Peptides (200 ng per injection) were reconstituted in 0.1% formic acid and loaded onto a 25 cm × 75 μm ID C18 column (1.6 μm, 120 Å; 50°C) coupled to an EASY-nLC 1200. Separation employed a 90-min linear gradient from 2% to 30% ACN in 0.1% formic acid at 300 nl min^{-1}, after which eluate was electrosprayed (1.7 kV) into a timsTOF Pro II (Bruker) operated in PASEF mode. Trapped-ion mobility parameters were: dual-TIMS analyzer, 100 ms accumulation/ramp, 0.60–1.60 V s cm^{-2} mobility range; each duty cycle comprised one survey MS^1 frame (m/z 100–1700) followed by ten PASEF MS/MS scans, yielding a 1.1 s cycle time. Precursors of charge state 2–5 were prioritised; collision

energies were ramped from 20 to 45 eV as a function of ion mobility, with dynamic exclusion of 0.4 min after one sequencing event. Raw data were processed in MaxQuant v3.0 with TIMS-DDA presets against the UniProt *mus musculus* reference proteome; enzyme specificity trypsin/P with two missed cleavages, fixed modification carbamidomethyl-Cys, variable modifications oxidised Met and N-terminal acetylation. False-discovery rate was controlled at 1% at PSM, peptide and protein levels using target-decoy searching, and label-free quantification was enabled (MaxLFQ, minimum ratio count = 2).

2.7 RNA isolation for quantitative RT-PCR

Cell pellets and tissues were snap-frozen in liquid nitrogen, stored at −80°C, and subsequently homogenized in Trizol (Thermo Fisher Scientific) using a TissueLyser II (Qiagen). Homogenized samples were frozen at −80°C for 1 hour and were subsequently allowed to thaw at 4°C. Chloroform was added at a 1:5 volume ratio relative to Trizol. Following centrifugation at 12,000 g, the upper aqueous layer was carefully removed and combined with 2-propanol at a 1:2 volume ratio relative to Trizol. RNA precipitates were centrifuged at 12,000 g, 2-propanol was discarded, and pellets were washed twice with ice-cold ethanol. RNA precipitates were allowed to dry before solubilization in molecular biology grade Tris-EDTA (Sigma-Aldrich; pH 8.0). RNA purity and concentrations were estimated using a NanoDrop 2000 UV spectrophotometer (Thermo Fisher Scientific). Only samples with A_{260}/A_{280} ratios between 1.8–2.2 and A_{260}/A_{230} ratios > 1.8 were used for downstream applications.

Complementary DNA synthesis was performed using the High-Capacity cDNA Reverse Transcription Kit (Applied Biosystems 4368814) according to manufacturer's specifications. Quantitative PCR was performed using PowerUp SYBR

Green Master Mix (Applied Biosystems A25742) on a QuantStudio 6 Flex Real-Time PCR System (Applied Biosystems). Primer specificity was confirmed by melt curve analysis and gel electrophoresis. Relative gene expression was calculated using the ΔΔCt method with normalization to multiple reference genes including Ppib (peptidylprolyl isomerase B), Rpl27 (ribosomal protein L27), and Actb (β-actin). Technical triplicates were performed for each biological sample, and no-template controls were included in each run. Primer efficiencies were validated to be between 90-110% using standard curve analysis.

2.8 Immunoblotting

Samples were lysed in 1X SDS sample buffer (50 mM Tris-HCl pH 6.8, 2% SDS, 10% glycerol, 1% β-mercaptoethanol, 12.5 mM EDTA, 0.02% bromophenol blue) supplemented with protease and phosphatase inhibitors. Lysates were briefly sonicated to shear genomic DNA, heated to 95°C for 5 min, and centrifuged at 14,000 g for 10 minutes. Protein samples were resolved by SDS-PAGE using 4-12% Bis-Tris gels under reducing conditions, alongside prestained molecular weight markers. Proteins were transferred to nitrocellulose membranes using a wet transfer system in transfer buffer (25 mM Tris, 192 mM glycine, 20% methanol) at either 100V for 1 h at 4°C or 30V overnight at 4°C.

Following protein transfer, membranes were dried at room temperature for 1 h to maximize protein retention. Nitrocellulose membranes were rehydrated in TBS for 5 min. Membranes were blocked with Intercept Blocking Buffer (LI-COR) for 1 h at room temperature with gentle agitation. Primary antibodies were diluted in Intercept T20 Antibody Diluent and incubated with membranes overnight at 4°C. After washing four times with TBS-T (TBS containing 0.2% Tween 20), membranes were incubated with IRDye 800CW or 680RD secondary antibodies

(1:20,000) or VRDye secondary antibodies (1:10,000) in Intercept T20 Antibody Diluent for 1 h at room temperature. For PVDF membranes, SDS (0.01-0.02%) was added to the secondary antibody solution. Membranes were washed four times with TBS-T, rinsed once with TBS, and imaged using an Odyssey Imaging System (LI-COR). For multiplexed detection, primary antibodies from different host species were co-incubated, followed by species-specific secondary antibodies labeled with spectrally distinct fluorophores.

2.9 RNA isolation for mRNA-Seq

Tissues were snap-frozen in liquid nitrogen, stored at -80°C, and subsequently homogenized in 1 mL Trizol (Thermo Fisher Scientific) using a TissueLyser II (Qiagen). Homogenates were frozen overnight at -80°C. Samples were thawed at 4°C and 200 µL Chloroform was added. Following centrifugation at 12,000 g and extraction of the aqueous layer, RNA was isolated using the RNeasy Mini Kit (Qiagen) according to the manufacturer's specifications.

2.10 Triacylglycerol quantification

Tissues were carefully weighed and homogenized in 5% IGEPAL CO-630 (Sigma-Aldrich) using a TissueLyser II. Samples were heated in an 85°C water bath for 3 minutes and allowed to cool to 23°C. Following a second heating cycle, samples were diluted and background glycerol levels and liberated triacylglycerol concentrations were evaluated using the Triglyceride Quantification Colorimetric/Fluorometric Kit (Sigma-Aldrich).

2.11 In vivo metabolic analysis

Indirect calorimetry was performed using the comprehensive lab animal monitoring system (CLAMS) system as previously described. Mice were acclimatized for a minimum of twelve hours in single-animal cages and rates of oxygen consumption, energy expenditure, carbon dioxide emission, food intake, and water intake were measured. CalR was used for data analysis according to the developer's specifications.

2.12 Bacterial Culture and Plasmid Preparation

Plasmid-containing bacteria from stab cultures were streaked onto LB-ampicillin (100 µg/mL) plates and incubated overnight at 37°C. Single colonies were selected and grown in LB-Lennox broth supplemented with ampicillin (100 µg/mL) at 37°C with shaking (220 rpm). Plasmid DNA was isolated using a QIAprep Spin Miniprep Kit according to manufacturer's instructions. All plasmids were verified by sequencing (via Plasmidsaurus).

2.13 Immunofluorescence Staining

Cells were cultured on No. 1.5 glass coverslips (22 × 22 mm) and fixed for 10 minutes at 23°C in 4% (w/v) paraformaldehyde (PFA) prepared freshly in HBSS supplemented with 1% BSA. For preservation of tubulin and related structures, an alternative fixative containing 3% PFA and 0.1% glutaraldehyde in HBSS and 1% BSA was used for the same duration. Residual aldehydes were quenched for 10 min in 100 mM glycine in PBS, after which cells were permeabilized for 5-10 minutes at 23°C with 0.1% (v/v) Triton X-100 in HBSS and rinsed 3x in HBSS.

Non-specific binding sites were blocked for 60 min at 23°C in either 3% (w/v) bovine serum albumin in PBS or 10% (v/v) normal serum from the secondary-antibody host species, each supplemented with 0.05% (v/v) Tween-20. Primary antibodies were diluted in their corresponding blocking buffer according to in-house titration experiments and/or manufacturer recommendations and incubated for 1 h at 23°C or overnight at 4°C in a humidified chamber. After 3x 5-min washes in HBSS containing 0.05% Tween-20, fluorophore-conjugated secondary antibodies were added for 60 min at 23°C. F-actin was stained with phalloidin conjugates for 20 minutes, and nuclei were counterstained with either 1 μg mL^{-1} DAPI or Hoechst 33342 for 20 minutes. Coverslips were mounted in either Prolong Glass or Prolong Diamond (Thermo Fisher Scientific) and allowed to set for at least 36 h before imaging.

2.14 Antibody validation

Primary antibodies were validated for specificity using multiple approaches. The mouse anti-murine IL-17RC antibody (R&D Systems) was validated by comparing staining in wild-type versus*Il17rc*$^{-/-}$ knockout cells or tissues when available. Secondary antibody specificity was verified by omitting primary antibodies in control samples. For western blot applications, antibodies were validated by confirming expected molecular weights and by siRNA-mediated knockdown where feasible. Cross-reactivity was assessed by comparing staining patterns between species-matched isotype controls and experimental antibodies. Only antibodies showing specific staining patterns with minimal background were used for quantitative analyses.

2.15 Confocal microscopy

Confocal fluorescence microscopy was performed using either a Lionheart FX automated microscope (BioTek) or a Nikon A1 R confocal laser scanning microscope. For the Lionheart FX system, samples were imaged using LED excitation with appropriate filter cubes and a 20× or 40× Plan Fluor objective. For the Nikon A1 R system, imaging was performed with a 60× or 100× oil immersion objective (NA 1.4) and photomultiplier tube (PMT) detectors. Sequential acquisition was employed to prevent spectral bleed-through between fluorescent channels. DAPI was excited at 405 nm and emission collected between 415-480 nm. Alexa Fluor 488 or FITC was excited at 488 nm with emission collected between 498-550 nm. Alexa Fluor 568 or similar red fluorophores were excited at 552 nm with emission collected between 562-650 nm. Alexa Fluor 647 was excited at 638 nm with emission collected between 648-750 nm. Pixel size was maintained at 50-70 nm with 4× line averaging and sequential frame acquisition. Z-stacks were acquired with 200 nm step intervals when volumetric analysis was required. Images were acquired using identical laser power settings, gain, and exposure times within each experiment to enable quantitative comparisons. Post-acquisition processing included deconvolution when appropriate and maximum intensity projections or orthogonal views were generated using ImageJ/FIJI (v2.3.0).

2.16 STED microscopy

Super-resolution stimulated emission depletion (STED) microscopy was performed using a Nikon A1 R confocal system equipped with an Abberior STED module. Samples were prepared on high-precision No. 1.5H coverslips (170 ± 5 μm thick-

ness) and mounted using ProLong Diamond antifade medium. A 100× oil immersion objective (NA 1.4) was used for all acquisitions. The Abberior STED system provided 775 nm depletion laser for super-resolution imaging. Fluorophores were selected based on STED compatibility: Alexa Fluor 594, ATTO 647N, and Star RED were used with 775 nm STED depletion. STED laser power was optimized for each fluorophore (typically 10–40% of maximum power) to achieve optimal resolution enhancement while minimizing photobleaching. Pixel size was set to 15–20 nm with time gating applied to enhance resolution. Images were processed using NIS-Elements software and resolution assessment was performed using fluorescent beads (40 nm TetraSpeck, Thermo Fisher Scientific) to confirm achievement of sub-100 nm lateral resolution.

2.17 Live-cell imaging

Live-cell microscopy was performed using a Lionheart FX automated microscope (BioTek) equipped with environmental control maintaining 37°C, 5% CO_2, and humidified atmosphere. Cells were seeded on 96-well imaging plates or 35 mm glass-bottom imaging dishes 24–48 hours prior to imaging. Growth medium was replaced with phenol-red free DMEM (Gibco) supplemented with 10% FBS and 25 mM HEPES buffer 30 minutes before imaging commenced. Time-lapse acquisition was performed using 4×, 10×, or 20× Plan Fluor objectives with images captured every 5–15 minutes for up to 24 hours. LED illumination was used with appropriate filter cubes and neutral density filters to minimize phototoxicity. For fluorescent protein tracking, exposure times were maintained below 100 ms per channel. Z-stacks spanning 10–15 μm were acquired when three-dimensional tracking was required. Image analysis was performed using Gen5 software (BioTek) and ImageJ/FIJI with the TrackMate plugin for automated

cell tracking and manual verification of track accuracy.

2.18 Image analysis and quantification

Confocal microscopy images were analyzed using Nikon NIS-Elements software (version 5.30.00) for initial processing and measurements, or Gen5 software (version 3.09, Agilent BioTek) for automated imaging data. Background subtraction was performed using rolling ball algorithms with appropriate radius settings determined empirically for each imaging session. For quantitative analysis of cellular parameters, images were exported as TIFF files and analyzed using CellProfiler (version 4.2.8). Object identification pipelines were established to segment nuclei using DAPI staining and cell boundaries using appropriate cytoplasmic markers or transmitted light images. Object-level and cell-level measurements including fluorescence intensity, area, shape parameters, and colocalization coefficients were extracted using standardized CellProfiler pipelines.

For immunofluorescence quantification, regions of interest were defined based on cellular compartments and fluorescence intensities were measured after background subtraction. Colocalization analysis was performed using Pearson's correlation coefficients and Manders' overlap coefficients. All quantitative analyses were performed on raw, unprocessed images with identical acquisition parameters within each experiment. For live-cell imaging data, cellular tracking and migration analysis were performed using the TrackMate plugin in ImageJ/FIJI, with manual verification of automated tracking results. A minimum of 50 cells per condition were analyzed across at least three independent experiments unless otherwise stated.

2.19 µMap proximity labeling

2.19.1 Photocatalyst-antibody conjugate preparation

Goat anti-mouse IgG secondary antibody (150 μL of 2.0 mg/mL, Millipore AP124) was combined with 15 μL of 1.0 M $NaHCO_3$ and 10 μL of 10 mM azidobutyric acid NHS ester (Enamine EN300-265680) in DMSO. The mixture was incubated for 1.5 hours at room temperature with gentle agitation. Following incubation, the reaction mixture was passed through a Zeba 40 kDa 2 mL desalting column equilibrated with 50 mM Tris-HCl (pH 8.0). The desalted antibody solution (ca. 200 μL) was then treated with 8 μL of 5.0 mM iridium photocatalyst in DMSO, followed by addition of Click-iT kit components (Thermo Fisher C10276): 50 μL reaction buffer A, 20 μL $Cu(OAc)_2$, and 20 μL additive 1. The mixture was incubated for 5 minutes, then 30 μL additive 2 was added and incubated in the dark for 30 minutes. The conjugation reaction was purified using a DPBS-equilibrated desalting column to yield approximately 250 μL of photocatalyst-antibody conjugate. Final protein concentration was determined by BCA assay and photocatalyst loading assessed by A_{350} measurement, typically achieving 6–10 photocatalysts per antibody.

2.19.2 µMap labeling on live cells

Cells were harvested during log-phase growth and washed twice in cold DPBS before resuspension at the appropriate density. For IL-17RC targeting, cells (5-50 million depending on experiment) were pelleted at 1,000×g for 4 minutes at 4°C and resuspended in 1 mL cold DPBS containing 5-25 μg mouse anti-murine IL-17RC primary antibody (R&D Systems). Cells were incubated on a rotisserie for 30 minutes at 4°C, then pelleted and washed twice with 1 mL

cold DPBS. Following primary antibody incubation, cells were resuspended in 1 mL cold DPBS containing 5-25 μg photocatalyst-conjugated goat anti-mouse secondary antibody and incubated for 30 minutes at 4°C with rotation. After two additional washes with cold DPBS, cells were resuspended in 1 mL cold DPBS containing 250 μM diazirine-biotin probe. Samples were immediately placed in a PennOC Photoreactor M1 and irradiated with 450 nm light at 100% intensity for 2-10 minutes. Following irradiation, cells were pelleted and washed twice with cold DPBS before lysis and streptavidin enrichment.

2.19.3 µMap labeling on fixed/permeabilized cells

For fixed cell µMap experiments, cells were first fixed with 4% paraformaldehyde in DPBS for 10 minutes at room temperature, then washed three times with DPBS. Cells were permeabilized using 0.1% Triton X-100 in DPBS for 10 minutes at room temperature, followed by three washes with DPBS. Fixed and permeabilized cells were blocked with 3% BSA in DPBS for 60 minutes at room temperature. Primary antibody incubation was performed using mouse anti-murine IL-17RC (R&D Systems) diluted in blocking buffer for 1 hour at room temperature or overnight at 4°C. Following three washes with DPBS containing 0.05% Tween-20, cells were incubated with photocatalyst-conjugated secondary antibody in blocking buffer for 60 minutes at room temperature. After washing, cells were resuspended in DPBS containing 250 μM diazirine-biotin probe and subjected to photolabeling as described for live cells. The fixed cell approach allowed for enhanced antibody penetration and reduced background labeling compared to surface-only labeling in live cells.

2.19.4 Sample processing and streptavidin enrichment

Following photolabeling, cell pellets were lysed in RIPA buffer (Thermo Fisher 89900) supplemented with 1% SDS and 1× protease inhibitors (Sigma-Aldrich 11873580001). Lysates were sonicated briefly to shear genomic DNA, heated at 95°C for 5 minutes, then centrifuged at 14,000×g for 10 minutes. Protein concentration was determined by BCA assay. For streptavidin enrichment, 1-1.2 mg total protein was incubated with 250 μL pre-washed streptavidin magnetic beads (Thermo Fisher 88817) for 3 hours at room temperature with rotation. Beads were washed sequentially with 1% SDS in DPBS (3×), 1 M NaCl in DPBS (3×), and 10% ethanol in DPBS (3×), with 5-minute incubations for each wash. Proteins were eluted by heating beads in 4× Laemmli sample buffer containing 20 mM DTT and 25 mM biotin at 95°C for 10 minutes. Eluates were analyzed by SDS-PAGE and western blotting using IRDye 800CW streptavidin (LI-COR 926-32230) for biotinylation detection.

2.19.5 Proteomics sample preparation

For mass spectrometry analysis of µMap-enriched proteins, streptavidin magnetic beads were processed using an on-bead digestion protocol. Following the standard washing procedure described above, beads were resuspended in 8 M urea, 50 mM Tris-HCl (pH 8.5), 1 mM EDTA, and protease/phosphatase inhibitors (cOmplete™, Roche). Proteins were reduced with 5 mM tris(2-carboxyethyl)phosphine (TCEP) for 30 minutes at 37°C, then alkylated with 10 mM iodoacetamide for 20 minutes in the dark at room temperature. Excess iodoacetamide was quenched with additional 5 mM TCEP for 15 minutes.

For proteolytic digestion, beads were washed three times with 50 mM ammonium bicarbonate to remove urea. On-bead digestion was performed with

sequencing grade trypsin (Promega V5111) at a 1:50 protease-to-protein ratio in 50 mM ammonium bicarbonate at 37°C overnight with gentle agitation. The digestion was quenched with 0.5% formic acid, and peptides were collected in the supernatant after magnetic separation.

Peptide cleanup was performed using C18 stage tips or Pierce C18 spin columns (Thermo Fisher 89870). Briefly, peptides were acidified to pH <3 with trifluoroacetic acid, loaded onto pre-conditioned C18 material, washed with 0.1% formic acid, and eluted with 60% acetonitrile, 0.1% formic acid. Eluates were dried in a SpeedVac concentrator and resuspended in 0.1% formic acid for LC-MS/MS analysis. Peptide concentrations were estimated using the Pierce Quantitative Colorimetric Peptide Assay (Thermo Fisher 23275) prior to injection.

2.20 End-point PCR

PCR amplification of CRISPR-edited loci was performed using Phusion High-Fidelity DNA Polymerase (Thermo Fisher Scientific) according to the manufacturer's recommendations. Briefly, genomic DNA was extracted from clonal populations using QuickExtract DNA Extraction Solution (Lucigen) or standard phenol-chloroform extraction. PCR reactions contained 1× Phusion HF Buffer, 200 µM dNTPs, 0.5 µM forward and reverse primers flanking the predicted cut site, 0.02 U/µL Phusion polymerase, and 10-50 ng template DNA in a final volume of 25 µL. Thermal cycling conditions consisted of initial denaturation at 98°C for 30 seconds, followed by 30 cycles of 98°C for 10 seconds, primer-specific annealing temperature for 15 seconds, and 72°C extension for 30 seconds per kilobase of expected product, with a final extension at 72°C for 5 minutes. PCR products were resolved by agarose gel electrophoresis, excised, and purified using a QIAquick Gel Extraction Kit (Qiagen). Purified amplicons were subjected to

linear PCR sequencing using the same primers employed for initial amplification through Plasmidsaurus sequencing services to confirm successful genomic editing and characterize insertion/deletion events at the target locus.

2.21 Transfection

Cells were cultured in DMEM supplemented with 10% (v/v) fetal bovine serum and 1% (v/v) penicillin–streptomycin and maintained at 37°C and 5% CO_2. Twenty-four hours before transfection, cultures were seeded at a density to yield 60–80% confluence on the day of reagent delivery.

Immediately before transfection, growth medium was replaced with an equivalent volume of antibiotic-free DMEM containing serum. Transfection complexes were assembled in Opti-MEM according to the manufacturer's guidelines. Briefly, plasmid DNA, duplex siRNA, or CRISPR ribonucleoprotein (RNP) complexes were paired with Lipofectamine 2000, Lipofectamine RNAiMAX, or Lipofectamine CRISPRMAX, respectively.

Nucleic acid or RNP and lipid solutions were prepared separately, combined in equal volumes, mixed gently, and incubated for 10–15 min at room temperature to allow complex formation. Complexes were then added dropwise to the cells with gentle rocking to ensure homogeneous distribution.

After 6–8 h, the transfection medium was replaced with fresh complete growth medium to minimize cytotoxicity. Transfection efficiency was evaluated 24–48 hours later by flow cytometry or by quantitative PCR/western blotting.

2.22 Nucleofection

Cells were nucleofected using the 4D-Nucleofector System (Lonza) according to manufacturer's specifications. Briefly, cells were harvested during log-phase growth, counted, and resuspended at 2×10^6 cells per reaction in 20 µL of P3 Primary Cell 4D-Nucleofector Solution (Lonza). For CRISPR-Cas9 ribonucleoprotein (RNP) delivery, Cas9 protein (IDT) was complexed with synthetic guide RNAs at a 1:2 molar ratio in nuclease-free water for 15 minutes at room temperature to form RNPs. Each nucleofection reaction contained 3 µg of Cas9-RNP complex. Cell-RNP mixtures were transferred to 16-well Nucleocuvette Strips and nucleofected using program CM-130 for primary cells or DN-100 for cell lines. Immediately following nucleofection, cells were rescued with 80 µL of pre-warmed culture medium without antibiotics and incubated at 37°C for 10 minutes before transfer to culture vessels. Antibiotic selection or FACS-assisted clone generations was initiated 24-36 hours post-nucleofection when applicable.

2.23 Lentiviral transduction

Lentiviral particles were produced using a third-generation packaging system in HEK293T cells. Transfer plasmids containing genes of interest under control of constitutive (EF1α, CMV) or inducible (TetOn, doxycycline-responsive) promoters were co-transfected with packaging plasmids psPAX2 (gag-pol) and pMD2.G (VSV-G envelope) at a 4:3:1 molar ratio using polyethylenimine (PEI, 1 mg/mL) in serum-free DMEM. Medium was replaced 6 hours post-transfection with DMEM containing 10% FBS. Viral supernatants were harvested at 48 and 72 hours, filtered through 0.45 µm PVDF membranes, and concentrated using Lenti-X Concentrator (Takara) according to manufacturer's instructions. Viral

titers were determined by transduction of HEK293T cells with serial dilutions followed by flow cytometric analysis of fluorescent reporter expression or qPCR-based assessment using the Lenti-X qRT-PCR Titration Kit (Takara).

Target cells were transduced at multiplicity of infection (MOI) ranging from 0.1-10 in the presence of 8 μg/mL polybrene (Sigma-Aldrich) to enhance viral uptake. Transduction medium was replaced after 24 hours with fresh growth medium. For stable cell line generation, selection was initiated 48-72 hours post-transduction using appropriate antibiotics (puromycin 2-10 μg/mL, blasticidin 2-15 μg/mL, or hygromycin 50-400 μg/mL) with selection concentrations determined by kill curve analysis. Transduction efficiency was assessed by flow cytometry for fluorescent markers or by antibiotic resistance for selection markers.

2.24 RNA-seq analysis

Reads were processed using Trimmomatic (v0.38) and aligned to mm10 using STAR (v2.7.8a). Lowly expressed genes were removed and normalized count matrices were generated using the median of ratios method. Differentially expressed genes (DEGs) were then obtained from DESeq2 (v2.11.40.7). gProfiler was used for Gene set enrichment analyses (GSEA). Volcano plots were either generated using Tableau (v.2022.1) or Phantasus (v1.17.4).

2.25 Protein Structure Visualization

Three-dimensional protein structures were predicted using AlphaFold (version 3) via the AlphaFold database (https://alphafold.ebi.ac.uk), with data downloaded as a compressed archive containing mmCIF model files and confidence metrics in JSON format. The highest-ranked model was selected for visualization.

Structures were visualized using PyMOL (version 2.5.0, Schrödinger, LLC). The .cif file was loaded via the graphical interface. To isolate a single subunit from multimeric predictions, chain information was accessed using `cmd.get_chains()` in the command line (e.g., `print cmd.get_chains('model_name')`), and specific chains were displayed (`show cartoon, model_name and chain X`) while others were hidden (`hide cartoon, model_name and chain Y`). The structure was colored uniformly (`color green, model_name and chain X`) and centered (`zoom model_name and chain X`) using cartoon mode to highlight secondary structure elements.

2.26 Statistical analysis

Statistical analysis was performed using GraphPad Prism (version 9.5.1) and R (version 4.3.0). Data are presented as mean ± standard error of the mean (SEM) unless otherwise indicated. When resources were sufficient, sample sizes were determined using power analysis to detect effect sizes of 0.8 with 80% power at $\alpha = 0.05$. Normality of data distribution was assessed using the Shapiro-Wilk test and visual inspection of Q-Q plots. Equality of variances was evaluated using Levene's test.

For comparisons between two groups, unpaired two-tailed Student's t-tests were used for normally distributed data, or Mann-Whitney U tests for non-normally distributed data. For multiple group comparisons, one-way ANOVA followed by Tukey's post-hoc test was used for normally distributed data, or Kruskal-Wallis test followed by Dunn's post-hoc test for non-normally distributed data. For repeated measures or paired data, paired t-tests or Wilcoxon signed-rank tests were applied as appropriate. Two-way ANOVA was used to analyze data with two independent variables, followed by Šídák's multiple comparisons

test.

For time-course experiments, two-way repeated measures ANOVA was employed. Correlation analyses were performed using Pearson's correlation coefficient for normally distributed data or Spearman's rank correlation for non-parametric data. Survival analysis was performed using the log-rank (Mantel-Cox) test with Kaplan-Meier survival curves.

All statistical tests were two-tailed with $\alpha = 0.05$. Multiple comparisons were corrected using the false discovery rate (FDR) method when appropriate. Statistical significance is indicated as follows: * $P<0.05$; ** $P<0.01$; *** $P<0.001$; **** $P<0.0001$. The specific statistical test used and exact P values are provided in figure legends. All experiments were performed with a minimum of three biological replicates unless otherwise stated. No statistical methods were used to predetermine sample sizes, but sample sizes were chosen based on previous experience and published studies using similar methodologies.

Chapter 3

IL-17 cytokines influence metabolic physiology in a diet- and sex-dependent manner

Proinflammatory cytokines shape metabolic physiology and tissue integrity (Meizlish et al., 2021). Among them, members of the IL-17 family offer compelling examples of immunometabolic crosstalk (Douglas et al., 2023; Bechara et al., 2021). Under homeostatic conditions, or at the early hours of infection, tissue-resident lymphocytes such as γδ T cells and ILC3s produce the vast majority of IL-17A and IL-17F (Fan & Rudensky, 2016; Omenetti et al., 2019; Zúñiga et al., 2010). These newly released cytokines in turn engage dimeric and multimeric receptor complexes on non-hematopoietic cells, allowing IL-17A/F to act directly on adipose, liver, and muscle parenchyma (Meng et al. 2012; Lemmers et al., 2009; Majumder et al., 2019; Hu et al., 2020). As a consequence, IL-17A/F are now appreciated to influence energy utilization, fat accumulation, and glucose regulation (Kohlgruber et al., 2018; Zúñiga et al., 2010; Subudhi et al., 2024; Peng et al., 2024; Greenhill et al., 2021).

These effects are particularly evident in adipose tissue, where IL-17A/F orchestrate complex interactions between immune, neuronal, and metabolic com-

partments (Chehimi et al., 2017; Li et al., 2023; Teijeiro et al., 2021). Through direct signaling on adipocytes and stromal cells, as well as indirect effects mediated by tissue-resident immune cells, IL-17A/F alter adipose tissue function and systemic energy balance (Ahmed & Gaffen, 2010; Qu et al., 2016). This dual mechanism of action positions IL-17 cytokines as key modulators of adipose tissue homeostasis. Importantly, emerging evidence suggests that homeostatic levels of IL-17A/F promote metabolically favorable phenotypes in adipose depots, with particularly striking effects in brown adipose tissue (Hu et al., 2020). In contrast, unrestrained production of IL-17A/F is associated with metabolic disease and tissue damage (Chehimi et al., 2017; Riedel et al., 2020; Giles et al., 2016). As detailed in Chapter 1, this interplay deepens in thermogenic fat depots, where IL-17A and IL-17F act in a complementary fashion to stimulate *Ucp1* expression while maintaining sympathetic nerve connections (Kohlgruber et al., 2018; Hu et al., 2020).

Despite these established effects on thermogenesis, adipogenesis, and innervation, the molecular mechanisms linking IL-17 signaling to specific metabolic pathways remain largely undefined. Moreover, how IL-17 signaling shapes nutrient utilization and metabolic flux remains almost entirely unknown. The present chapter aims to address this gap by investigating where, and under what conditions, IL-17A and IL-17F exert direct control over lipid and carbohydrate metabolism, and how this control translates into whole-body fuel selection and temperature homeostasis.

Two key observations motivated this investigation. First, our preliminary work on*Il17a/f*$^{-/-}$ mice revealed altered whole-body substrate utilization, with evidence of disrupted carbohydrate or lipid metabolism that pointed toward potential defects in biosynthetic pathways. Second, the metabolic demands of ther-

mogenic adipose tissue create an ideal context for investigating IL-17's biosynthetic functions, as brown adipocytes create a steady supply of specialized lipid membranes and engage in rapid mobilization of lipid substrates that maintain thermogenic capacity (Ying et al., 2023). Given that IL-17RC is expressed at high levels on adipocytes, brown fat emerged as a logical target tissue for mechanistic investigation (Hu et al., 2020; Sinton et al., 2023).

To address these observations and open questions, we relied on genetic models, recombinant cytokine treatments, dietary interventions, and heavy water tracing to directly assess metabolic regulation and flux. Our experimental approach proceeded from organism to pathway to mechanism, beginning with whole-animal energetics and mapping these phenotypes onto tissue-specific programs in adipose tissue and liver. Ultimately, these experiments highlighted IL-17A/F's versatility as direct regulators of lipogenic programs in adipose tissue, with effects coupling to whole-body fuel selection and thermal stability in a sex-dependent manner.

3.1 Results

3.1.1 IL-17A/F deficiency is associated with altered thermoregulation and substrate utilization

While the interplay between cytokine signaling and systemic metabolism is beginning to gain the attention in the literature, many mechanistic details remain obscure. Both metabolic and immune processes are dynamic and subject to regulation by a variety of intrinsic factors, such as biological sex, circadian rhythm, and hormonal status, that can influence the outcome of inflammatory signaling. Despite this, an unwarranted majority of research in the field of immunometabolism relies on male subjects and does not account for temporal fluctuation in physio-

logical processes. To develop a more comprehensive picture of how IL-17 signaling participates in systemic metabolic control, we measured metabolic parameters in male and female mice at hourly intervals, which enabled us to examine how IL-17-mediated effects are modulated by sex and circadian rhythm. We reasoned that this strategy would allow for a more physiologically intact context for assessing IL-17's contribution to metabolic homeostasis.

Prior work by the Lynch Lab and others has established that the cytokines IL-17A and IL-17F modulate metabolic processes in male mice; however, their contributions to whole-body metabolism in females remain unresolved (Kohlgruber et al., 2018; Hu et al., 2020). To address this knowledge gap and to interrogate the potential functional redundancy between these closely related cytokines, we used a genetic model in which both*Il17a* and *Il17f* were concomitantly ablated (these animals are referred to as$Il17a/f^{-/-}$ mice for remainder of this thesis).

To obtain an unbiased assessment of the contribution of IL-17A and IL-17F to systemic energy homeostasis, we employed indirect calorimetry using the Comprehensive Lab Animal Monitoring System (CLAMS). This methodology enabled simultaneous measurements of core body temperature, respiratory gas exchange, energy expenditure, and locomotor activity. To minimize confounding effects arising from adaptive thermogenesis and thereby isolate intrinsic metabolic regulation, age-matched wildtype and $Il17a/f^{-/-}$ mice were maintained at their thermoneutrality zone (30°C). After a 48-hour acclimation period, metabolic parameters were recorded continuously over 72 hours to ensure reliable capture across multiple circadian cycles. In line with earlier research in single-knockout models, male $Il17a/f^{-/-}$ mice showed a marked thermoregulatory impairment, as evidenced by consistently lower core body temperatures than WT controls (Figure 3.1A). Core temperatures were reduced by an average of 0.8°C (36.0 $\pm$ 0.2°C

vs. 36.8 ± 0.1°C at ZT18) during the dark phase, when mice are most likely to be awake, feeding, and metabolically active. These findings pointed towards thermogenic dysfunction, compromised metabolic activation, or dysregulation of both processes. Nutrient utilization was severely disrupted alongside this thermoregulatory failure. Particularly during the dark cycle, male *Il17a/f*$^{-/-}$ mice had a significantly lower respiratory exchange ratio (RER), a real-time indicator of substrate preference, suggesting a shift away from carbohydrate oxidation and, among other possibilities, towards a compensatory reliance on lipids for fuel (Figure 3.1B). This altered substrate preference occurred despite normal food intake patterns and locomotor activity, suggesting a primary defect in metabolic fuel selection.

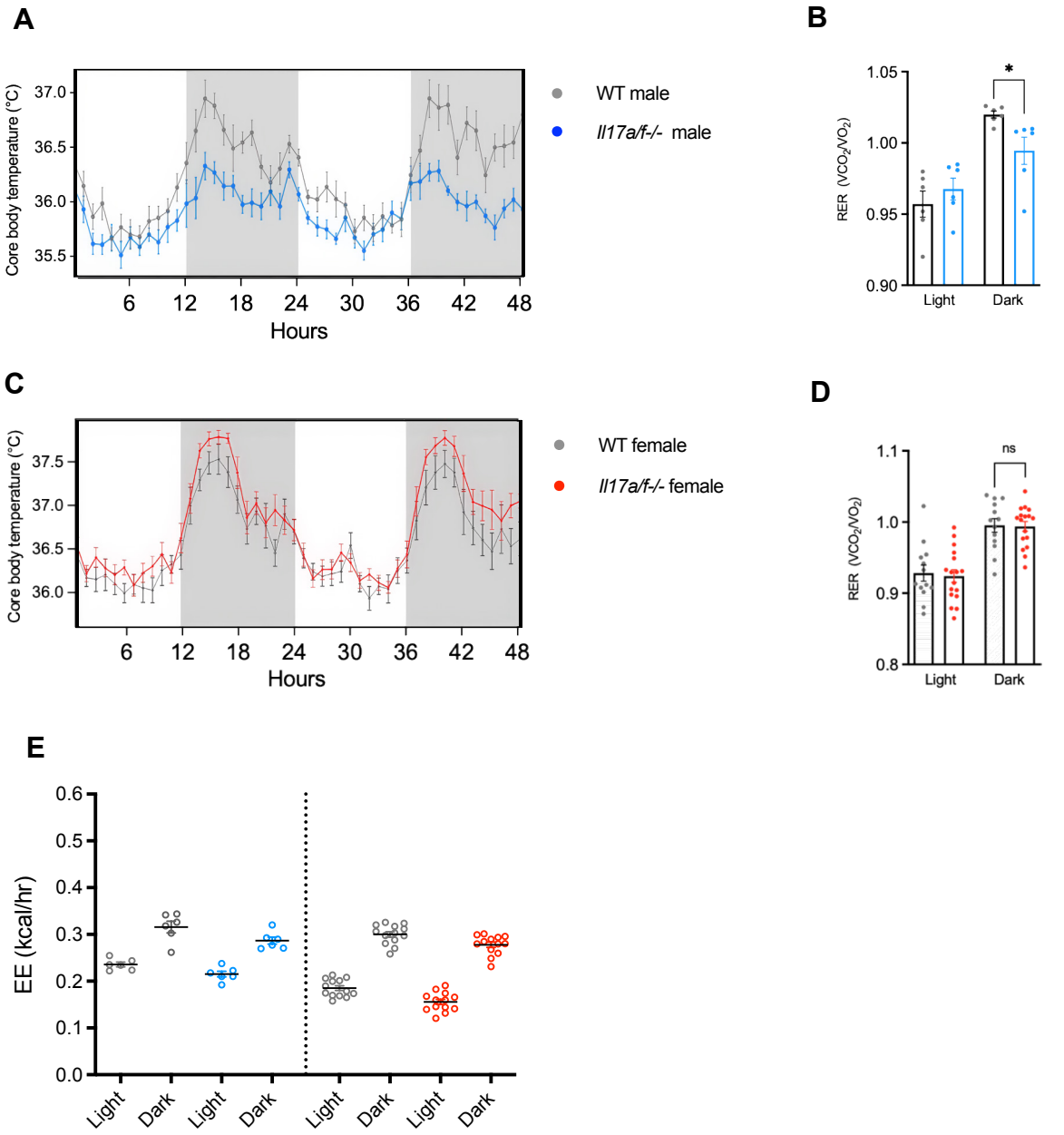


Figure 3.1 IL-17A/F deficiency alters thermoregulation and substrate utilization in a sex-dependent manner.

(A) Core body temperature of age-matched WT and *Il17a/f* -/- male mice housed at 30°C (n = 6 per group).(B) Respiratory exchange ratios (RER) of male mice from (A). (C) Core body temperature of age-matched C57BL/6J and *Il17a/f* -/- female mice housed at 30°C (n = 11-12 per group). (D) Analysis of female core body temperature averaged over light and dark cycles. (E) Energy expendature for age-mached WT and *Il17a/f* -/- male (n=6) and female (n=11-12) mice

To our surprise, however, female *Il17a/f*$^{-/-}$ mice showed an entirely different phenotype. Female knockouts had considerably higher core body temperatures than their WT counterparts, particularly during the active dark phase (37.5 ± 0.2°C vs. 36.9 ± 0.1°C at ZT18) (Figure 3.1C–D). This change in thermoregulation appeared to be independent of whole-body substrate metabolism, as the RER of female knockouts remained largely indistinguishable from that of WT controls throughout the circadian cycle. The appearance of these profound and opposing sex-specific metabolic signatures prompted us to further investigate the underlying molecular pathways regulated by IL-17 signaling in critical tissues.

3.2 Transcriptional Profiling Identifies De Novo Lipogenesis as a Primary Target

3.2.1 RNA-Seq Analysis of Brown Adipose Tissue

Brown adipose tissue (BAT) plays an important role in the control of energy balance through thermogenesis, fatty acid mobilization, and glucose uptake, processes that are central to overall metabolic health (Stanford et al., 2013; Chondronikola et al., 2014). In the last few years, multiple pro- and anti-inflammatory cytokines have emerged as important regulators of adipose tissue biology, influencing both adipocyte maturation and the inflammatory milieu of the tissue itself (Hu et al., 2020; Kohlgruber et al., 2018; Teijeiro et al., 2021). As detailed above, IL-17A in particular has also been shown to promote thermogenic pathways in adipocytes in response to cold and metabolic stress, at least in males, suggesting a broad influence over BAT activity (Hu et al., 2020; Douglas et al., 2024).

Given the significant thermoregulatory abnormalities found in our*Il17a/f*$^{-/-}$ mice, we reasoned that the lack of IL-17A and IL-17F could induce sex-dependent

transcriptional changes in BAT. To investigate this, we conducted unbiased RNA sequencing on interscapular BAT of WT and double KO mice of both sexes. Tissues were taken at Zeitgeber Time 8 (ZT8) to obtain baseline transcriptional states. Differential expression analysis revealed a prominent, male-specific disruption of metabolic gene programs. Pathway enrichment in *Il17a/f*$^{-/-}$ males showed that central processes implicated in carbohydrate metabolism were most strongly repressed (Figure 3.1C,E). Closer inspection revealed coordinated suppression of the transcriptional machinery controlling de novo lipogenesis (DNL), the transcriptionally controlled anabolic pathway that converts carbohydrate precursors into fatty acids. Most notably, the master transcriptional regulator Mlxipl (encoding ChREBP) of carbohydrate-induced fatty acid synthesis was significantly downregulated in the BAT of male double KOs. ChREBP and its transcriptional targets are implicated to be essential for lipid synthesis and energy storage in BAT, and their repression has been linked with profound effects on metabolic health and reductions in thermogenic flexibility (Sánchez-Gurmaches et al., 2018; Schlein et al. 2021).

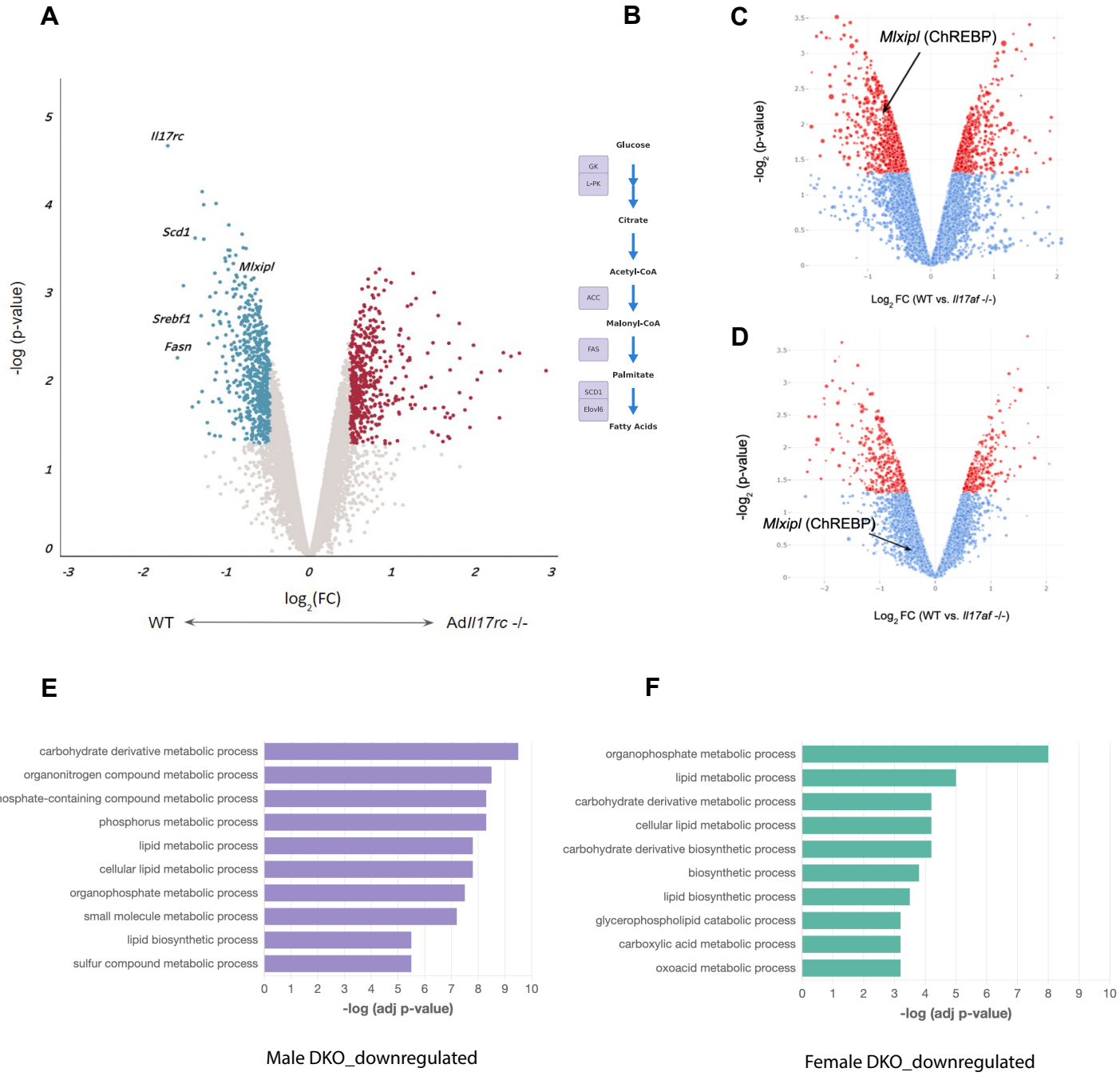


Figure 3.2 Transcripts controlling lipid synthesis are significantly dysregulated in brown adipose tissue from *Il17a/f* and adipocyte-specific *Il17rc* (AdIl17rc) KO male mice

(A)Volcano plot showing differential gene expression in BAT) from male mice with an adipocyte-specific deletion of Il17rc (AdIl17rc KO) compared to wild-type (WT) controls. Key downregulated genes in the *de novo* lipogenesis pathway are indicated. Data were reanalyzed from public dataset GSE144255 (n = 3 per group). (B) Simplified schematic of the DNL pathway. (C, D) Volcano plots comparing differential gene expression in BAT from male (C) and female (D) Il17a/f -/- mice versus WT controls. Tissues were collected at a baseline state, Zeitgeber Time 8 (ZT8). The master DNL regulator Mlxipl (encoding ChREBP) is highlighted. (E, F) Gene Ontology pathway enrichment analysis of metabolic genes significantly downregulated in BAT from male (E) and female (F) Il17a/f -/- mice.

To validate that this was an adipocyte-autonomous effect of altered IL-17 signaling, we reanalyzed a publicly available RNA-seq dataset from male mice harboring an adipocyte-specific deletion of Il17rc (AdIl17rc). This orthogonal analysis highlighted an even greater level of transcriptional dysregulation, as Mlxipl and its major targets, including Scd1 and Fasn, were among the top downregulated mRNA species (Figure 3.2A). In our view, the fidelity of these distinct datasets provided strong evidence that IL-17A/F (or at the very least, IL-17A *or* IL-17F) act directly on adipocytes to sustain the DNL program. In sharp contrast, female *Il17a/f*$^{-/-}$ mice were transcriptionally insensitive to IL-17A/F deletion in this context, as major DNL transcript levels (e.g., Mlxipl) were not significantly affected (Figure 3.2D,F). This dramatic transcriptional divergence provided the first molecular evidence that IL-17A/F signaling is a critical, male-specific regulator of the lipogenic program of brown adipose tissue.

3.2.2 Temporal Dynamics of DNL Disruption

Recent data by the Lynch Lab showed that in murine adipose, IL-17A and IL-17F levels rise precipitously during the dark phase. This circadian pattern dovetails with the known circadian regulation of DNL, which reaches its highest peak in rodents at night. We therefore sought to determine whether the circadian induction of DNL genes was specifically defective in*Il17a/f*$^{-/-}$ male mice. Quantitative RT-PCR was performed in BAT isolated at two different time points: ZT6 (midday, resting phase) and ZT18 (midnight, active phase). At ZT6, during periods of low anabolic activity in mice, we saw no statistically significant differences in DNL gene expression levels between knockout and WT males (Figure 3.3A). However, by ZT18, during peak feeding hours and increasing IL-17 production, we observed an acute failure of the lipogenic transcriptional program in*Il17a/f*$^{-/-}$ male mice:

Acly, Fasn, Acaca, and Scd1 were significantly reduced in the BAT of knockout males compared to WT controls (Figure 3.3B). In contrast, critical transcripts that are engaged in thermogenesis and lipolysis, such as Ucp1 and Ppargc1a, were decreased in knockout males at both points, consistent with their hypothermic state and not indicative of disrupted circadian rhythm (Figure 3.3C–D). This selective failure to upregulate the DNL pathway upon feeding further strengthened our hypothesis that IL-17A/F signaling is critical for proper diurnal regulation of lipogenesis in male BAT.

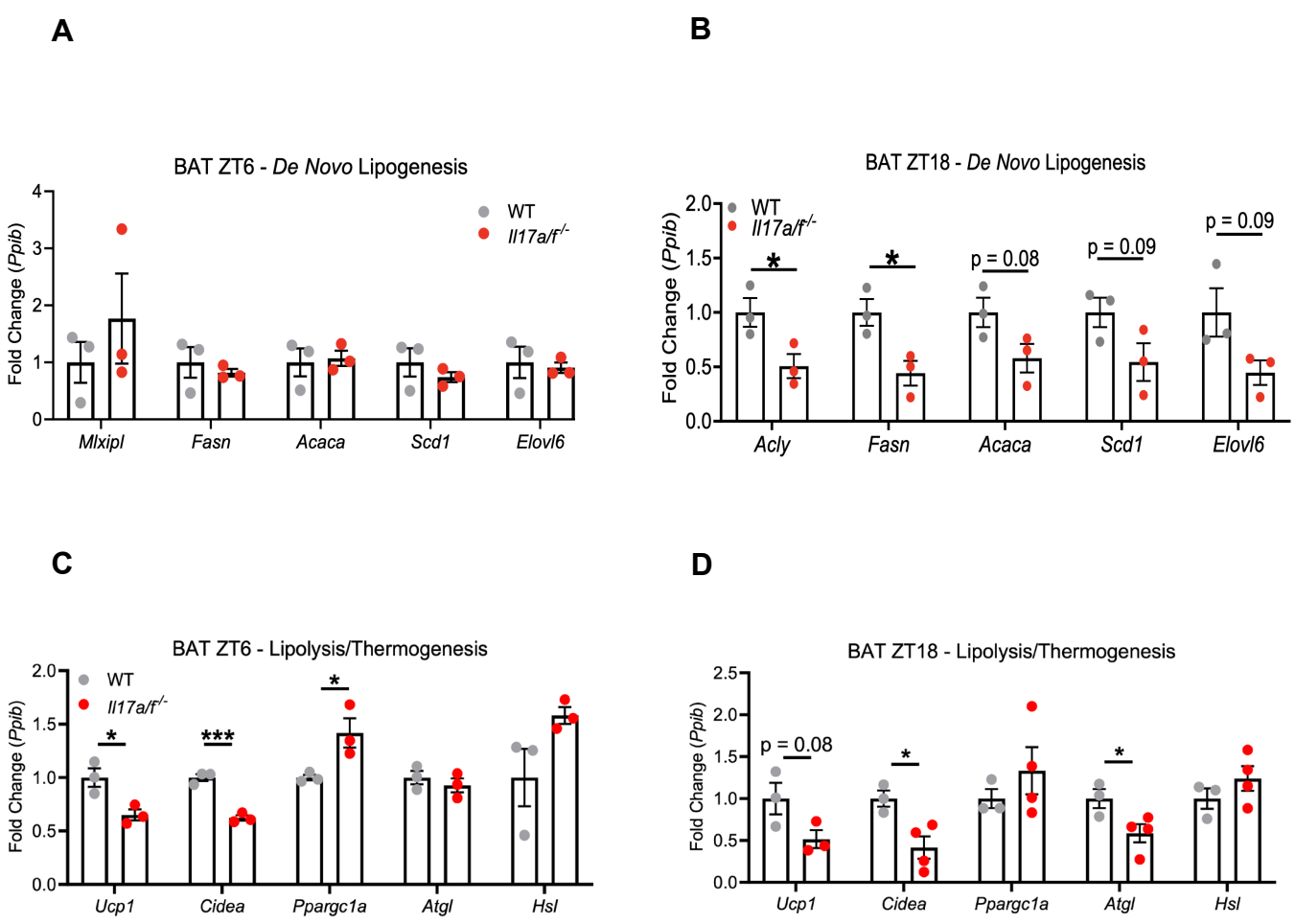


Figure 3.3 Lipogenic transcripts are downregulated in *Il17a/f -/-* male mice specifically during the dark cycle.

(A) RT-PCR analysis of DNL-related transcripts in BAT from age-matched WT and *Il17a/f-/-* male mice sacrificed at ZT6. (B) RT-PCR analysis of DNL-related transcripts in male mice sacrificed at ZT18.(C) RT-PCR analysis of genes related to thermogenesis and lipid catabolism in male mice sacrificed at ZT6. (D) RT-PCR analysis of transcripts related to thermogenesis and lipid catabolism in male mice sacrificed at ZT18. Data are represented as mean ± SEM, n = 3–4 mice per group. Statistical significance was calculated using the two-tailed unpaired Student's t-test. * $P < 0.05$, *** $P < 0.001$. Experiments performed in collaboration with Aaron Douglas

3.3 IL-17A regulates adipose lipogenesis in a sex-dependent manner

Building upon our initial findings linking IL-17 signaling and lipid metabolism, we proceeded to investigate the impact of IL-17A and IL-17F on key transcriptional regulators within three interconnected metabolic pathways: de novo lipogenesis, lipolysis, and oxidative phosphorylation. To this end, wild-type mice were administered recombinant IL-17A or IL-17F intraperitoneally, and transcriptional responses in brown adipose tissue were then quantified via RT-PCR (Figure 3.4A).

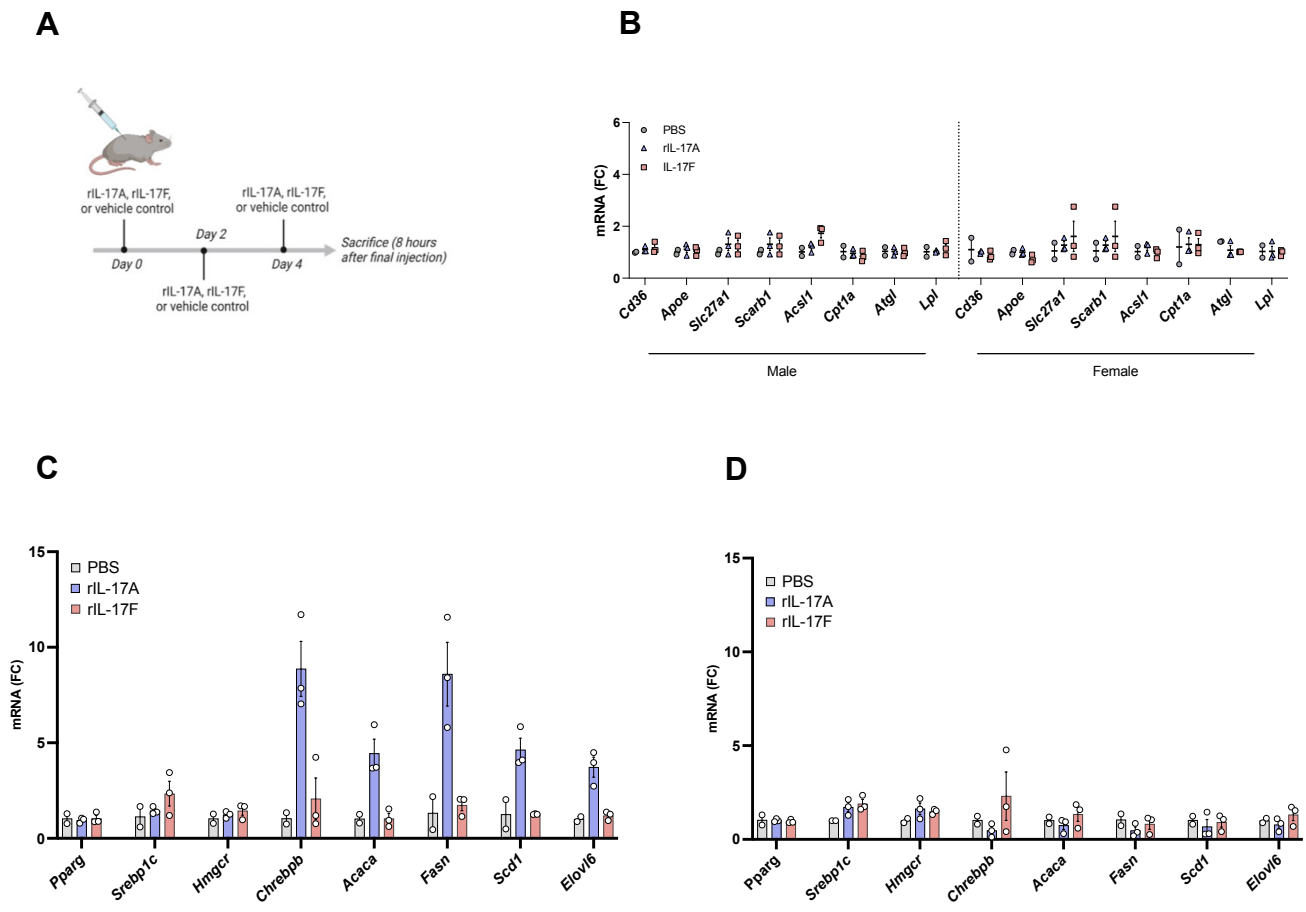


Figure 3.4 Administration of IL-17A, but not IL-17F, induces robust expression of genes related to *de novo* lipogenesis in male mice

(A) Experimental schematic for administration of PBS, recombinant IL-17A (1 μg/animal), or IL-17F (1 μg/animal) via intraperitoneal injection over the course of five days. (B) Relative expression levels of genes related to lipid catabolism and uptake in BAT, analyzed via RT-PCR (n = 2-3 per group). (C) Relative expression levels of transcriptional regulators of lipid synthesis in male BAT, analyzed via RT-PCR (n = 2-3 per group). (D) Relative expression levels of transcriptional regulators of lipid synthesis in female BAT, analyzed via RT-PCR (n = 2-3 per group) Data are represented as mean ± SEM.

The administration of recombinant IL-17A (rIL-17A) was sufficient to produce a strong and specific lipogenic response in the BAT of male mice. Key DNL-associated genes such as Chrebp-β, Fasn, and Scd1 were significantly upregulated compared to PBS-treated controls (Figure 3.4C). In contrast, rIL-17F produced only marginal lipogenic responses at the transcriptional level. Notably, the expression levels of genes implicated in lipid uptake or catabolism (e.g., *Cd36, Scarb1, Lpl, Atgl*) were unaltered after treatment with either cytokine, even after multiple treatments, suggesting that IL-17A has a selective effect on lipogenic pathways in male BAT (Figure 3.4B). In agreement with our findings using the knockout models, female mice were resistant to the lipogenic effects of IL-17A. Female BAT did not show detectable induction of DNL genes under the identical treatment regimen (Figure 3.4D). This failure to respond was not due to differences in receptor expression, at least at the mRNA level, as*Il17ra* and *Il17rc* enrichment were comparable in both sexes. This suggests that the sexual dimorphism in IL-17 responsiveness is downstream of the receptor, possibly involving crosstalk with sex hormone signaling pathways (an angle which our lab is now actively pursuing).

3.4 Functional Assessment of De Novo Lipogenesis

3.4.1 In Vivo Flux Measurements

To test the physiological implications of our findings at the mRNA level, we evaluated the rate of DNL in vivo using heavy-labeled water (D_2O) tracing, the gold standard for metabolic flux measurements (Wallace et al., 2018). WT and *Il17a/f*$^{-/-}$ mice were given 8% D_2O in their drinking water, and the experiments

were carefully timed so as to capture lipogenic activity during the dark period. Following treatment, tissue extraction, and GC-MS analysis, we found a significant decrease in DNL flux in the BAT of male *Il17a/f*$^{-/-}$ mice, with the rate of de novo palmitate synthesis reduced by approximately 50% compared to WT controls (Figure 3.5D–E). The liver showed a comparable but more mild decline in DNL (Figure 3.5F), indicating that in the absence of IL-17A/F, BAT is a key site of impaired lipogenesis in males. Female *Il17a/f*$^{-/-}$ animals, by contrast, showed no such suppression in lipogenic flux in either the BAT or liver, consistent with their intact DNL gene expression. These functional data provided additional evidence that the IL-17–DNL axis is sensitive to biological sex and tissue-specific control.

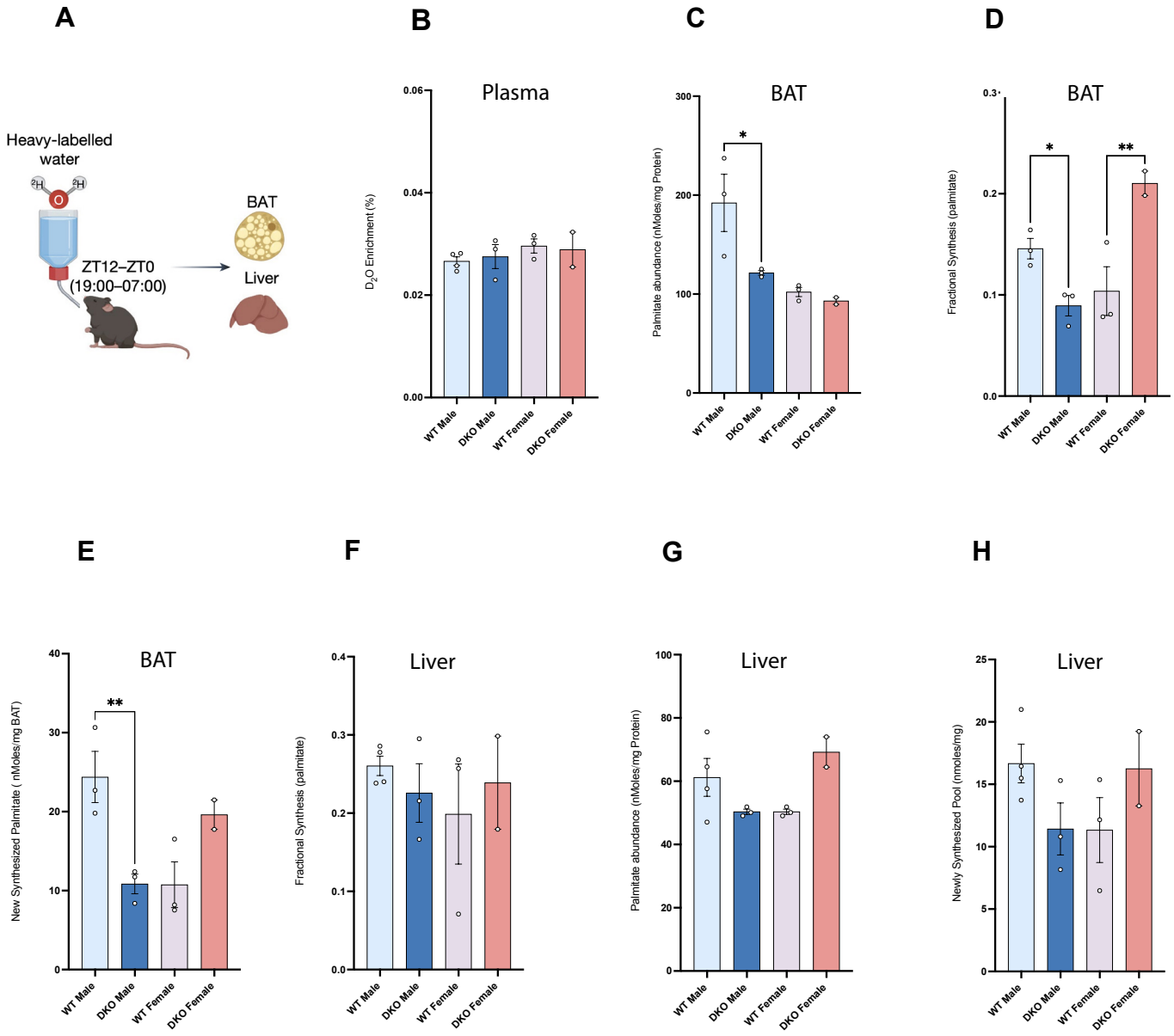


Figure 3.5 *De novo* lipogenesis is functionally impaired in the brown adipose tissue of male *Il17a/f -/-* (DKO) mice.

(A) Experimental schematic showing overnight 8% D_2O labeling protocol in mice with subsequent tissue collection. (B) Plasma ^2H_2O enrichment (%) demonstrating successful isotope incorporation across experimental groups. (C) Palmitate abundance (nmoles/mg protein) and (D) fractional synthesis of palmitate in brown adipose tissue (BAT). (E) Newly synthesized palmitate pool (nmoles/mg BAT) in BAT. (F) Fractional synthesis of palmitate and (G) palmitate abundance (nmoles/mg protein) in liver tissue. (H) Newly synthesized palmitate pool (nmoles/mg) in liver. Data from male and female wildtype (WT) and Il17af-/- DKO mice following overnight ^2H_2O labeling (n = 3-5 per group). Mass spectromitry experiments were conducted with technical assistance from Karl Wessendorf-Rodriguez.

3.5 IL-17A/F Modulate the Metabolic Adaptation to Sucrose-Enriched Diets

3.5.1 Dietary Carbohydrate Response

As our initial experiments were primarily conducted on chow-fed animals at steady state (i.e., when circulating levels of IL-17A/F are low and when lipid synthesis rates are relatively modest), we next examined *Il17a/f*$^{-/-}$ mice under conditions of elevated DNL activity. Meticulous research led by the Postic Lab and others has shown that targeted disruptions of FA synthesis (e.g., through deletion of Fasn, Chrebp-β, or Srebp-1c) are most consequential in conditions of high carbohydrate intake (Flowers & Ntambi, 2009; Matsukawa et al., 2023; Hodson & Gunn, 2019). Conversely, ChREBP-β null mice fed standard chow or high-fat diets are far more similar to their wild-type littermates (Recazens et al, 2022). It is also interesting to note that standard chow and the majority of high-fat diets formulated for rodents do not mirror the intake habits of an overwhelming majority of the inhabitants of industrialized countries, where the harmful effects of sugar-sweetened drinks are ubiquitous. With this in mind, we proceeded to determine the role of IL-17 in mice enjoying a high-carbohydrate lifestyle. Considering recent evidence showing that sweetened drinks are far more effective at stimulating fatty acid synthesis in humans and rodents alike (compared to sugar-laden solid food), we reasoned that this approach would offer more mechanistic insight (Jang et al., 2020).

To examine the relevance of the IL-17–DNL axis under more demanding circumstances, we challenged WT and *Il17a/f*$^{-/-}$ mice with a high-carbohydrate diet, providing them with a 20% sucrose solution as drinking water for three weeks.

This dietary challenge uncovered a significant functional outcome. Male double knockouts showed near-total resistance to the weight gain normally caused by high-sucrose feeding (Figure 3.6B). This resistance suggests that defects in the DNL pathway may act to curb the efficient conversion of surplus dietary carbohydrates into stored fat. In contrast, female mice deficient in IL-17A/F showed an exaggerated weight gain response to sucrose compared to WT females (Figure 3.6B, right). This result again highlights the profound sex-specific effects of IL-17 deficiency on energy balance, where the same genetic deletion that protects against diet-induced weight gain in males rendered females even more vulnerable.

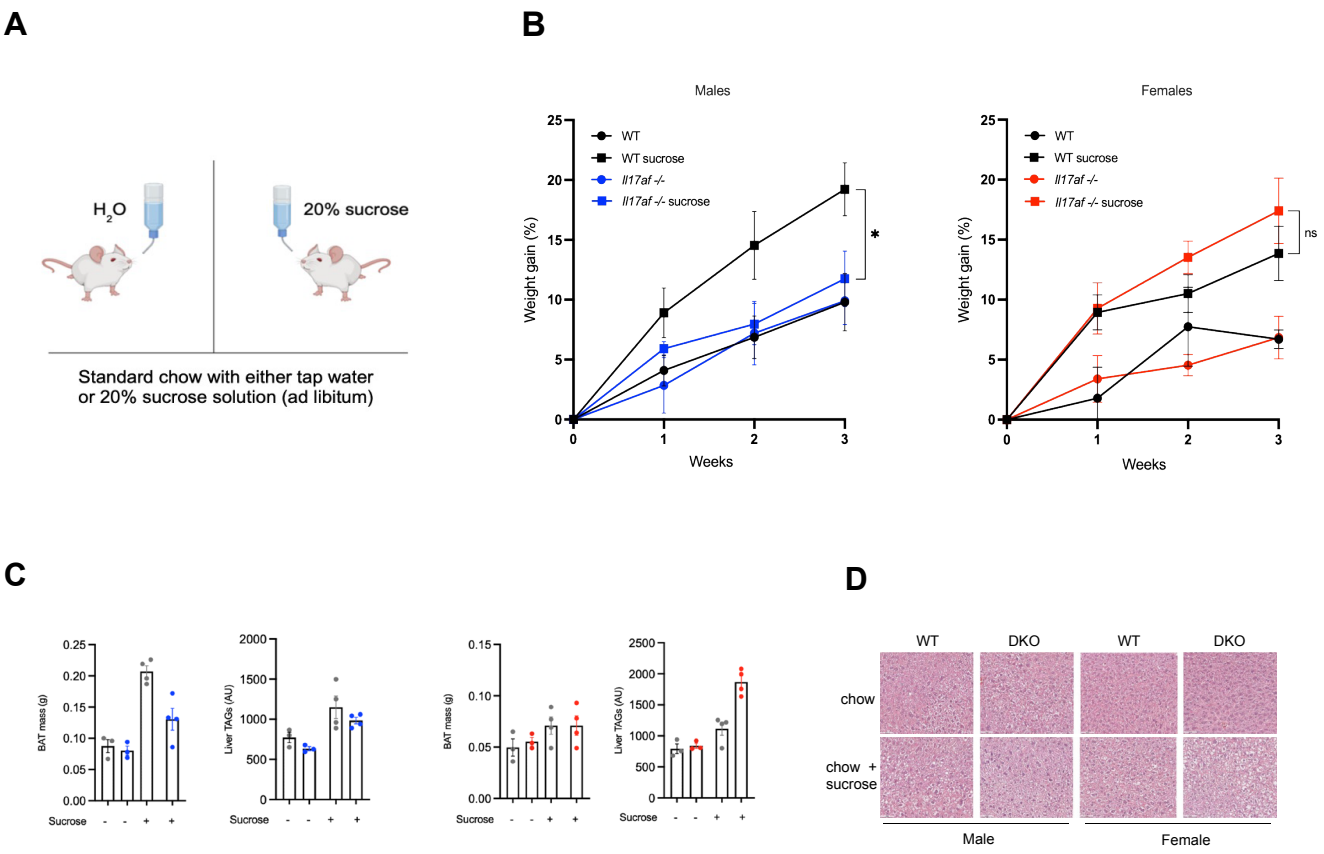


Figure 3.6 IL-17A/F deficiency elicits sexually dimorphic effects on sucrose-driven weight gain

(A) Experimental design schematic showing WT and *Il17a/f -/-* mice provided with standard chow *ad libitum* and either regular drinking water or water supplemented with 20% sucrose for three weeks. (B) Body weight gain trajectories over three weeks of treatment in male (left) and female (right) mice (n = 3–4 per group). (C) Metabolic parameters measured after three weeks of treatment, comparing sucrose versus control conditions in both genotypes. (D) Representative histological sections from male and female WT and *Il17a/f* -/- mice under control chow and chow + sucrose conditions. Data in (B) and (C) are represented as mean ± SEM. Statistical significance was calculated using one-way ANOVA. * $P < 0.05$.

3.5.2 Molecular Validation of DNL Defects

To assess how the induction of *de novo* lipogenesis is altered in knockout animals and might contribute to their resistance to weight gain, we conducted a short-term sucrose challenge in male WT,*Il17a*$^{-/-}$, and *Il17a/f*$^{-/-}$ mice. Using this model, in which we turned our attention hepatic DNL (the liver is the principle location of acute, sucrose-driven lipogenesis in the body), genetic ablation of IL-17A or IL-17A/F markedly impaired lipogenic responses at both the mRNA and protein levels. IL-17-deficient mice displayed a dampened induction of essential lipogenic genes such as Scd1, Pklr (hepatic pyruvate kinase), and Elovl6 (Figure 3.7B–C). To determine whether these transcriptional alterations were reflected at the protein level, we analyzed hepatic expression of lipogenic enzymes by Western blot. In WT mice, SCD1 protein levels exhibited robust sucrose responsiveness that was substantially blunted in*Il17a*$^{-/-}$ and *Il17a/f*$^{-/-}$ mice (Figure 3.7D). These molecular data add further context on the connection between suppressed IL-17 signaling, the impaired induction of the DNL machinery in response to a carbohydrate load, and the consequent protection from sucrose-induced weight gain in male mice.

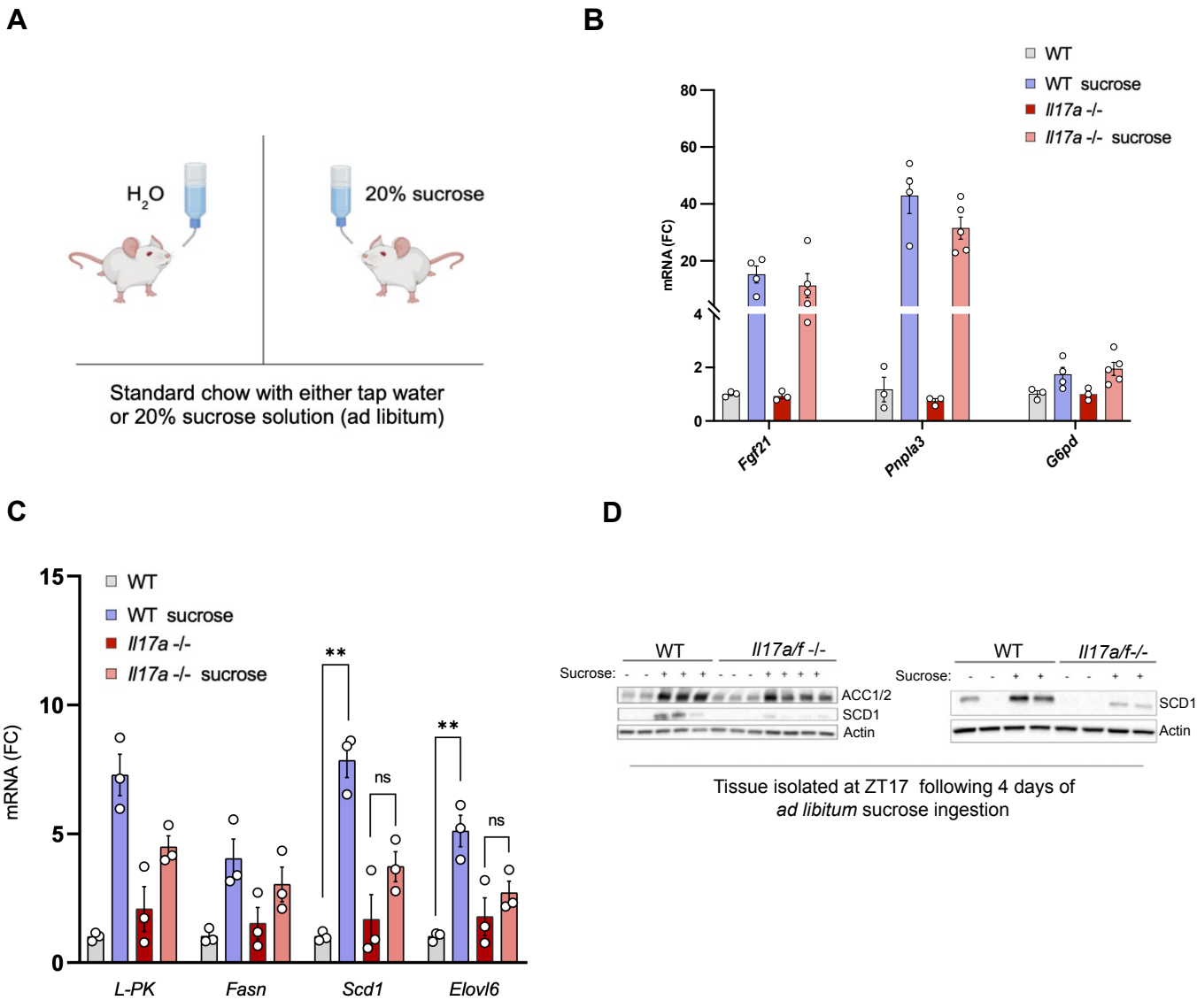


Figure 3.7 Sucrose fails to induce a full lipogenic response in male mice lacking IL-17A

(A) Experimental overview of sucrase admistration experiments.schematic showing male mice provided with standard chow ad libitum and either regular drinking water or water supplemented with 20% sucrose for four days. (B) Relative mRNA expression of sucrose-responsive genes in liver tissue from male WT and *Il17a* -/- mice after four-day treatment with regular water or 20% sucrose water (n = 3 per group). (C) Relative mRNA expression of key *de novo* lipogenesis genes in liver tissue. (D) Western blot analysis and quantification of SCD1 and ACC1/2 protein expression in liver tissue from male WT, *Il17a* -/-, and *IL17a/f* -/- mice collected after four-day treatment with regular water or 20% sucrose water. Data are represented as mean ± SEM. Statistical significance was calculated using one-way ANOVA or Cosinor analysis. * $P < 0.05$, ** $P < 0.01$.

3.6 Systemic Metabolic Integration and Clinical Relevance

3.6.1 IL-17's influence on whole-body metabolism and physiology

Our collective data define a nuanced, sexually dimorphic influence of IL-17A/F on the control of systemic energy homeostasis. In males, disruption of the IL-17–DNL pathway is associated with a unique metabolic phenotype of hypothermia, increased dependence on fat oxidation, and impaired processing of carbohydrates, culminating in a dramatic resistance to diet-induced obesity. By contrast, female mice bearing the identical genetic deletion develop a contrasting phenotype of mild hyperthermia and exquisite sensitivity to sucrose-induced weight gain, a response that is seemingly independent of significant changes in *de novo* lipogenesis.

3.6.2 Translational Relevance of the IL-17–DNL Axis in Humans

To investigate whether the IL-17–DNL axis is evident in human-derived data, we compared transcriptomics from skin biopsies of psoriasis patients before and after IL-17 pathway blockade. In a Phase 3 dataset using the IL-17 receptor antagonist brodalumab (GSE117468), blockade reduced expression of DNL-associated genes (e.g., *Scd, Acaca*) relative to placebo (Figure 3.8A). In a Phase 1 dose-escalation study with ixekizumab (anti-IL-17A; GSE31652), a broader set of DNL genes showed downregulation vs. placebo (Figure 3.8B). Although the intricate inflammatory environment of psoriasis and possible treatment-related confounders require cautious interpretation, these clinical findings are consistent with a con-

served role for IL-17 signaling in the control of lipogenic pathways across species.

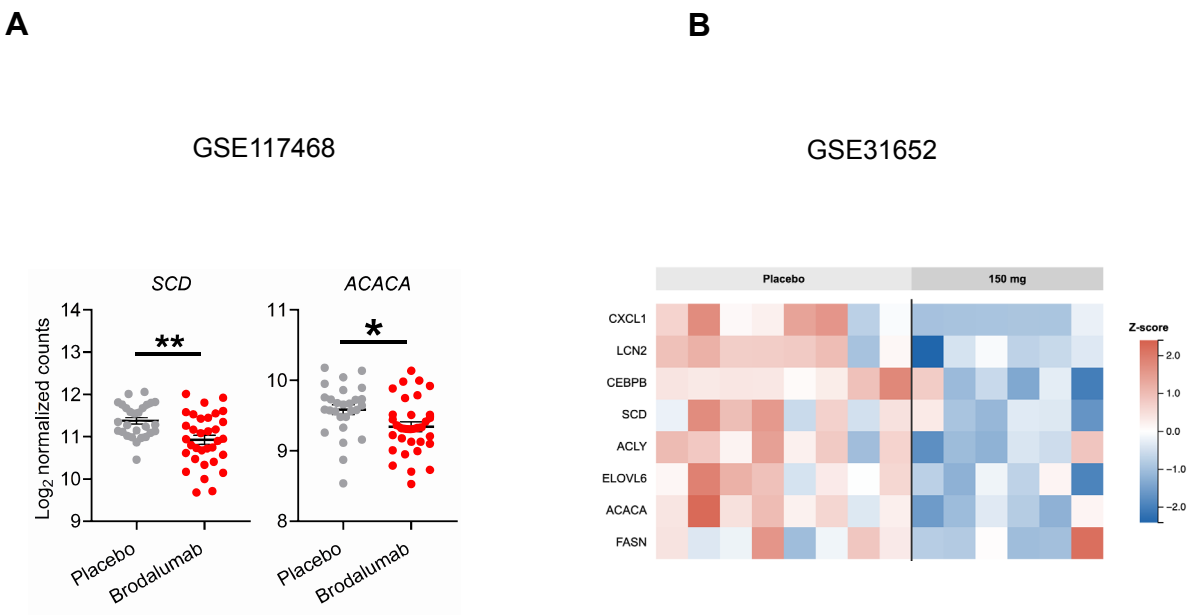


Figure 3.8 IL-17 pathway blockade reduces the expression of DNL-associated genes in human psoriasis patients.

(A) GSE117468: Expression of DNL-associated genes in skin biopsies from psoriasis patients enrolled in Phase 3 clinical trials of the IL-17A receptor antagonist brodalumab. (B) GSE31652: Heat map showing differential expression of DNL-associated genes in lesional skin biopsies from psoriasis patients treated with the anti-IL-17A monoclonal antibody ixekizumab or placebo in a Phase 1 dose-escalation trial. Expression changes are shown at 150mg dose relative to placebo at week 2 following two subcutaneous injections (weeks 0 and 2). Statistical significance indicated as *p < 0.05, **p < 0.01.

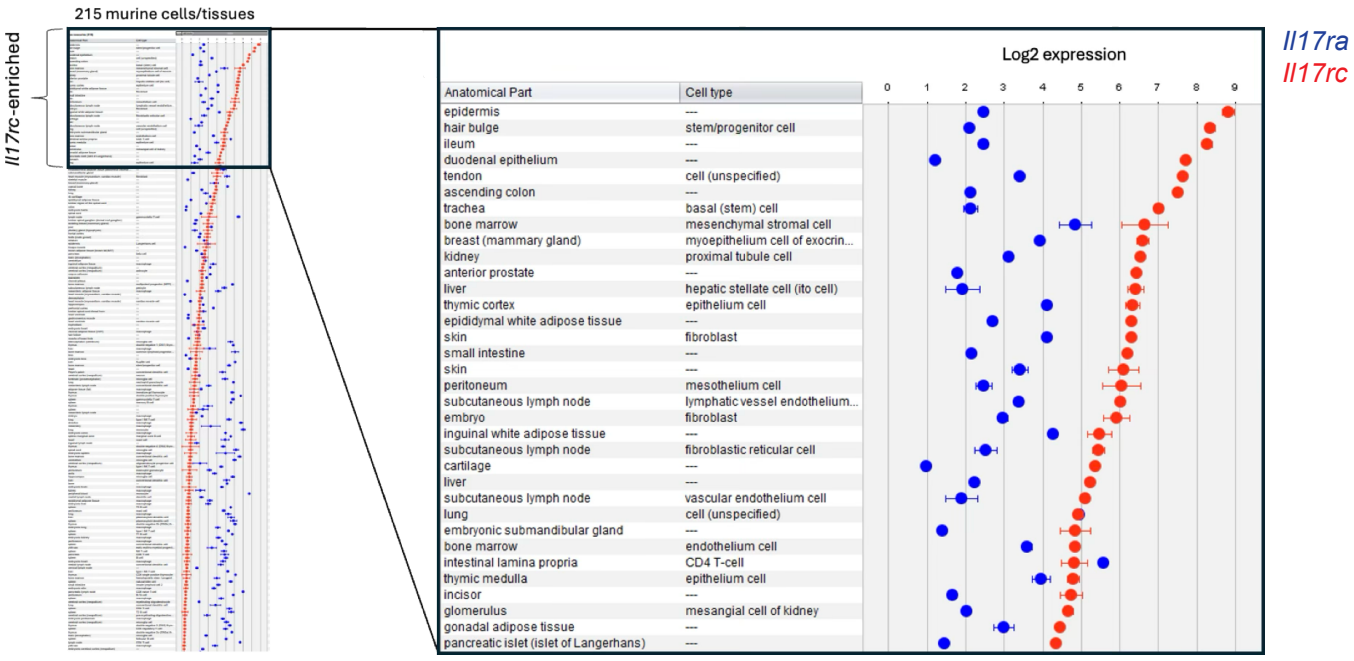
Chapter 4

The Intracellular Interactome of IL-17RC Bridges Structural Organization and Metabolic Control

4.1 Introduction

Interleukin-17 (IL-17) cytokines orchestrate tissue protective and inflammatory programs that maintain epithelial barriers and remodel damaged stroma (McGeachy et al., 2019; Wu et al., 2021; Brockmann et al., 2017). IL-17A and IL-17F signal through a heterodimeric receptor consisting of the broadly expressed IL-17RA subunit and the more selectively expressed IL-17RC subunit (Subramaniam et al., 1999; Li et al., 2019). IL-17RA is present across most somatic cells and IL-17RC expression is enriched in epithelial and mesenchymal lineages, a tissue bias that, along with IL-17RC's distinct structural characteristics, encouraged us to examine if IL-17RC serves a role beyond a simple co-receptor. Identifying the full breadth of activities and intracellular binding partners of IL-17RC is important for understanding how IL-17 signaling coordinates barrier defense, tissue remodeling, and cellular homeostasis.

A



B

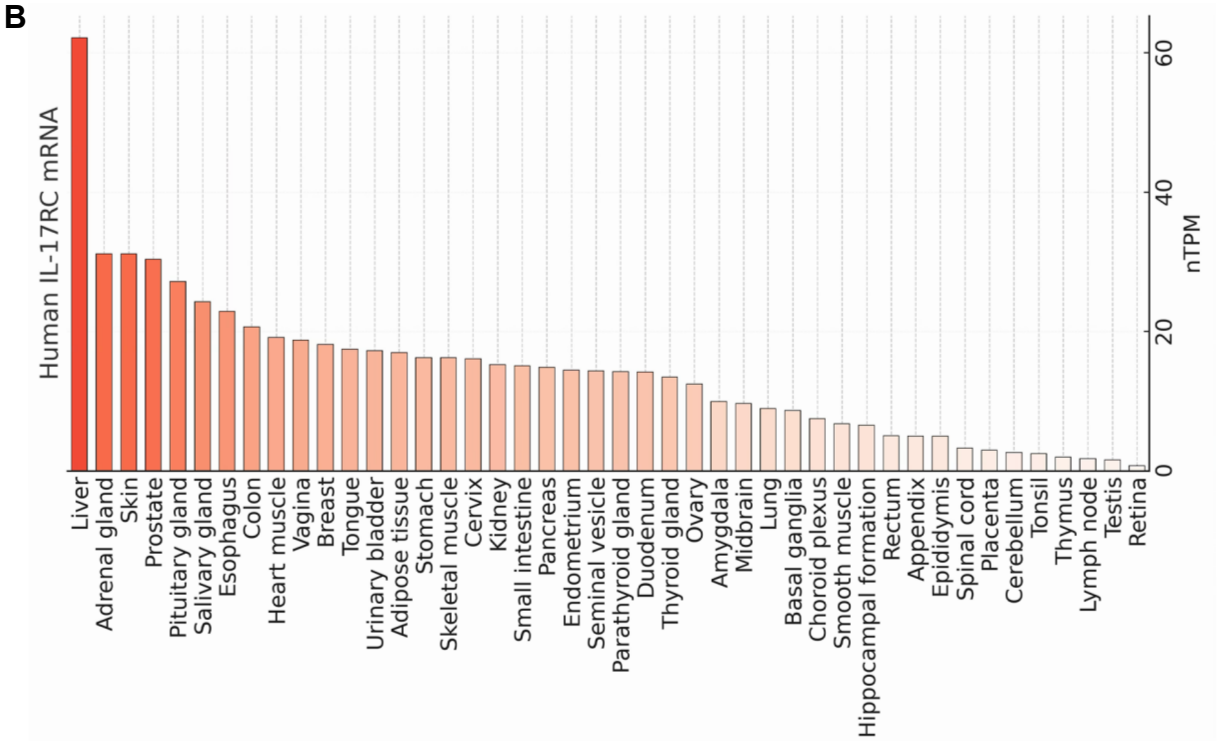


Figure 4.1 *Il17rc* is selectively enriched at barrier mucosa and stromal compartments

(A) *Il17rc* (red) and *Il17ra* (blue) transcript abundance across 215 murine tissues/cell populations, plotted on a $\log_2$ scale and ordered by *Il17rc* level; bracket marks the *Il17rc*-enriched segment. Horizontal whiskers indicate variability across samples in the source compendium (SEM). Enlarged view of the boxed region shown to aid readability of the top Il17rc-expressing entries. Entries extracted from Genevestigator (B) Human bulk--tissue RNA-seq ranking of IL17RC mRNA abundance (normalized transcripts per million, nTPM) across major organs, ordered by decreasing expression. Entries extracted from Genevestigator

IL-17RC is a type-I single-pass membrane glycoprotein that has two fibronectin-type III domains in the ectodomain that interact with complementary domains of IL-17RA in the presence of IL-17A or IL-17F. The cytoplasmic region of IL-17RC contains a SEFIR (similar expression to fibroblast growth factor and IL-17 receptors) motif that, upon ligand engagement, comes into close proximity with the SEFIR domain of IL-17RA to create a docking platform for the adaptor Act1. The recruitment of Act1 initiates assembly of TRAF E3 ligases and kinases to activate the NF-$\varkappa$B, MAP kinase and C/EBP pathways leading to transcription of chemokines, cytokines and antimicrobial peptides. In this well-established sequence of events, IL-17RC functions as the tissue-restricted element of the IL-17 receptor heterodimer, and is essential for robust IL-17A/F signaling at the plasma membrane.

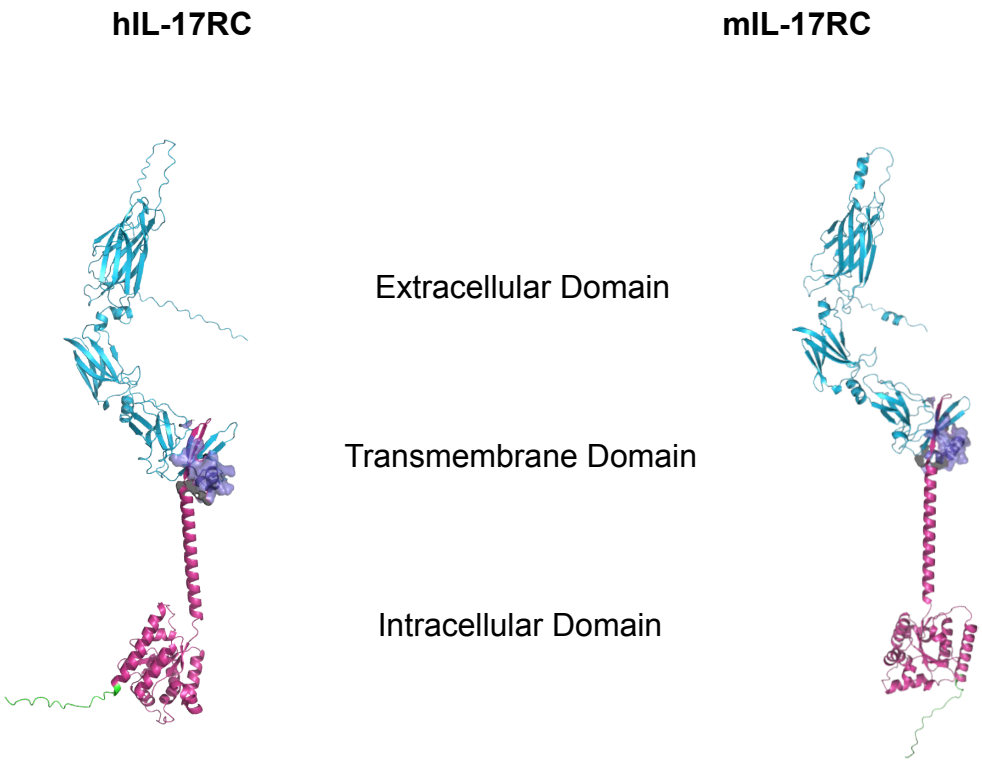


Figure 4.2 Protein architecture is largely conserved between human and murine IL-17RC
Structural comparison of IL-17RC protein between mouse and human orthologs. Three-dimensional ribbon representations showing the extracellular domain architecture of human IL-17RC (left) and mouse IL-17RC (right). Color gradient from N-terminus (blue) to C-terminus (red) indicates the polypeptide chain progression. Both structures display conserved fibronectin type III-like domains and similar overall folding patterns, suggesting functional conservation across species. Figures generated via AlphaFold 3 and PyMOL

IL17RC transcripts exhibit significant heterogeneity in both humans and rodents. For instance, alternative splicing can truncate the receptor by removing its transmembrane domain, creating soluble versions of IL-17RC which have been proposed to function as decoy receptors (Kuestner et al., 2007; Ho & Gaffen, 2010; Haudenschild et al., 2006). Other variants lack segments of IL-17RC's cytoplasmic tail, thereby compromising the extent or specificity of downstream signaling events. This isoform heterogeneity may facilitate distinct signaling outcomes, each tuned further by a cell's relative abundance of IL-17RA/IL-17RC and downstream adapter molecules.

Several receptors that were previously viewed as merely ligand-gated switches are now being reevaluated for their novel interactions in context-dependent signaling hubs. For example, the epidermal growth factor (EGF) receptor can autophosphorylate in the absence of ligand, and insulin-like growth factor receptors (IGFR) have been shown to promote survival signals in a ligand-independent manner in multiple cancer types (Cox et al., 2015; Honegger et al., 1989; Weigel & Zhang, 1998; Guo et al., 2015). There is also evidence to suggest that toll-like receptors have scaffolding, ligand-independent functions in endosomes and other densely populated regions of the cell (Hartman et al., 2010; Leibler et al., 2022; Sánchez et al., 2023). Collectively, these examples suggest that receptor conformation, post-translational modifications and subcellular localization can enable the initiation of downstream cascades even in the absence of exogenous agonists. Based on this precedent, we questioned whether IL-17RC could likewise engage intracellular partners and cellular programs in the absence of IL-17A/F.

In order to comprehensively map IL-17RC's interaction networks, we prioritized recent advances in proximity-based proteomics that surpass the intrinsic limitations of traditional pull-down and affinity purification. Although these clas-

sical approaches have greatly enhanced our knowledge of protein complexes, they are limited by several major drawbacks. First, the harsh detergent solubilization needed to isolate membrane proteins from cells often breaks weak or transient interactions that may nevertheless be vital for signaling. Second, cell lysis destroys virtually all spatial information, making it difficult to differentiate between proteins that interact in their native cellular compartments and those that only interact after lysis. Third, traditional methods often require bait proteins to be overexpressed in order to provide sufficient material for detection. This can cause stoichiometric imbalances that lead to non-physiological interactions or obscured molecular phenotypes. Additionally, the long washing steps needed to remove background noise are detrimental for low-affinity binding partners that could form biologically important regulatory interactions. These limitations led us to use proximity-based labeling methods that kept the natural protein stoichiometry, preserved spatial context throughout the workflow, and captured the full range of protein interactions that make up the dynamic protein environment in living and fixed cells, from stable complexes to short-lived encounters.

To this end, we employed microenvironment mapping (µMap), a proximity-labeling technology that covalently labels proteins that lie within mere nanometers of a target of interest in intact cells. Specifically, a validated antibody targeting the protein of interest is first linked to a photocatalyst. When the photocatalyst-labeled antibody is illuminated with visible light, the photocatalyst produces short-lived carbenes that crosslink proteins in close proximity. In turn, the reactive intermediates can only diffuse several nanometers before being quenched, allowing µMap to offer spatial precision while retaining the native location of each interaction. Critically, µMap can be performed on endogenous protein. We conducted µMap in two complementary manners: live-cell µMap

to interrogate extracellular neighbors at the plasma membrane, and µMapx in gently fixed and permeabilized cells to reveal intracellular partners. By directly comparing both datasets, we separated surface-restricted interactors from those that only emerge when IL-17RC is targeted in the cell's interior.

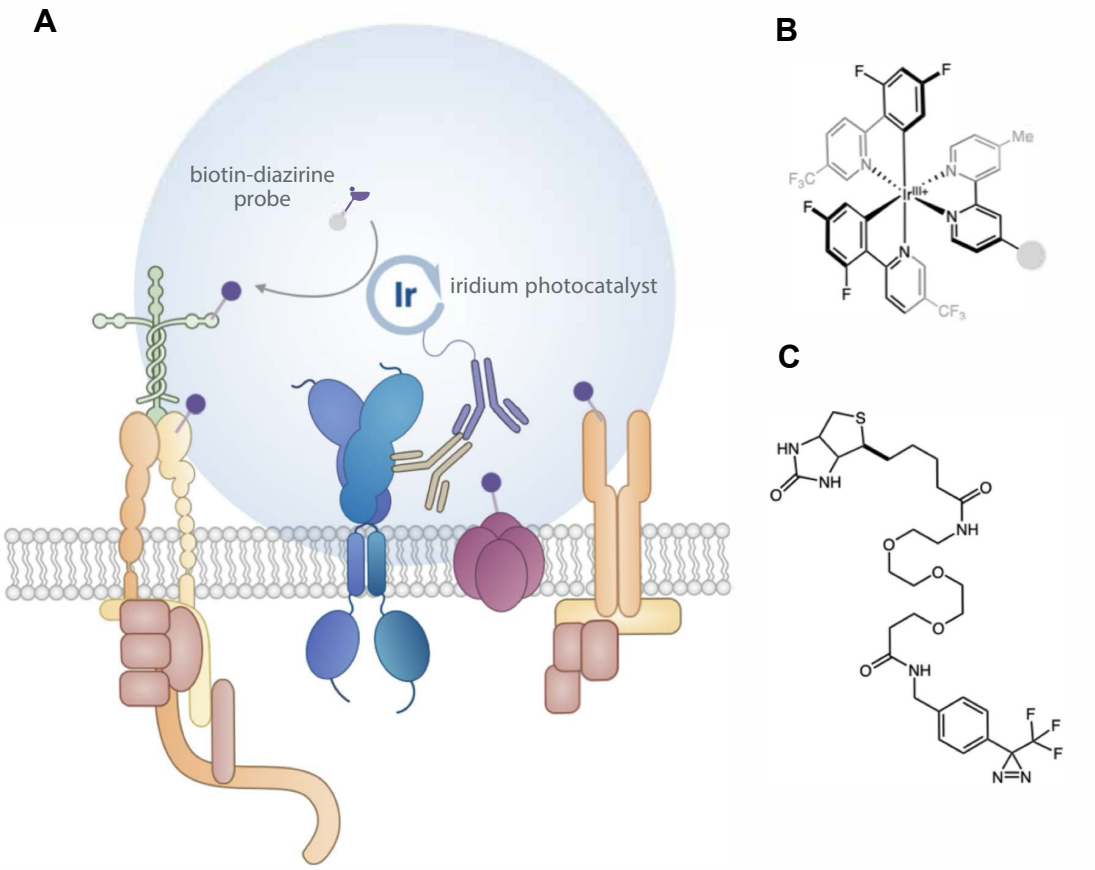


Figure 4.3 µMap workflow for identifying proximal protein networks

(A) Schematic overview of the proximity-dependent biotinylation (µMap) approach for mapping POI-associated protein networks. The workflow illustrates the experimental design showing biotin-dependent labeling system with proximity-dependent biotin ligase fusion protein targeting proteins within the microenvironment. Cellular localization of the biotinylation reaction at the membrane interface. (B, C) Chemical structures of biotin-phenol and related compounds used for proximity labeling. This approach enables identification of transient and stable protein-protein interactions within the native cellular environment.

4.2 Results

4.2.1 Human IL-17RC deficiency reveals unexpected non-inflammatory transcriptional dysregulation

Cytokine receptors are traditionally assumed to function primarily within their canonical signaling cascades, but this assumption may oversimplify their true biological complexity. To assess whether IL-17RC exhibits functions beyond traditional inflammatory signaling, we first turned to unbiased transcriptional profiles of primary fibroblasts derived from IL-17RC-deficient patients. These rare patient populations suffer from chronic mucocutaneous candidiasis due to defective IL-17 signaling. As expected, their fibroblasts displayed severely impaired inflammatory responses following IL-17A treatment; transcripts associated with neutrophil recruitment and NF-$\varkappa$B-dependent signaling, including *Nfkbiz*,*Il6*, *Cxcl1*, and *Cxcl8*, showed blunted (or non-existent) induction. Intriguingly, however, our unbiased pathway analyses indicated widespread dysregulation extending well past canonical inflammatory pathways. In the absence of IL-17A, the most noteworthy and unexpected alterations in *Il17rc*-deficient fibroblasts were tied to metabolic, redox-related, and structural gene networks (processes that were broadly captured via pathway analysis under the umbrellas of epithelial-mesenchymal transitions and basic tumor biology). Among these, several key genes encoding lipogenic proteins (e.g., *Elovl1*, *Fasn*, *Pnpla3*, and *Acly*) were among the first mRNA species to catch our attention, as their expression levels were significantly downregulated in Il17rc$^{-/-}$ fibroblasts. Second, altered redox-related genes (e.g., encoding *IER3, MRPL23, FOLR3, MRAP2, OSGIN1, GADD45A,* and *TXNIP*) were prominent among the top dysregulated mRNA species. And third, coordinated dysregulation

of genes impacting cytoskeletal dynamics and the extracellular matrix (ECM), including *COL13A1, SPP1, CAV2, COL18A1, PLAUR, TIMP1, TGFBR2*, and *SEMA7A*, was likewise suppressed. Naturally, given the many confounding artifacts that plague underpowered patient data and clonal knockout populations, these initial hints of ligand-independent activity warranted due skepticism. Even so, intriguing associations between redox homeostasis, the ECM/cytoskeleton, and metabolic regulation prompted us to ask whether IL-17RC might regulate key cellular responses in the absence of IL-17A/F.

In order to contextualize these findings against the broader IL-17 receptor superfamily, we performed a combinatorial KEGG pathway enrichment analysis intersecting IL-17RA and IL-17RC co-expression gene networks. These associative data mirrored the IL-17-dependent and IL-17RC-associated transcriptional signatures highlighted in Figure 4.4A. Whereas IL-17RA-associated networks centered around classic immune pathways (e.g., formation of neutrophil extracellular traps, B-cell receptor signaling pathway, and leukocyte migration), genes that correlated with IL-17RC were enriched for ECM-receptor interaction pathways, metabolite degradation, lipid/hormone synthesis, and bile secretion (Figure 4.4D,E).

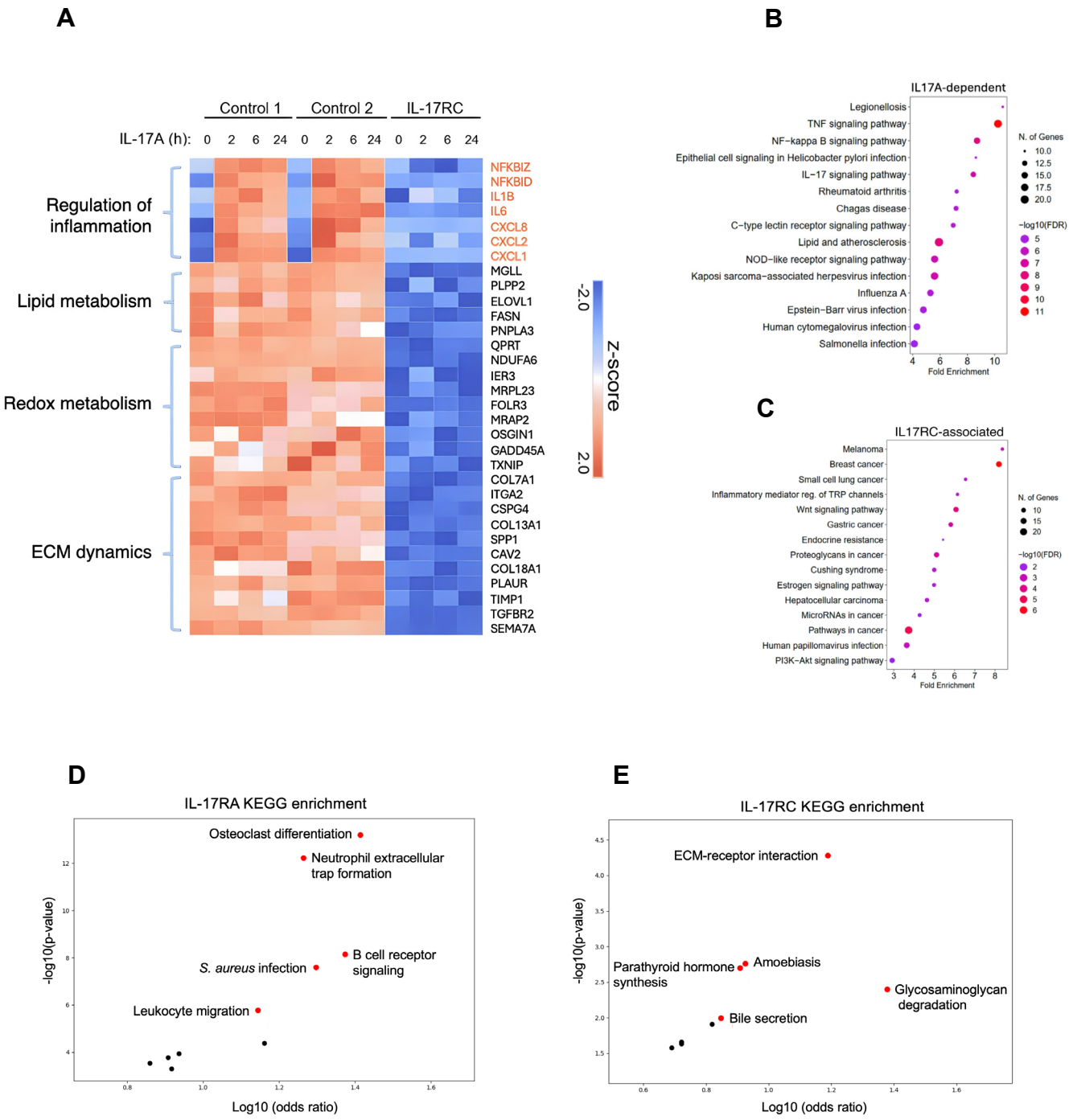


Figure 4.4. Metabolic and ECM-related transcripts are broadly dysregulated in fibroblasts isolated from *Il17rc*-deficient patients

(A) Heatmap of reanalysed data (GSE137108) showing differential gene expression in fibroblasts from *Il17rc*-deficient patients compared to healthy controls following IL-17A stimulation at indicated time points. Top DEGs are grouped by functional categories including regulation of inflammation, lipid metabolism, redox metabolism, and cytoskeletal/ECM dynamics. Expression levels are shown as Z-scores. (B) Pathway enrichment analysis of IL-17A-dependent genes using gene set enrichment analysis. Dot plot shows significantly enriched pathways plotted against fold enrichment. Dot size represents the number of genes in each pathway, and color intensity indicates statistical significance. (C) Pathway enrichment analysis of top IL-17A-insensitive DEGs in fibroblasts isolated from *Il17rc*-deficents patients. (D) KEGG pathway enrichment analysis of genes co-expressed with IL-17RA in tumor cells using Enrichr. (E) KEGG pathway enrichment analysis of genes co-expressed with IL-17RC in tumor cells using Enrichr.

These divergent patterns offered another associative hint that the biological functions of IL-17RC may extend beyond its established partnership with IL-17RA. IL-17RC's association with metabolic and structural pathways was nevertheless intriguing, though, perhaps reflecting that IL-17RC exists as a node integrating immune signals with the fundamental cellular behaviors of energy production, matrix remodeling, and tissue homeostasis.

To link these speculations to a system capable of manipulation and further probe our transcriptional findings at the protein level, we silenced *Il17rc* in murine embryonic fibroblasts (MEFs) with two independent siRNA species and performed quantitative proteomics. This experimental framework allowed us to interrogate the functional consequence of loss of IL-17RC at the protein level while controlling for genetic background, experimental conditions, and off-target effects.

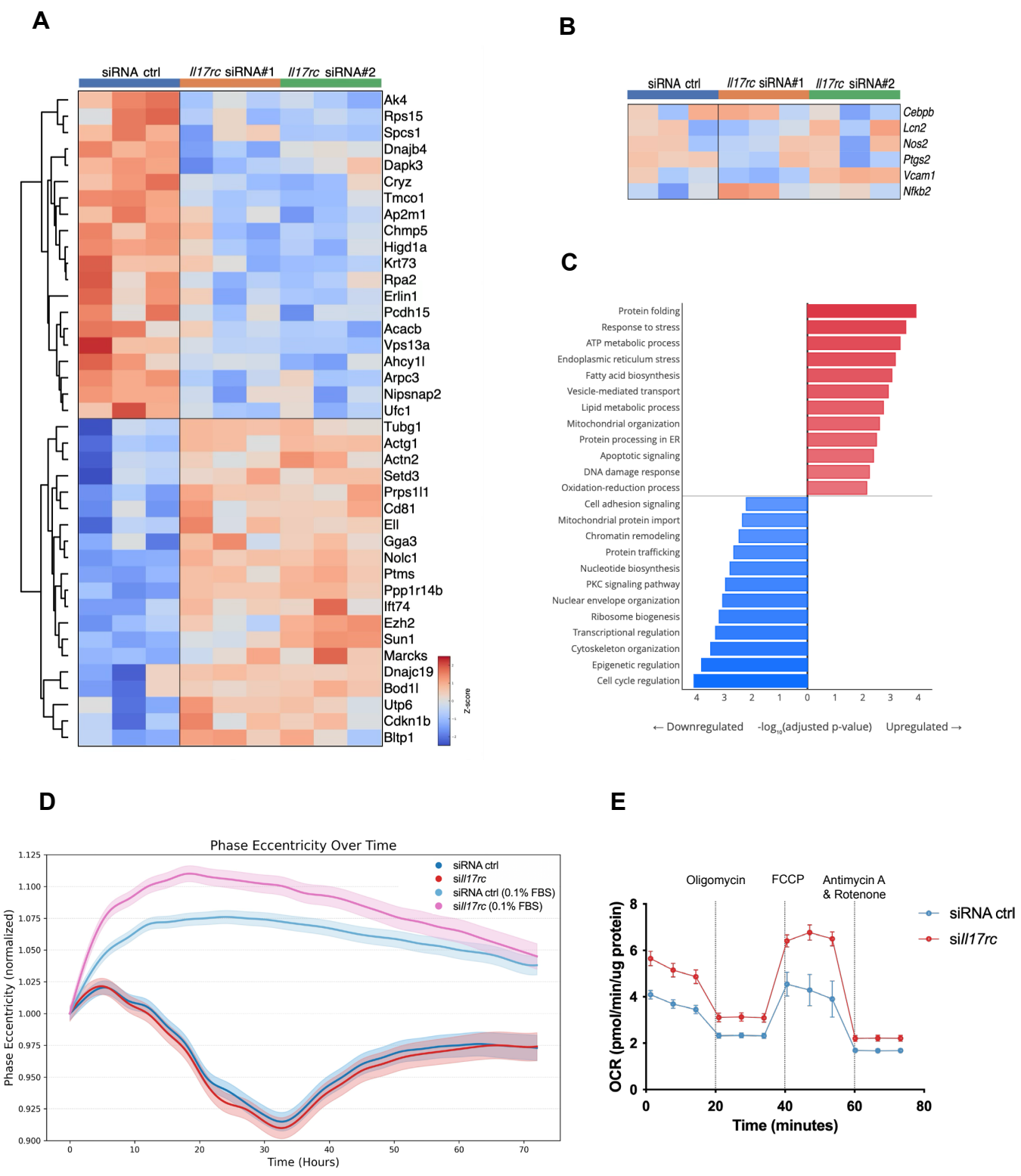


Figure 4.5. Silencing of *Il17rc* disproportionately alters mitochondrial and cytoskeletal networks

(A) Proteomic analysis of MEFs following silencing of *Il17rc* shows downregulation of mitochondrial and actin-remodeling proteins, and upregulation of core cytoskeletal/centrosomal components (n=3). (B) Basal expression of NF-κB target proteins is largely unaffected. (C) Pathway enrichment analysis reveals downregulation of mitochondrial and metabolic networks, and upregulation of pathways related to the cytoskeleton and RNA processing. (D) Live-cell imaging shows that *Il17rc*-deficient MEFs exhibit exaggerated changes in eccentricity (cell shape) following serum starvation, indicating cytoskeletal instability (n=3-4) (E) Seahorse assay reveals that *Il17rc* silencing alters the oxygen consumption rate (OCR), indicating dysregulated mitochondrial respiration(n=4).

Global proteome analysis indicated IL-17RC-dependent regulatory networks that complemented the patient-derived transcriptional associations (Figure 4.5A). Cytoskeletal and ECM-related proteins were among the most consistently up-regulated targets: the key component of the microtubule nucleation complex TUBG1 (γ-tubulin), and both ACTG1 (γ-actin) and ACTN2 (α-actinin-2) exhibited marked increases. (While concomitant increases in these structural components are frequently observed in compensatory responses to cytoskeletal instability, we are currently working to tease apart this mechanism at the time of this thesis submission.) Other proteins such as PRPS1L1 (nucleotide synthesis), ELL, GGA3, and NOLC1 (RNA processing), and CDKN1B/p27KIP1 (cell cycle regulation) also showed increased abundance.

Conversely, we saw significant decreases in the abundance of functionally important metabolic and structural proteins. For ARPC3, a critical part of the Arp2/3 complex that assembles at diverse cellular locations (e.g., lamellipodia edges and the centrosome) before nucleating branched actin networks, abundances decreased dramatically, suggesting broad disruption of cytoskeletal dynamics on multiple levels of organization. The mitochondrial acetyl-CoA carboxylase ACACB (the mitochondrial counterpart of our lipogenic friend from chapter 3, ACACA), also showed significantly decreased abundance alongside a variety of other mitochondrial proteins, including DAPK3 (death-associated protein kinase 3) and HIGD1A. We also noted a decreased presence of proteins involved in endocytosis (e.g., AP2M1, WASHC2) and vesicle trafficking (e.g., VPS13A and ERLIN1).

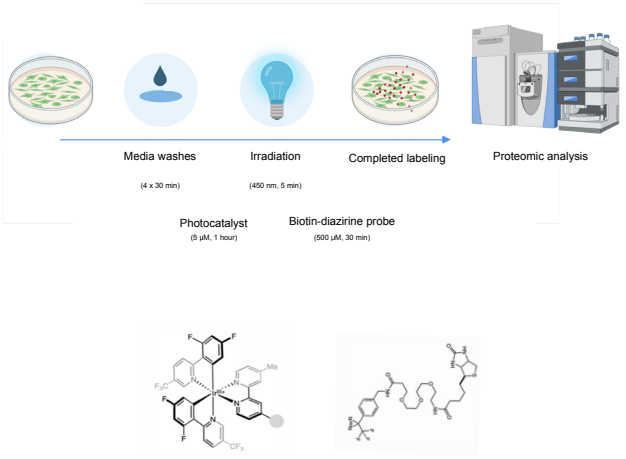
Pathway enrichment suggested that the biological processes most significantly affected represent an intersection with pathways involved in RNA/nucleotide metabolism, cytoskeletal dynamics, mitochondrial function, endocytosis, and cel-

lular stress. In tandem with these defects at the protein level, we observed significant functional disruptions in both mitochondrial respiration (Figure 4.5E) and cytoskeletal responses to stress (Figure 4.5 D). The correlation between human patient transcriptomics and murine cell proteomics provided evidence that IL-17RC deficiency readily alters cellular homeostasis through pathways independent of classical inflammatory signaling. Therefore, our next aim was to determine IL-17RC's direct molecular interaction partners, as we reasoned that a more comprehensive view of these protein-protein interactions would provide invaluable clues to the unappreciated roles of this versatile yet cryptic receptor.

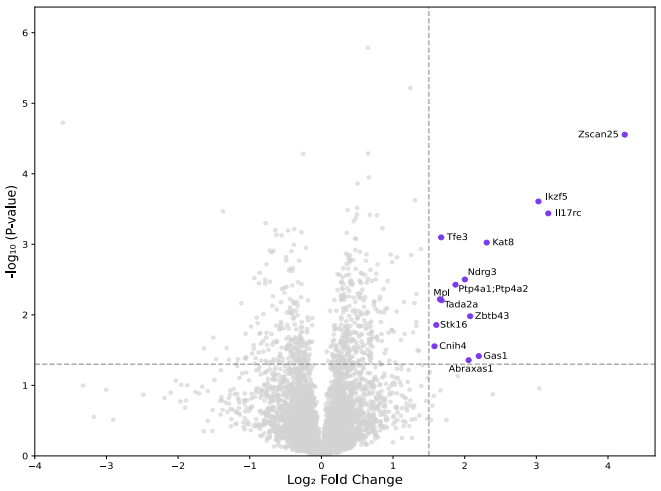
4.2.2 µMap reveals unexpected intracellular protein networks

Given the observation that IL-17RC deficiency altered structural and metabolic signatures, we proceeded to measure the protein-protein interactions that might drive these effects. To this end, we applied microenvironment mapping (µMap), a photocatalytic proximity labeling technology that generates spatially resolved interactomes of proteins at endogenous levels. In cases such as ours, µMap relies on antibodies bound to photosensitizers that can produce highly reactive carbenes, which can then covalently modify nearby proteins within an estimated 10–20 nm radius after activation by visible light.

A



B



C

Protein	Log_2FC	Pathway/Process	Functional annotation
ZSCAN25	4.23	Transcriptional regulation	Zinc finger and SCAN domain-containing protein 25
IKZF5	3.03	Lymphocyte development	Ikaros family zinc finger 5 (Pegasus); B cell differentiation
KAT8	2.31	Epigenetic regulation	Lysine acetyltransferase 8; histone H4K16 acetylation
NDRG3	2.00	Cell differentiation	N-myc downstream-regulated gene 3; lactate-induced hypoxia response
PTP4A1	1.87	Cell signaling	Protein tyrosine phosphatase 4A1; cell proliferation and migration
PTP4A2	1.87	Cell signaling	Protein tyrosine phosphatase 4A2; cell growth regulation
TADA2A	1.68	Transcription coactivation	Transcriptional adaptor 2A; histone acetyltransferase complex
TFE3	1.67	Transcription regulation	Transcription factor E3; lysosomal biogenesis, autophagy
MPL	1.66	Hematopoiesis	Thrombopoietin receptor; megakaryocyte differentiation
TPPP2	1.39	Microtubule dynamics	Tubulin polymerization-promoting protein 2; microtubule bundling
TRIM24	1.33	Transcriptional regulation	Tripartite motif-containing 24; E3 ubiquitin ligase, chromatin reader
ARMC10	1.31	Mitochondrial function	Armadillo repeat-containing protein 10; mitochondrial dynamics
KLLN	1.26	Cell cycle regulation	Killin; p53-regulated DNA replication inhibitor
GTF2H3	1.25	DNA repair/transcription	General transcription factor IIH subunit 3; nucleotide excision repair
WTAP	1.24	RNA modification	Wilms tumor 1-associated protein; m6A RNA methylation complex
MUL1	1.15	Mitochondrial quality control	Mitochondrial E3 ubiquitin ligase 1; mitophagy regulation

D

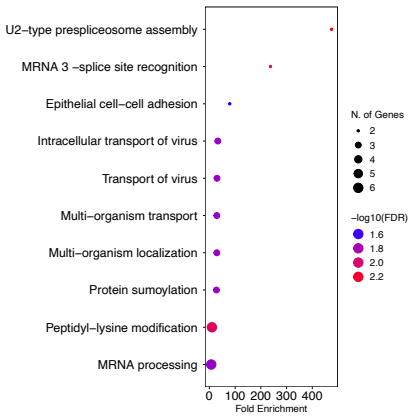


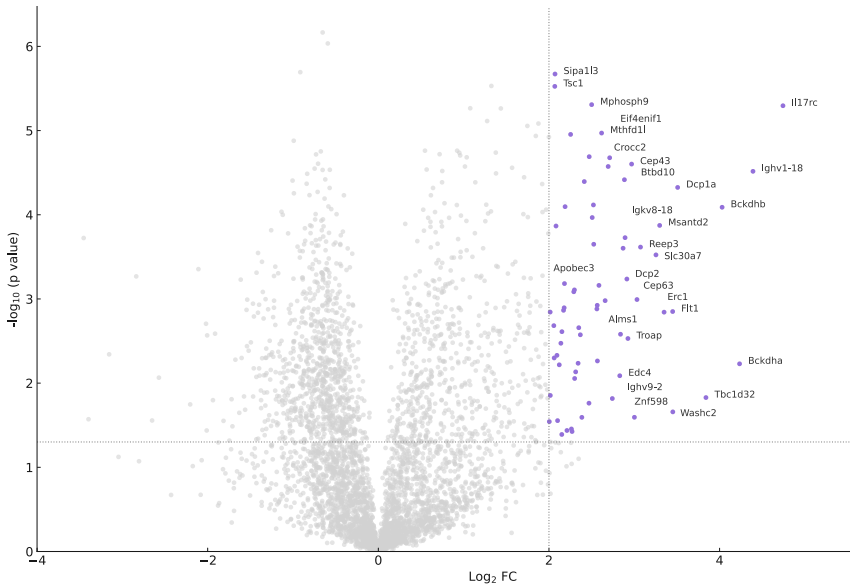
Figure 4.6 | Live-cell proximity labeling identifies the IL-17RC surface interactome.

Microenvironment mapping (μMap) was performed on live murine embryonic fibroblasts (MEFs) to determine the presence of proteins proximal to the extracellular and transmembrane domains of endogenous IL-17RC. (A) General schematic of our live-cell μMAP experments (B) Volcano plot showing protein enrichment from IL-17RC-targeted μMap (n = 3). (C) High-confidence proximal proteins (Log2FC>1), their respective enrichment, and functional annotations.(D) Gene Ontology enrichment analysis of top μMAP-determined candidate proteins (log2FC>1; p<0.01). Invaluable technical assistance was generously provided by Dr. Bloomer

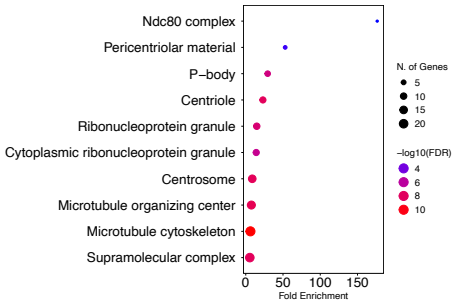
We employed this technology in two complementary ways to comprehensively map the IL-17RC interactome. First, we ran the original µMap ("µMAP classic") approach on live cells, where proteins at the plasma membrane are most readily detected, as antibody-catalyst access to intracellular targets is limited (except for the weak diffusion afforded by mild detergents used in the reaction). To capture the intracellular interactome, we then performed µMapx, which relies on mild fixation and permeabilization conditions to preserve protein interactions while allowing antibody access to cytoplasmic domains. Since the µMapx experiments in fixed cells gave the most unexpected results, revealing abundant intracellular and perinuclear residing proteins, we focus our detailed discussion on these µMapx findings. This dual µMap/µMapx strategy offered key advantages: it avoided detergent-induced artifacts that disrupt membrane organization, maintained spatial relationships between proteins, and captured transient protein-protein interactions that would otherwise be lost during conventional immunoprecipitation workflows.

Both approaches followed similar experimental protocols: in-house-validated antibodies specific for IL-17RC were applied, unbound antibodies were removed by washing, photocrosslinking with 450 nm light was performed to covalently capture proximal proteins, and the crosslinked complexes were extracted for mass spectrometry analysis. Controls validated our results, including isotype-matched antibodies to assess non-specific binding and parallel non-illuminated samples to distinguish light-dependent crosslinking from background interactions.

A



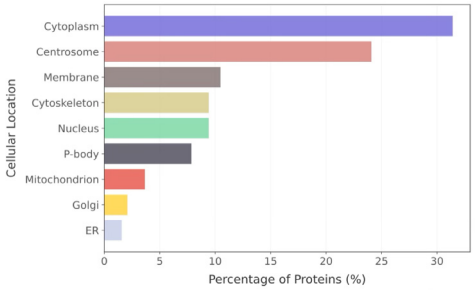
B



C

Protein	Log_2FC	Pathway/Process	Functional annotation
BCKDHA	4.23	Amino-acid catabolism	BCKD E1 α subunit; branched-chain amino-acid catabolism
BCKDHB	4.03	Amino-acid catabolism	BCKD E1 β subunit; branched-chain amino-acid catabolism
TBC1D32	3.84	Ciliogenesis & hedgehog	TBC-domain protein in Sonic Hedgehog pathway
DCP1A	3.51	mRNA decay	Cap-removal enzyme in mRNA turnover
WASHC2	3.45	Endosomal trafficking	WASH complex subunit; endosomal transport & actin dynamics
FLT1	3.45	Angiogenesis	VEGFR1; vascular endothelial growth factor receptor 1
ERC1	3.35	Synaptic & NF-κB signalling	Active-zone scaffold; cadherin & NF-κB regulator
MSANTD2	3.30	Unknown	Myb/SANT DNA-binding protein; unknown function
REEP3	3.07	ER morphology	Receptor expression-enhancing protein 3; ER tubulation
CEP63	3.03	Cell division	Centrosomal protein; centriole duplication & spindle assembly
ZNF598	3.00	Translation quality control	Zinc finger protein 598; ribosome-associated quality control
CEP43	2.97	Ciliogenesis	Centrosomal protein 43; centriolar satellite organization
TROAP	2.93	Cell division	Trophinin-associated protein; spindle assembly and cytokinesis
DCP2	2.91	mRNA decay	mRNA-decapping enzyme 2; 5' cap structure removal
BTBD10	2.88	Motor protein regulation	BTB/POZ domain-containing protein 10; ATPase activator

D



E

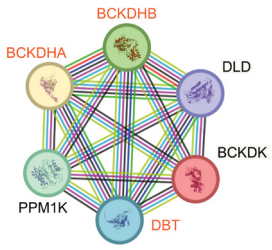


Figure 4.7 The intracellular IL-17RC interactome in MEFs shows extensive overlap with centrosomal, mitochondrial, and mRNA-processing networks

(A) Volcano plot of μMapx proximity labeling results showing IL-17RC-proximal proteins in MEFs under basal conditions (n = 3). (B) Gene Ontology enrichment analysis of top μMAPx canditates (p<0.01; log2FC>2). (C) Top 15 IL-17RC interactors (p<0.01) (D) Distribution of IL-17RC-proximal proteins across subcellular compartments. Values represent percentage of total identified proteins localizing to each compartment based on validated annotations (COMPARTMENTS Curated Protein Localization Evidence Scores 2025 dataset) (E) Network analysis of top two canditates, as ranked by fold size, from STRING database.

Following extensive optimizations of the protocol, trials with more than a few antibody clones, and subsequent analysis, we were first intrigued by the sheer number of IL-17RC-centrosome interactions that emerged across our µMapx experiments (4.7A). Natives of this critical organelle, such as CEP150, CEP170, CEP152, CEP192, CDK5RAP2, and PCNT (pericentrin), were consistently among the top hits in our proximity investigations. These proteins shape cellular architecture by organizing pericentriolar material and nucleating microtubules.

A second noteworthy result was a high enrichment of mitochondrial proteins, particularly those associated with the inner mitochondrial membrane and the mitochondrial matrix. The branched-chain α-ketoacid dehydrogenase complex requires BCKDHA, BCKDHB, and DBT for amino acid catabolism. MTHFD1L converts 10-formyltetrahydrofolate to formate. Given the absence of proteins from the outer mitochondrial membrane in our top hits list, the specific enrichment for proteins associated with the inner mitochondrial membrane suggested a more functional and localized link.

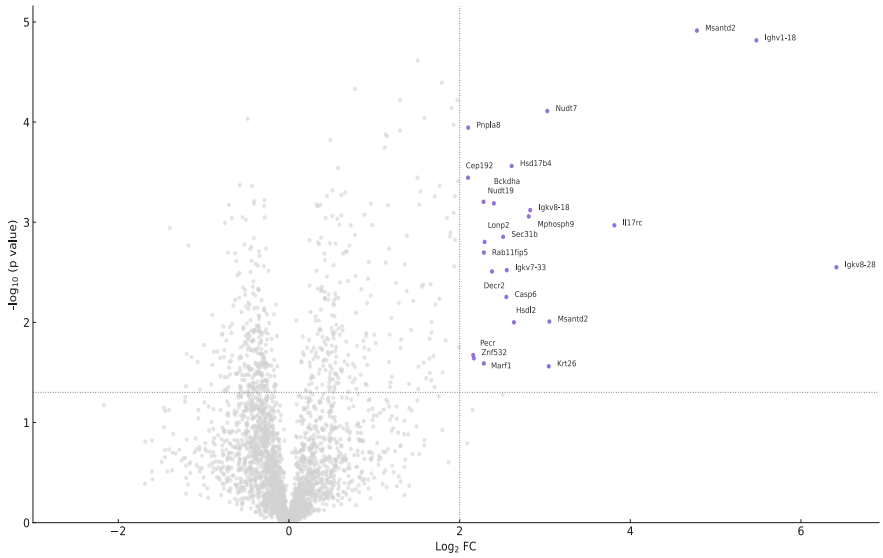
RNA-binding proteins and processing body (P-body) components were the third major category of IL-17RC-associated proteins (4.7A,B). Consistent levels of translational regulators, including GIGYF2 (GRB10-interacting GYF protein 2), ZNF598, and DCP1A (mRNA-decapping enzyme), were consistently enriched in our µMapx experiments. This finding raises the possibility that IL-17RC may constitutively participate in post-transcriptional regulation, as P-bodies are cytoplasmic ribonucleoprotein granules that are found in response to stress and are involved in both mRNA storage and degradation. Considering the intricate work recently performed by Li et al. and others showing that canonical IL-17-based signaling often intertwines with mRNA metabolism, it is tempting to speculate that IL-17RC may coordinate inflammatory signals with stress signals, even in the

absence of its ligands. Alternatively, these constitutive processing body-IL-17RC associations may instead require further assistance from ACT1, IL-17RA and/or other members of the canonical pathway for downstream functional relevance.

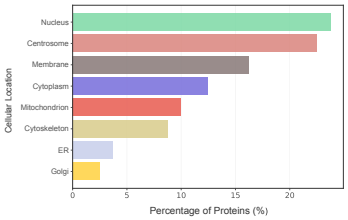
Intriguingly, we also identified apparent constitutive co-localization between IL-17RC and proteins such as NEMO and other members of the NF-$\varkappa$B cascade (Figure 4.7A). This unexpected finding suggests that IL-17RC may retain proximity to key inflammatory signaling machinery even in the absence of ligand stimulation, potentially priming cells for rapid inflammatory responses upon cytokine engagement.

Lastly, we also identified multiple cytoskeletal regulators in addition to centrosomal proteins. Formins (FMN1), the formin-binding protein COBLL1, and various components of the WASH complex were enriched; these include proteins involved in the assembly of endosomal actin. Our identification of ARPC3 as a direct interactor is worth further investigation since we found that its expression was affected upon loss of IL-17RC (Figure 4.5A). This provides a mechanistic link between the presence of IL-17RC and the organization of the actin cytoskeleton.

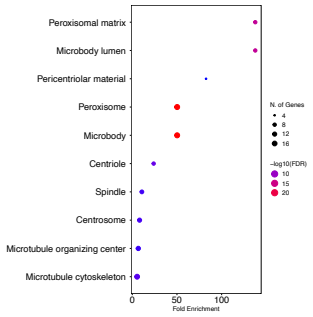
A



B



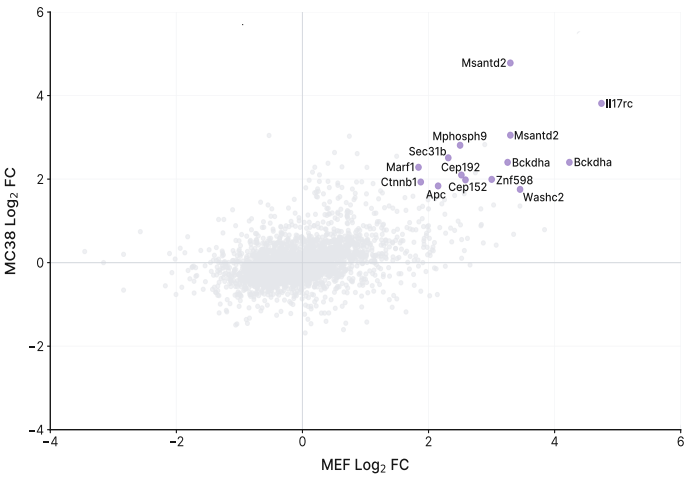
C



D

Protein	Log_2FC	Pathway/Process	Functional annotation
MSANTD2	4.78	Unknown	Myb/SANT DNA-binding protein; unknown function
NUDT7	3.03	Nucleotide metabolism	Nudix hydrolase 7; CoA diphosphatase, peroxisomal
MPHOSPH9	2.81	Ciliogenesis	M-phase phosphoprotein 9; negatively regulates cilium assembly
HSDL2	2.64	Lipid metabolism	Hydroxysteroid dehydrogenase-like 2; peroxisomal metabolism
HSD17B4	2.61	Fatty acid β-oxidation	17β-hydroxysteroid dehydrogenase 4; peroxisomal multifunctional enzyme
CASP6	2.55	Apoptosis	Caspase-6; executioner caspase, neurodegeneration
SEC31B	2.51	Vesicle trafficking	SEC31 homolog B; COPII vesicle coat component
BCKDHA	2.40	Amino-acid catabolism	BCKD E1 α subunit; branched-chain amino-acid catabolism
DECR2	2.38	Fatty acid metabolism	Peroxisomal 2,4-dienoyl-CoA reductase; unsaturated fatty acid β-oxidation
LONP2	2.29	Protein quality control	Lon protease 2; peroxisomal matrix protein degradation
RAB11FIP5	2.28	Membrane trafficking	RAB11 family-interacting protein 5; endocytic recycling
NUDT19	2.28	Nucleotide metabolism	Nudix hydrolase 19; CoA diphosphatase, ER-localized
PNPLA8	2.10	Lipid metabolism	Patatin-like phospholipase domain-containing 8; phospholipase A2 activity
CEP192	2.10	Centrosome organization	Centrosomal protein 192; mitotic spindle organization, PLK1 recruitment
CEP152	1.98	Centrosome duplication	Centrosomal protein 152; PLK4 recruitment, centriole biogenesis

E



4.8 µMapx analysis of IL-17RC in MC38 cells shows a notable enrichment of centrosomal and mitochondrial proteins

(A) Proteins that colocalize with IL-17RC are identified by proximity-labeling endogenous IL-17RC in fixed, permeabilized MC38 cells using µMapx. Volcano plot displays significantly enriched neighbors. (B) The subcellular localization of IL-17RC-proximal proteins, as annotated using the COMPARTMENT database. (C) Top MC38 µMapx hits with GO Cellular Component enrichment ($p<0.01$; log2FC >2) (D) FC Top high-confidence candidates that µMapx recovered, racked by fold change. (E) Cross-cell analysis of µMAPx runs shows that MC38 cells and mouse embryonic fibroblasts share top candidates.Invaluable technical assistance was generously provided by Dr. Bloomer

Compartment enrichment analysis added a more quantitative aspect to the unexpected intracellular localization of IL-17RC. In MEFs, 25–30% of identified interactors were centrosomal, compared to roughly 10% of identified interactors that were ascribed to the plasma membrane. The cytoplasm broadly corresponded to 35% of top interactions, out of which there were contributions from the cytoskeleton (10%), P-bodies (8%) and mitochondria (5%). MC38 cells showed a similar orientation with even more enrichment for nuclear (23%) and centrosomal (20%) compartments (Figure 4.8A, B). This distribution stood in stark contrast to computational predictions, which assign IL-17RC universally to the plasma membrane (Figure 4.9A–B).

4.2.3 Microscopy illuminates IL-17RC's intracellular localization

The overall intracellular interactome was surprising and directed us to explore IL-17RC's subcellular distribution using multiple orthogonal approaches. As mentioned, computational algorithms predict localization based on sequence features of proteins with high confidence, yet we were compelled by contradictory experimental evidence.

We next consulted The Human Protein Atlas to determine IL-17RC subcellular localization via immunofluorescence-based localization data from validated antibodies. The hIL-17RC results provided strong experimental evidence of localization to microtubules and centrosomes, but a considerably weaker signal for the plasma membrane. The experimental data also revealed high and low confidence ratings for microtubule and centrosome localization, respectively, with plasma-membrane localization visible only in computational predictions. The discrepancy between prediction and observation was difficult to ignore: computational algo-

rithms assigned IL-17RC to the plasma membrane based on its predicted signal peptide and transmembrane domain, but our experimentally-based approaches consistently showed localization in the intracellular compartment, demonstrating potential limitations in relying on computational predictions for proteins with complex trafficking or functional states (Figure 4.9A–B).

To back our proximity proteomics data with more tangible visualizations, we next pursued several microscopy approaches. Immunofluorescent microscopy using knockout-validated IL-17RC-specific antibodies consistently showed perinuclear staining patterns in three cell types that were selected for their high expression of IL-17RC: MEFs, B16 melanoma cells, and MC38 colorectal cancer cells (Figure 4.9C-D).

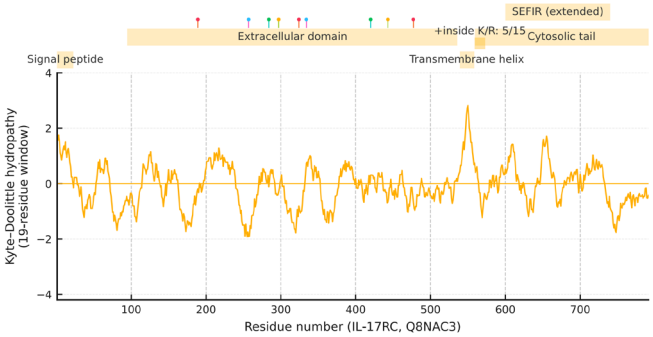
A

Experimental evidence and computational predictions for human IL-17RC subcellular localization

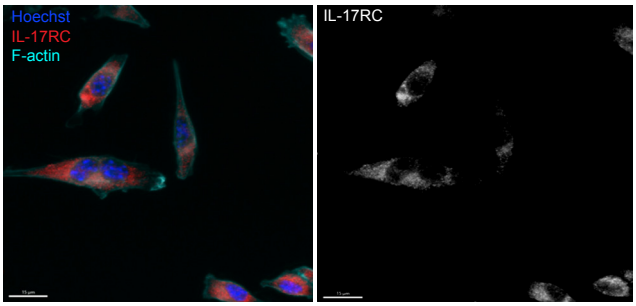
Evidence Type	Compartment	Method/Source	Score/Evidence	Confidence
Computational	*Plasma membrane*	PSORT	24/32	★★★☆☆
	Endoplasmic reticulum	PSORT	4/32	★☆☆☆☆
	Extracellular region	PSORT	1/32	★☆☆☆☆
	Golgi apparatus	PSORT	1/32	★☆☆☆☆
	Peroxisome	PSORT	1/32	★☆☆☆☆
	Mitochondrion	PSORT	1/32	★☆☆☆☆
Experimental	*Microtubule*	HPA	**Strong:** 1 antibody Very weak: 1 antibody	★★★☆☆
	Centrosome	HPA	**Weak:** 1 antibody Very weak: 1 antibody	★★☆☆☆

Subcellular localization evidence for human IL-17RC from experimental validation and computational prediction methods. **Experimental:** Human Protein Atlas (HPA) immunofluorescence microscopy data with antibody validation scores. **Computational:** Sequence-based predictions using PSORT (features: number supporting/32 total). Confidence ratings follow the COMPARTMENTS database scoring scheme (★ = low confidence, ★★★★★ = high confidence).

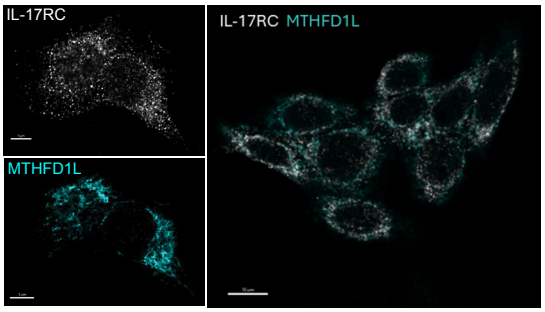
B



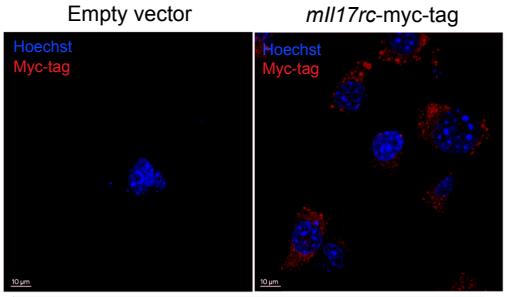
C



D



E



F

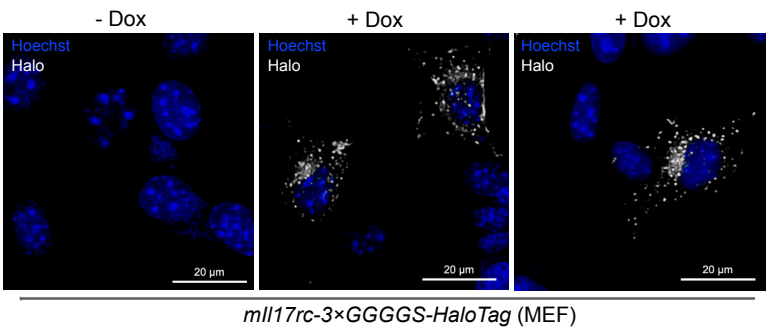


Figure 4.9 Computational and empirical evidence reveals discrepancies in IL-17RC subcellular localization

(A) Summary of *in silico* predictions (PSORT) and Human Protein Atlas (HPA) immunofluorescence assignments for human IL-17RC, (B) Kyte–Doolittle hydropathy profile and topology features for hIL-17RC (C) Representative confocal images of endogenous IL-17RC in murine embryonic fibroblasts (MEFs) (D) Endogenous IL-17RC compared with the mitochondrial marker MTHFD1L in B16 (melanoma) and MC38 (colorectal carcinoma) cells; (E) Transient expression of mouse Il17rc–Myc in MEFs. (F) Doxycycline-inducible *mIl17rc*–3×GGGGS–HaloTag in MEFs visualized with HaloTag ligand.

The perinuclear localization pattern was prominent as IL-17RC appeared as punctate cytoplasmic structures with enrichment in regions where centrosomes and mitochondria typically cluster. It is also important to note that these experiments were conducted without the presence of IL-17A or IL-17F in the media. Given that the intracellular IL-17RC pool was found during basal states in multiple cell types, we next hypothesized that this interaction is a constitutive feature of the protein, rather than hinging fully on inflammatory signaling events.

To mitigate additional possible antibody artifacts and allow for dynamic-tracking visualization, we created a tetracycline-inducible system that expresses IL-17RC with a C-terminal HaloTag. The tetracycline system allowed us to time IL-17RC expression while maintaining nearly physiological levels of the protein. Induction of our IL-17RC construct revealed perinuclear colocalization and appeared to phenocopy our immunofluorescent staining of endogenous protein (Figure 4.9F). In our imaging experiments, IL-17RC localized minimally at the plasma membrane compared to intracellular compartments. Our colocalization approach confirmed that these associations were further supported through proximity proteomics, suggesting that IL-17RC-positive structures partially aligned with γ-tubulin at centrosomes as well as with antibody-labeled mitochondria and associated with other intermediate filament network markers. Intriguingly, IL-17RC appeared to coalesce at contact sites between organelles, suggesting possible roles in inter-organellar communication (Figure 4.9C-F).

4.2.4 IL-17RC ablation disrupts cytoskeletal architecture and nuclear organization

To interrogate the functional consequences of the intracellular localization of IL-17RC on the cell, we created clonal IL-17RC knockout MEF lines with CRISPR-

Cas9. gRNAs were specifically designed towards two separate regions of the murine Il17rc gene.

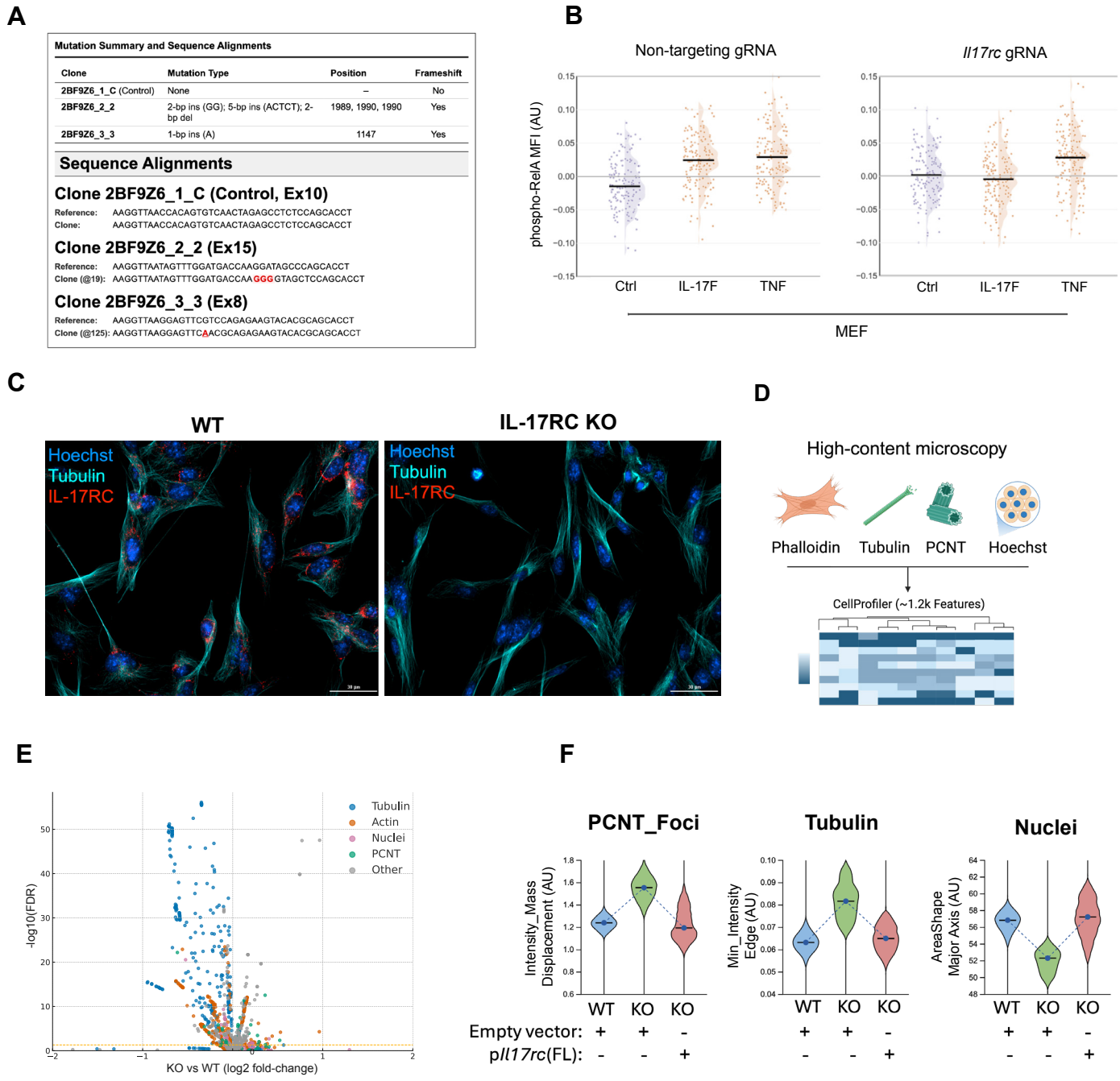


Figure 4.10 IL-17RC ablation disrupts centrosome-nucleus coupling and cytoskeletal organization

(A) CRISPR–Cas9 validation of Il17rc knockout clones in mouse embryonic fibroblasts (MEFs). Table and Sanger alignments summarize frameshift-inducing indels in independent clones. (B) Canonical signaling evaluation, as measured via phospho-RelA induction, in MEFs transduced with a non-targeting gRNA or Il17rc gRNA after stimulation with IL-17F (100ng/mL) or TNF(20ng/mL) for 30 minutes. (C) Immunofluorescence images of WT and Il17rc-KO MEFs stained for alpha tubulin (cyan) and IL-17RC (red).(D) High-content microscopy workflow, which entailed phalloidin/F-actin, α-tubulin, PCNT (pericentrin), and Hoechst 33342 staining, imaging with fluorescence, and quantification via CellProfiler. (E) Global phenotypic comparison (KO vs WT) shown as a volcano plot of single-cell imaging features. Features are color-coded by channel. (F) Violin plots summarize top feture hits from genetic rescue experiments across WT + empty vector, KO + empty vector, and KO + full-length Il17rc vector [pIl17rc(FL)]. (n=3-4)

After single-cell sorting, we expanded clonal populations and sequenced them to validate that we had multiple clones with true frameshift mutations. Clone 2BF9Z6_1_C (Figure 4.10)served as a control and showed no mutations, while clones 2BF9Z6_2_2 (2-bp and 5-bp insertions), 2BF9Z6_3_3 (1-bp insertion) and 2BF9Z6_4_10 (5-bp insertion and 4-bp insertion) were independent knockout lines showing confirmed frameshifts that abolished IL-17RC protein expression.

Next, we conducted high-content imaging analysis with automated quantification of over 1000 morphological features and observed clear and orchestrated defects in cellular architecture in IL-17RC knockout cells.

Nuclear morphology changed dramatically. IL-17RC knockout cells displayed reduced nuclear major axis length (Figure 4.10F), increased circularity, and altered maximum Feret diameters. These changes reflect abnormal nuclear-cytoskeletal connections, with the nucleus as a whole becoming more rounded and less elongated; phenotypes typically associated with loss of mechanical tension or disruption of the cytoskeletal framework.

Microtubule morphology was greatly disrupted as well (Figure 4.10E). For the quantitative measure of tubulin stain intensity around the periphery of the nuclei, we observed significant alterations to the minimum edge intensity, suggesting that the typical perinuclear microtubule cage was depleted of integrity or had gaps. This is notable given the upregulation of γ-tubulin in our proteomics data, suggesting increased tubulin expression alone does not address gaps or deficits in organization.

Centrosome morphology was abnormal in our KOs, too. Localized PCNT events, relative to the centroids of the nucleus, displayed a significant mass displacement indicating loss of coupling of the centrosome to the nuclear envelope

that is typically tight (Figure 4.10F). This may also explain many of the cytoskeletal abnormalities that we observed.

The observations, driven by unbiased analysis of 100s of features, provided evidence that IL-17RC ablation altered the tension balance in the cytoskeleton-microtubule networks. There, alpha tubulin was observed to be more tightly pulled around the nucleus, nuclei became more circular, and there was increased polarity of the actin in the cytoskeleton (Figure 4.10E,F). These distinct changes indicate an alteration in the mechanical homeostasis of the cell.

4.2.5 Centrosomal scaffolding defines IL-17RC's localization

The identification of centrosomal proteins in our proximity proteomics dataset and the centrosome-associated phenotypes of the knockout cells led us to fully investigate this interaction network. Consistent across all of our µMapx datasets and imaging modalities, the centrosome organizers have always been an enriched adjacent partner of IL-17RC. The enrichment values in MEFs were: CDK5RAP2 (1.37-fold), CEP152 (2.59-fold), CEP170 (1.99-fold), CEP192 (2.52-fold), CEP63 (3.03-fold), NIN (2.08-fold), and PCNT (2.17-fold). MC38 demonstrated similar patterns with much more robust assemblies for CDK5RAP2 (1.36-fold), CEP152 (1.58-fold), and CEP192 (2.10-fold).

With such strong evidence for the associations from the centrosomal proteins, it would be reasonable to propose that IL-17RC associates with the centrosome as an organellar complex instead of individual proteins in isolation. Additionally, the depth of enrichment also corresponded to the weight of the phenotype and how dramatically the functional consequences were altered in cells deficient in IL-17RC.

To demonstrate causality, we conducted a set of rescue experiments reintroducing full-length IL-17RC back into the knockout cells using cDNA vector. Reintroduction of IL-17RC was able to restore functional cellular architecture in remarkable fashion: following genetic rescue, nuclear morphology parameters returned to near wild-type values, and the rescued cells exhibited greater nuclear elongation and lower circularity (Figure 4.10F). The perinuclear microtubule network was partially restored, as well, as indicated by the α-tubulin edge intensity values, which were equivalent to wild-type.

The volcano plot evaluation comparing knockout and rescue conditions indicated that the most easily rescuable features, PCNT localization, α-tubulin organization, and nuclear shape, were also the exact features that had the highest correlations associated with the centrosomal protein interactions that we identified in our proteomics data. The specificity and overall ability to rescue features suggest that the phenotypes we identified were due to IL-17RC loss and were not canonical off-target effects from Cas9 cutting or clonal variation.

4.2.6 Ligand engagement remodels the intracellular localization of IL-17RC

One of the questions that arose from our assessment of the intracellular functions of IL-17RC was this: how do the IL-17RC intracellular non-canonical functions relate to typical cytokine signaling? With this in mind, we next performed µMapx experiments on MEFs that were treated with either IL-17A or IL-17F for 30 minutes and were then fixed and proximity labeled.

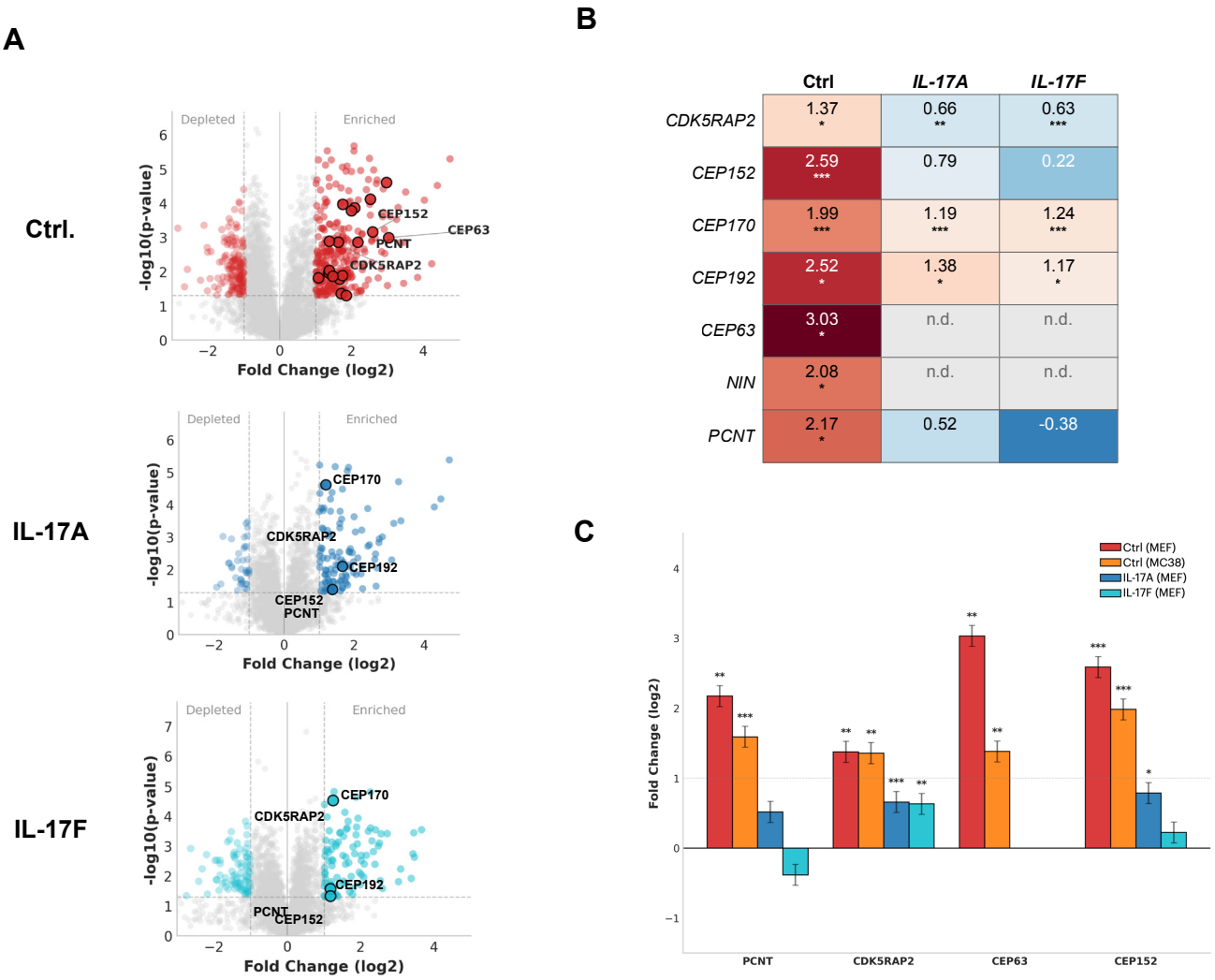


Figure 4.11 Ligand engagement displaces IL-17RC from centrosomal scaffolds.

(A) Volcano plots of data from µMapx experiments performed in MEFs following 30-min stimulation with IL-17A or IL-17F (100 ng/mL), depicting reduced proximity of IL-17RC to centrosomal proteins versus unstimulated control. (B) Heat map summarizing fold-enrichment under each condition; asterisks denote significance (n.d. = not detected).(C) Bar plots compare baseline centrosome adjacency in MEFs and MC38 cells and its attenuation in MEFs upon IL-17A/F treatment for selected proteins.Invaluable technical assistance was generously provided by Dr. Bloomer.

Remarkably, both treatments exhibited a distinctly different interaction profile for IL-17RC (Figure 4.11) . Enrichment for centrosomal proteins was greatly altered: PCNT enrichment changed from a log2 fold change of 2.2 to 0.52 (IL-17A) and, in case of IL-17F treatment, -0.38 fold. Whereas CEP152 followed a similar trend (Figure 4.11B,C). Importantly, this ligand-mediated dissociation appeared to be specific. Although associations to mitochondrial proteins were mostly retained, some cytoplasmic interactions actually increased. The selective loss of known centrosomal interactions could indicated that IL-17RC toggles between structural and signaling functions depending on ligand availability.

4.3 Discussion and Conclusions

Our comprehensive study has uncovered an unanticipated aspect of cytokine receptor biology, showing that IL-17RC is primarily an intracellular regulator of cellular structure and metabolism, not just a plasma membrane co-receptor. We gathered convergent evidence from patient transcriptomics, proximity proteomics, super-resolution imaging, and functional genomics, showing that IL-17RC coordinates a complex program at the centrosome while also regulating mitochondrial metabolism and, potentially, RNA processing.

By observing that less than 10% of IL-17RC localizes to the plasma membrane at the steady state, we are tempted to reevaluate traditional views of receptor topology. Our ongoing pursuit to further validate the more controversial µMAPx results will undoubtedly bring clarity to this matter, despite the various technical hurdles that have cropped up throughout these investigations. Nevertheless, these data support a model where the majority pool of IL-17RC is sequestered within the cytoplasm. Moreover, this intracellular pool of IL-17RC seems to be constitutive and does not explicitly rely on expression of, or engagement with, its

known ligands.

The functional role of IL-17RC's association with the centrosome is highlighted by the severe defects in cytoskeleton structure upon loss of IL-17RC. These defects include disrupted nuclear structures, disorganized microtubules, and misplaced centrosomes, which may in turn point towards an unrecognized role of IL-17RC around the centrosome to maintain cellular structure. These structural roles of IL-17RC appear to be mechanistically separate from the canonical IL-17 signaling pathways.

The observation that IL-17A and IL-17F treatment induces IL-17RC dissociation from the centrosome suggests an elegant regulatory mechanism by which cells toggle between homeostatic and inflammatory programs. IL-17RC organizes cellular structure by associating with the centrosome as part of the default state; when it becomes engaged by ligand, that organization is disrupted to provide an opportunity for inflammatory signaling.

The evolutionary conservation of the intracellular functional activities of IL-17RC is compelling from our assessments of data comparing human patients and murine models, and it provides a strong rationale for a model in which IL-17RC's structural and metabolic functions are real, fundamental aspects of cellular physiology.

These observations are also a result of technical advances; for example, we employed µMap proximity proteomics to track transient and compartmentalized interactions that would likely have been missed using classic methods. Additionally, we used quantitative imaging with pipelines that allowed, beyond qualitative descriptions, a means to quantitatively define specific and measurable phenotypes. This approach should be beneficial going forward in exploring other presumed surface receptors assumed to be missing intracellular roles.

At the time of this thesis submission, there are many new and exciting avenues to pursue, each guided by what we and others have recently observed. First, what governs how IL-17RC is allocated to surface and intracellular pools? Our data suggest retention mechanisms are at play, but we do not fully understand these mechanisms yet. Additionally, how do the functional modules of IL-17RC (i.e., cytokine binding, signal transduction, and structural organization) coordinate their tasks? And last, under what physiological contexts do structural effects prevail over signaling effects or vice-versa?

Our ongoing work aims to clarify IL-17RC's underappreciated role as a multifunctional protein that blends immune signaling roles with essential aspects of basic cell biology. Understanding where IL-17RC resides within the cell, and the cellular states that determine its localization, moves us from a simplistic model to a more complex, nuanced grasp of receptor biology. In this light, and from multiple empirically aligned viewpoints, we see IL-17RC as dynamic protein that deftly weaves immune-mediated signaling with vital cellular processes seemingly unrelated to host defense.

Chapter 5

Discussion and Conclusions

Here, we found that members of the IL-17 cytokine family control central determinants of cellular and metabolic health, including nutrient utilization, thermoregulation, fatty-acid metabolism, and diet-induced weight gain. Deletion of IL-17A or IL-17A/F in males was accompanied by significantly lowered core body temperature across the active cycle. While indirect calorimetry highlighted IL-17-dependent effects consistent with defective carbohydrate metabolism. To our surprise, IL-17A/F deficiency in female mice corresponded with increased core body temperature during the active phase.

We then proceeded to hypothesize that IL-17A/F- and sex-dependent control of lipid metabolism in adipose tissue could, at least in part, account for these results. Through interrogation of our own animal models, as well as publicly available omics, we found that either adipocyte-specific knockout of*Il17rc* or global deletion of*Il17a/f* disrupted a central pathway connecting carbohydrate processing with lipid anabolism. Transcriptional regulation of *de novo* lipogenesis, which facilitates the conversion of carbohydrates into long-chain fatty acids, was severely compromised in male but not female,$Il17a/f^{-/-}$ mice. A similar phenomenon was evident in the liver, which, together with adipose tissue, is a critical site of DNL activity in rodents and humans (Iroz et al., 2017). Given that levels of both tissue triglycerides and endogenous lipids have a strong influence on metabolic

health, we believe that future investigation into IL-17's function in triglyceride mobilization and accumulation is a worthy pursuit, one that will continue to add depth to the field of immunology and health in general.

These tissue-specific actions concur with previous findings that IL-17A and IL-17F induce lipolysis within adipose tissue and, combined with our evidence, now involve IL-17 signaling within hepatic lipogenesis as well. These immunometabolic functions give further weight to the idea that cytokine-lipid metabolic interactions should be directly measured in larger patient cohorts undergoing IL-17–targeted treatments.

This crosstalk demonstrates that metabolic homeostasis is vulnerable to immune disturbances. If the IL-17 pathway coordinates nutrient processing with immune surveillance, then neutralization of this signal (as routinely occurs in the clinic) may alter the very cellular programs that support tissue tolerance or predispose patients to metabolic disease. Accordingly, we advocate for enhanced metabolic monitoring as an integral component of the growing number of clinical trials examining IL-17 inhibition.

Next, we observed that proximity-based proteomics pointed to a novel function for IL-17RC as an intracellular scaffold. Under basal conditions, the receptor constitutively localized with centrosomal proteins, central mitochondrial enzymes, and with the key constituents of processing bodies. This molecular geography positions IL-17RC at the crossroads of cellular structure and metabolism, connecting microtubule organization with bioenergetics. The structural significance of these connections feel in line with observations made in*Il17rc*-deficient cells, which had a more rounded nucleus, displaced centrosome, and disrupted microtubule networks; phenotypes more suggestive of mechanical than of primary inflammatory malfunction.

These findings suggest that IL-17RC may function as a structural regulator of cellular behavior. In this model, IL-17RC physically associates with both cell cycle and stress-sensing machinery, coordinating structural integrity with homeostatic demands. We speculate that these molecular associations may endow structural stability during barrier maintenance. Then, following ligand engagement, these associations become disrupted, redirecting cellular resources from housekeeping towards immune defense. In diseases characterized by disordered tissue remodeling, such as fibrosis or cancer, this regulatory mechanism is especially intriguing, as a loss of the structural control can quickly give rise to pathological proliferation.

Ligand availability reshaped this physical proximity, as treatments with IL-17A/F appeared to subvert centrosomal connections. While under the same treatment conditions, mitochondrial interactions remained largely intact, implying a regulated redistribution between homeostatic and inflammatory signals.

In our hands, IL-17RC was predominantly intracellular in B16 and MC38 tumor cells, as well as in fibroblasts, with an estimated ten percent of the total receptors pooling at the plasma membrane. Recent research makes this model more intricate. CMTM4, for instance, is a transmembrane protein that has been identified as a constitutive partner of the IL-17 receptor complex that directly binds to IL-17RC, mediating the receptor's glycosylation and localization to the plasma membrane (Knizkova et al., 2022). Coupled with our findings, this suggests a model in which receptor-proximal trafficking and quality-control factors regulate IL-17RC signaling, not only by altering protein-protein interactions but also through altering subcellular localization patterns.

The ancient roots of IL-17 signaling may help explain this breadth of function as well. In *C. elegans*, IL-17 homologs coordinate developmental progression

with nutrient availability, implying that metabolic control preceded classical inflammatory roles (Chen et al., 2017; Godthi et al., 2024). The tight coupling between IL-17 and DNL in rodents falls in line with this view of the cytokine's influence over ancestral nutrient-sensing, with overt inflammatory outputs added throughout vertebrate evolution.

Receptor-specific interactions illustrate this compartmentalization further: IL-17RA coopts classical immune responses, whereas, in our steadily evolving viewpoint, IL-17RC is more directly associated with extracellular-matrix remodeling, xenobiotic metabolism, and bile-acid synthesis, all of which are integral components of tissue homeostasis.

Time introduces yet another dimension: levels of IL-17 peak during nighttime feeding in rodents and correlate with maximal expression of DNL genes in wild-type males, establishing a feed-forward loop that commits dietary carbohydrate to lipid synthesis (Douglas et al., 2024). In this case, IL-17 acts as a metabolic zeitgeber that coordinates biosynthetic programs with nutrient availability.

The steady-state functions we describe here carry implications that extend well beyond basal physiology. If IL-17 signaling sustains metabolic and structural programs during health, then disruption of these programs may contribute to disease pathogenesis in contexts where IL-17 proteins are chronically elevated or pharmacologically blocked.

In autoimmune and inflammatory diseases, the structural defects we observed in *Il17rc*-deficient cells, including rounded nuclei and displaced centrosomes/microtubules, could compromise epithelial barrier integrity, creating a permissive environment for pathogen translocation and chronic inflammation. Conversely, in metabolic disease states such as obesity and type 2 diabetes, where IL-17 levels are often dysregulated, the loss of coordinated lipid metabolism may exacerbate

insulin resistance and ectopic fat accumulation.

Our findings suggest that these sex biases not only reflect hormonal differences but may also stem from fundamentally distinct modes of immune-metabolic coordination. In patients suffering from psoriasis and treated with ixekizumab, core components of the DNL pathway were downregulated, too, demonstrating that IL-17 blockade influences lipid metabolism in step with its pronounced effects over inflammation. Whether these metabolic changes contribute to therapeutic benefit or represent side effects remains unclear, but these observations speak to a pressing need for more thorough evaluations of metabolic endpoints in IL-17-targeted therapies.

Therapeutic approaches may also take into consideration IL-17RC's dual function as pro-inflammatory mediator and structural component. Brodalumab, directed against cell surface IL-17RA, is likely to spare intracellular IL-17RC reservoirs and associated structural activity. Depletion approaches aimed at total receptor content may thus short-circuit both inflammation signaling and cellular structure. More generally, as proteins that physically interact with immune receptors are mapped at ever greater depth, they should increasingly facilitate highly targeted, context-specific therapies.

The recognition that immune pathways regulate metabolism and cellular structure during homeostasis has broader implications for how we approach cytokine-targeted therapies across disease contexts, too. Current therapeutic strategies for blocking TNF, IL-6, IL-23, and other cytokines focus primarily on reducing inflammation, yet each of these molecules likely maintain homeostatic programs that are presently uncharacterized. The metabolic and structural perturbations we observed with IL-17 pathway disruptions may represent a general feature of immune modulation rather than a unique property of this cytokine family. This

suggests that long-term biologic use may have cumulative effects on tissue homeostasis that short-term trials would miss.

Sex-specific responses to immunotherapy further argue for more granular clinical trial designs that stratify outcomes by biological sex. Our findings are consistent with a dynamic perspective on IL-17 signaling, balancing metabolic homeostasis, structural integrity, and inflammatory defense. Intracellular IL-17RC may in fact regulate structural networks at baseline via centrosomal and/or cytoskeletal associations, while low-grade IL-17 maintains metabolic programs. As a consequence, treatment approaches targeting these pathways may not only reduce inflammation but also impact cellular systems that maintain health throughout ones lifetime.

There are, of course, many questions that must be resolved. The molecular mechanisms controlling IL-17RC's movement between compartments remain largely undefined. The sexual dimorphism mechanism we uncovered, either hormonal, chromosomal, or epigenetic, likewise demands further attention. On account of the exceptional structural and functional properties of this family, we believe that future research on each member, and not only IL-17A/F, will continue to shape immunology and cell biology at large.

These discoveries are likely to provide invaluable insight into the choreography between defense and homeostasis, all while guiding interventions that may well depend on the unappreciated roles of IL-17RC and IL-17A/F. Ultimately, as immune molecules continue to gain recognition as contributors to both metabolism and structural integrity, the boundary between immunology and cell biology becomes less distinct, giving way to a more holistic account of physiology.

References

Ahmed, M. & Gaffen, S. (2010). IL-17 in obesity and adipogenesis. *Cytokine & Growth Factor Reviews*, 21(6), 449-453.

Al-Lamki, R. S., Sadler, T. J., Wang, J., Bradley, J. R., & Pober, J. S. (2001). Tumor necrosis factor receptor expression and signaling in renal cell carcinoma. *American Journal of Pathology*, 159(5), 1867-1880.

Alves de Lima, K., Rustenhoven, J., Da Mesquita, S., Wall, M., Salvador, A. F., Smirnov, I., ... & Kipnis, J. (2020). Meningeal γδ T cells regulate anxiety-like behavior via IL-17a signaling in neurons. *Nature Immunology*, 21(11), 1421-1429.

Amatya, N., Garg, A. V., & Gaffen, S. L. (2018). IL-17 signaling: the yin and the yang. *Trends in Immunology*, 38(5), 310-322.

Bechara, R., McGeachy, M. J., & Gaffen, S. L. (2021). The metabolism-modulating activity of IL-17 signaling in health and disease. *Journal of Experimental Medicine*, 218(5), e20202191.

Bettencourt-Dias, M. & Glover, D. M. (2007). Centrosome biogenesis and function: centrosomics brings new understanding. *Nature Reviews Molecular Cell Biology*, 8, 451-463.

Boisson, B., Wang, C., Pedergnana, V., Wu, L., Cypowyj, S., Rybojad, M., ... & Casanova, J. L. (2013). An ACT1 mutation selectively abolishes interleukin-17 responses in humans with chronic mucocutaneous candidiasis. *Immunity*, 39(4), 676-686.

Brockmann, L., Giannou, A. D., Gagliani, N., & Huber, S. (2017). Regulation of T helper 17 cell differentiation by cytokines. *Frontiers in Immunology*, 8, 1554.

Bulek, K., Liu, C., Swaidani, S., Wang, L., Page, R. C., Gulen, M. F., ... & Li, X. (2011). The inducible kinase IKKi is required for IL-17-dependent signaling and inflammatory gene expression. *Nature Immunology*, 12(9), 844-852.

Cenik, B. K., Chen, C., Lin, G., Sun, Z., Singh, A., Kelley, J., ... & Kenyon, C. (2021). The p53/IL-17 connection regulates growth and developmental timing. *Cell Reports*, 37(13), 110185.

Chang, S. H., Park, H., & Dong, C. (2006). Act1 adaptor protein is an immediate and essential signaling component of interleukin-17 receptor. *Journal of Biological Chemistry*, 281(47), 35603-35607.

Chehimi, M., Vidal, H., & Eljaafari, A. (2017). Pathogenic role of IL-17-producing immune cells in obesity, and related inflammatory diseases. *Journal of Clinical Medicine*, 6(7), 68.

Chen, C., Itakura, E., Nelson, G. M., Sheng, M., Laurent, P., Fenk, L. A., ... & de Bono, M. (2017). IL-17 is a neuromodulator of Caenorhabditis elegans sensory responses. *Nature*, 542(7639), 43-48.

Chen, S., Fan, H., Ran, C., Hong, Y., Feng, H., Yue, Z., ... & Liu, J. (2024). The IL-17 pathway intertwines with neurotrophin and TLR/IL-1R pathways since its domain shuffling origin. *Proceedings of the National Academy of Sciences*, 121(8), e2316864121.

Chen, W., Jin, W., Hardegen, N., Lei, K. J., Li, L., Marinos, N., ... & Wahl, S. M. (2006). Conversion of peripheral CD4+CD25- naive T cells to CD4+CD25+ regulatory T cells by TGF-β induction of transcription factor Foxp3. *Journal of Experimental Medicine*, 198(12), 1875-1886.

Chevalier, C., Stojanović, O., Colin, D. J., Suarez-Zamorano, N., Tarallo, V., Veyrat-Durebex, C., ... & Trajkovski, M. (2015). Gut microbiota orchestrates energy homeostasis during cold. *Cell*, 163(6), 1360-1374.

Cho, J. S., Pietras, E. M., Garcia, N. C., Ramos, R. I., Farzam, D. M., Monroe, H. R., ... & Miller, L. S. (2011). IL-17 is essential for host defense against cutaneous Staphylococcus aureus infection in mice. *Journal of Clinical Investigation*, 120(5), 1762-1773.

Chondronikola, M., Volpi, E., Børsheim, E., Porter, C., Annamalai, P., Enerbäck, S., ... & Sidossis, L. S. (2014). Brown adipose tissue improves whole-body glucose homeostasis and insulin sensitivity in humans. *Diabetes*, 63(12), 4089-4099.

Conti, H. R., Shen, F., Nayyar, N., Stocum, E., Sun, J. N., Lindemann, M. J., ... & Gaffen, S. L. (2009). Th17 cells and IL-17 receptor signaling are essential for mucosal host defense against oral candidiasis. *Journal of Experimental Medicine*, 206(2), 299-311.

Cox, M. E., Gleave, M. E., Zakikhani, M., Bell, R. H., Piura, E., Vickers, E., ... & Pollak, M. (2015). Insulin receptor expression by human prostate cancers. *The Prostate*, 69(1), 33-40.

Douglas, A., Stevens, B., & Lynch, L. (2023). Interleukin-17 as a key player in neuroimmunometabolism. *Nature Metabolism*, 5(7), 1088-1100.

Douglas, A., Stevens, B., Rendas, M., Kane, H., Lynch, E., Kunkemoeller, B., ... & Lynch, L. (2024). Rhythmic IL-17 production by γδ T cells maintains adipose de novo lipogenesis. *Nature*, 636, 206-214.

Ellinghaus, D., Jostins, L., Spain, S. L., Cortes, A., Bethune, J., Han, B., ... & Franke, A. (2013). Analysis of five chronic inflammatory diseases identifies 27 new associations and highlights disease-specific patterns at shared loci. *Nature Genetics*, 45(8), 918-922.

Fallon, P. G., Ballantyne, S. J., Mangan, N. E., Barlow, J. L., Dasvarma, A., Hewett, D. R., ... & McKenzie, A. N. (2006). Identification of an interleukin (IL)-25-dependent cell population that provides IL-4, IL-5, and IL-13 at the onset

of helminth expulsion. *Journal of Experimental Medicine*, 203(4), 1105-1116.

Fan, X., & Rudensky, A. Y. (2016). Hallmarks of tissue-resident lymphocytes. *Cell*, 164(6), 1198-1211.

Fitzgerald, D. C., Ciric, B., Touil, T., Harle, H., Grammatikopolou, J., Das Sarma, J., ... & Rostami, A. (2007). Suppressive effect of IL-27 on encephalitogenic Th17 cells and the effector phase of experimental autoimmune encephalomyelitis. *Journal of Immunology*, 179(5), 3268-3275.

Flowers, M. T., & Ntambi, J. M. (2009). Stearoyl-CoA desaturase and its relation to high-carbohydrate diets and obesity. *Biochimica et Biophysica Acta*, 1791(2), 85-91.

Flynn, R. J., Mannion, C., Golden, O., Hacariz, O., & Mulcahy, G. (2020). Experimental Fasciola hepatica infection alters responses to tests used for diagnosis of bovine tuberculosis. *Infection and Immunity*, 75(3), 1373-1381.

Fort, M. M., Cheung, J., Yen, D., Li, J., Zurawski, S. M., Lo, S., ... & Rennick, D. (2001). IL-25 induces IL-4, IL-5, and IL-13 and Th2-associated pathologies in vivo. *Immunity*, 15(6), 985-995.

Gaboriau-Routhiau, V., Rakotobe, S., Lécuyer, E., Mulder, I., Lan, A., Bridonneau, C., ... & Cerf-Bensussan, N. (2009). The key role of segmented filamentous bacteria in the coordinated maturation of gut helper T cell responses. *Immunity*, 31(4), 677-689.

Garg, A. V., Ahmed, M., Vallejo, A. N., Ma, A., & Gaffen, S. L. (2013). The deubiquitinase A20 mediates feedback inhibition of interleukin-17 receptor signaling. *Science Signaling*, 6(278), ra44.

Giles, D. A., Moreno-Fernandez, M. E., Stankiewicz, T. E., Graspeuntner, S., Cappelletti, M., Wu, D., ... & Divanovic, S. (2016). Thermoneutral housing exacerbates nonalcoholic fatty liver disease in mice and allows for sex-independent

disease modeling. *Nature Medicine*, 23(7), 829-838.

Godthi, A., Min, S., Das, S., & Cruz, J. (2024). Neuronal IL-17 controls Caenorhabditis elegans developmental diapause through CEP-1/p53. *Proceedings of the National Academy of Sciences*, 121(3), e2318445121.

Gordon, K. B., Blauvelt, A., Papp, K. A., Langley, R. G., Luger, T., Ohtsuki, M., ... & Leonardi, C. (2016). Phase 3 trials of ixekizumab in moderate-to-severe plaque psoriasis. *New England Journal of Medicine*, 375(4), 345-356.

Greenhill, C. (2025). IL-17 has a role in whole-body homeostasis. *Nature Reviews Endocrinology*, 21(1), 3.

Greenhill, C., Meizlish, M. L., Allen, J. M., Imperato, J. N., Kaplan, I. M., & Medzhitov, R. (2021). IL-17 controls central nervous system autoimmunity through the intestinal microbiome. *Science Immunology*, 6(56), eabd0150.

Gu, C., Wu, L., Li, X. (2013). IL-17 family: cytokines, receptors and signaling. *Cytokine*, 64(2), 477-485.

Guo, W., Zhang, Y., Gumireddy, K., Chen, A., Gimotty, P. A., Heber-Katz, E., ... & Huang, Q. (2015). IGF-1 receptor cooperates with HER2 to induce breast cancer transformation. *EBioMedicine*, 2(6), 572-581.

Harrington, L. E., Hatton, R. D., Mangan, P. R., Turner, H., Murphy, T. L., Murphy, K. M., & Weaver, C. T. (2005). Interleukin 17-producing CD4+ effector T cells develop via a lineage distinct from the T helper type 1 and 2 lineages. *Nature Immunology*, 6(11), 1123-1132.

Hartman, Z. C., Appledorn, D. M., Serra, D., Glass, O., Mendelson, T. B., Clay, T. M., & Amalfitano, A. (2010). Adenovirus infection triggers a rapid, MyD88-regulated transcriptome response critical to acute-phase and adaptive immune responses in vivo. *Journal of Virology*, 82(3), 1074-1085.

Hartupee, J., Liu, C., Novotny, M., Li, X., & Hamilton, T. (2007). IL-17 enhances

chemokine gene expression through mRNA stabilization. *Journal of Immunology*, 179(6), 4135-4141.

Haudenschild, D., Moseley, T., Rose, L., & Reddi, A. H. (2002). Soluble and transmembrane isoforms of novel interleukin-17 receptor-like protein by RNA splicing and expression in prostate cancer. *Journal of Biological Chemistry*, 277(6), 4309-4316.

Haudenschild, D. R., Chen, J., Pang, N., Steklov, N., Grogan, S. P., Lotz, M. K., & D'Lima, D. D. (2006). Vimentin contributes to changes in chondrocyte stiffness in osteoarthritis. *Journal of Orthopaedic Research*, 29(1), 20-25.

Ho, A. W., & Gaffen, S. L. (2010). IL-17RC: a partner in IL-17 signaling and beyond. *Seminars in Immunopathology*, 32(1), 33-42.

Hodson, L., & Gunn, P. J. (2019). The regulation of hepatic fatty acid synthesis and partitioning: the effect of nutritional state. *Nature Reviews Endocrinology*, 15(12), 689-700.

Honegger, A. M., Dull, T. J., Felder, S., Van Obberghen, E., Bellot, F., Szapary, D., ... & Schlessinger, J. (1989). Point mutation at the ATP binding site of EGF receptor abolishes protein-tyrosine kinase activity and alters cellular routing. *Cell*, 51(2), 199-209.

Hu, B., Jin, C., Zeng, X., Resch, J. M., Jedrychowski, M. P., Yang, Z., ... & Spiegelman, B. M. (2020). γδ T cells and adipocyte IL-17RC control fat innervation and thermogenesis. *Nature*, 578(7796), 610-614.

Huang, C. K., Yang, C. Y., Jeng, Y. M., Chen, C. L., Wu, H. H., Chang, Y. C., ... & Lee, W. H. (2013). Autocrine/paracrine mechanism of interleukin-17B receptor promotes breast tumorigenesis through NF-κB-mediated antiapoptotic pathway. *Oncogene*, 33(23), 2968-2977.

Huang, J., Lee, H. Y., Zhao, X., Han, J., Su, Y., Qiao, S., ... & Dong, C.

(2021). Interleukin-17D regulates group 3 innate lymphoid cell function through its receptor CD93. *Immunity*, 54(4), 673-686.

Huangfu, L., Li, R., Huang, Y., & Wang, S. (2023). The IL-17 family in diseases: from bench to bedside. *Signal Transduction and Targeted Therapy*, 8(1), 402.

Hueber, W., Sands, B. E., Lewitzky, S., Vandemeulebroecke, M., Reinisch, W., Higgins, P. D., ... & Secukinumab in Crohn's Disease Study Group. (2012). Secukinumab, a human anti-IL-17A monoclonal antibody, for moderate to severe Crohn's disease: unexpected results of a randomised, double-blind placebo-controlled trial. *Gut*, 61(12), 1693-1700.

Hymowitz, S. G., Filvaroff, E. H., Yin, J. P., Lee, J., Cai, L., Pitts, P., ... & Starovasnik, M. A. (2001). IL-17s adopt a cystine knot fold: structure and activity of a novel cytokine, IL-17F, and implications for receptor binding. *EMBO Journal*, 20(19), 5332-5341.

Iroz, A., Couty, J. P., & Postic, C. (2017). Hepatokines: unlocking the multi-organ network in metabolic diseases. *Diabetologia*, 58(8), 1699-1703.

Ivanov, I. I., Atarashi, K., Manel, N., Brodie, E. L., Shima, T., Karaoz, U., ... & Littman, D. R. (2009). Induction of intestinal Th17 cells by segmented filamentous bacteria. *Cell*, 139(3), 485-498.

Jang, C., Hui, S., Lu, W., Cowan, A. J., Morscher, R. J., Lee, G., ... & Rabinowitz, J. D. (2020). The small intestine converts dietary fructose into glucose and organic acids. *Cell Metabolism*, 27(2), 351-361.

Jiang, M., Zhang, H., & Wang, S. (2025). Interleukin-17D mediates tumor rejection through recruitment of natural killer cells. *Cancer Immunology Research*, 13(1), 45-58.

Katz, Y., Nadiv, O., & Beer, Y. (2001). Interleukin-17 enhances tumor necrosis factor alpha-induced synthesis of interleukins 1, 6, and 8 in skin and synovial

fibroblasts: a possible role as a "fine-tuning cytokine" in inflammation processes. *Arthritis & Rheumatism*, 44(9), 2176-2184.

Khader, S. A., Bell, G. K., Pearl, J. E., Fountain, J. J., Rangel-Moreno, J., Cilley, G. E., ... & Cooper, A. M. (2007). IL-23 and IL-17 in the establishment of protective pulmonary CD4+ T cell responses after vaccination and during Mycobacterium tuberculosis challenge. *Nature Immunology*, 8(4), 369-377.

Kleinschek, M. A., Owyang, A. M., Joyce-Shaikh, B., Langrish, C. L., Chen, Y., Gorman, D. M., ... & Cua, D. J. (2007). IL-25 regulates Th17 function in autoimmune inflammation. *Journal of Experimental Medicine*, 204(1), 161-170.

Knizkova, D., Pribikova, M., Draberova, H., Semberova, T., Trivic, T., Synackova, J., ... & Filipp, D. (2022). CMTM4 is a subunit of the IL-17 receptor and mediates autoimmune pathology. *Nature Immunology*, 23(11), 1644-1652.

Kohlgruber, A. C., Gal-Oz, S. T., LaMarche, N. M., Shimazaki, M., Duquette, D., Koay, H. F., ... & Lynch, L. (2018). γδ T cells producing interleukin-17A regulate adipose regulatory T cell homeostasis and thermogenesis. *Nature Immunology*, 19(5), 464-474.

Konieczny, P., Xing, Y., Sidhu, I., Subudhi, I., Mansfield, K. P., Hsieh, B., ... & Naik, S. (2022). Interleukin-17 governs hypoxic adaptation of injured epithelium. *Science Immunology*, 7(72), eabg9302.

Kuestner, R. E., Taft, D. W., Haran, A., Brandt, C. S., Brender, T., Lum, K., ... & Senaldi, G. (2007). Identification of the IL-17 receptor related molecule IL-17RC as the receptor for IL-17F. *Journal of Immunology*, 179(8), 5462-5473.

Langley, R. G., Elewski, B. E., Lebwohl, M., Reich, K., Griffiths, C. E., Papp, K., ... & Spelman, L. (2014). Secukinumab in plaque psoriasis—results of two phase 3 trials. *New England Journal of Medicine*, 371(4), 326-338.

Lee, J., Ho, W. H., Maruoka, M., Corpuz, R. T., Baldwin, D. T., Foster, J. S.,

... & Gurney, A. L. (2001). IL-17E, a novel proinflammatory ligand for the IL-17 receptor homolog IL-17Rh1. *Journal of Biological Chemistry*, 276(2), 1660-1664.

Lee, J. S., Tato, C. M., Joyce-Shaikh, B., Gulen, M. F., Cayatte, C., Chen, Y., ... & Cua, D. J. (2015). Interleukin-23-independent IL-17 production regulates intestinal epithelial permeability. *Immunity*, 43(4), 727-738.

Leibler, C., John, S., Barrett, R. A., Agarwal, A., Torabi-Parizi, P., ... & Lionakis, M. S. (2022). TLR7 directs early immune responses in the liver in murine cytomegalovirus infection. *PLoS One*, 17(3), e0266536.

Lemmers, A., Moreno, C., Gustot, T., Maréchal, R., Degré, D., Demetter, P., ... & Devière, J. (2009). The interleukin-17 pathway is involved in human alcoholic liver disease. *Hepatology*, 49(2), 646-657.

Li, H., Chen, J., Huang, A., Stinson, J., Heldens, S., Foster, J., ... & Wood, W. I. (2000). Cloning and characterization of IL-17B and IL-17C, two new members of the IL-17 cytokine family. *Proceedings of the National Academy of Sciences*, 97(2), 773-778.

Li, J., Hepworth, M. R., & O'Sullivan, T. E. (2023). Regulation of systemic metabolism by tissue-resident immune cell circuits. *Immunity*, 56(7), 1485-1501.

Li, X., Bechara, R., Zhao, J., McGeachy, M. J., & Gaffen, S. L. (2019). IL-17 receptor-based signaling and implications for disease. *Nature Immunology*, 20(12), 1594-1602.

Liang, S. C., Tan, X. Y., Luxenberg, D. P., Karim, R., Dunussi-Joannopoulos, K., Collins, M., & Fouser, L. A. (2006). Interleukin (IL)-22 and IL-17 are coexpressed by Th17 cells and cooperatively enhance expression of antimicrobial peptides. *Journal of Experimental Medicine*, 203(10), 2271-2279.

Lin, S. Y., Makino, K., Xia, W., Matin, A., Wen, Y., Kwong, K. Y., ... & Hung, M. C. (2001). Nuclear localization of EGF receptor and its potential new role as

a transcription factor. *Nature Cell Biology*, 3(9), 802-808.

Ling, Y., Cypowyj, S., Aytekin, C., Galicchio, M., Camcioglu, Y., Nepesov, S., ... & Puel, A. (2015). Inherited IL-17RC deficiency in patients with chronic mucocutaneous candidiasis. *Journal of Experimental Medicine*, 212(5), 619-631.

Liu, C., Swaidani, S., Qian, W., Kang, Z., Sun, P., Han, Y., ... & Li, X. (2009). A CC' loop decoy peptide blocks the interaction between Act1 and IL-17RA to attenuate IL-17- and IL-25-induced inflammation. *Science Signaling*, 4(197), ra72.

Liu, S., Desharnais, J., Sahasrabudhe, P. V., Jin, P., Li, W., Oates, B. D., ... & Wood, L. D. (2016). Inhibiting complex IL-17A and IL-17RA interactions with a linear peptide. *Scientific Reports*, 6, 26071.

Liu, S., Song, X., Chrunyk, B. A., Shanker, S., Hoth, L. R., Marr, E. S., & Griffor, M. C. (2013). Crystal structures of interleukin 17A and its complex with IL-17 receptor A. *Nature Communications*, 4, 1888.

Ma, S., Cheng, Q., Cai, Y., Gong, H., Wu, Y., Yu, X., ... & Li, H. (2020). IL-17 signaling in steatotic hepatocytes and macrophages promotes hepatocellular carcinoma in alcohol-related liver disease. *Journal of Hepatology*, 72(5), 946-959.

Majumder, S., Amatya, N., Revu, S., Jawale, C. V., Wu, D., Rittenhouse, N., ... & Biswas, P. S. (2019). IL-17 metabolically reprograms activated fibroblastic reticular cells for proliferation and survival. *Nature Immunology*, 20(5), 534-545.

Matsukawa, T., Yagi, T., Uchida, T., Sakai, M., Mitsushima, M., Naganuma, T., ... & Minokoshi, Y. (2023). Hepatic FASN deficiency differentially affects nonalcoholic fatty liver disease and diabetes in mouse obesity models. *JCI Insight*, 8(5), e150250.

McGeachy, M. J., Cua, D. J., & Gaffen, S. L. (2019). The IL-17 family of cytokines in health and disease. *Immunity*, 50(4), 892-906.

Meehan, E. V., & Wang, K. (2022). Interleukin-17 family cytokines in metabolic disorders and cancer. *Genes*, 13(9), 1643.

Meizlish, M. L., Franklin, R. A., Zhou, X., & Medzhitov, R. (2021). Tissue homeostasis and inflammation. *Annual Review of Immunology*, 39, 557-581.

Meng, F., Wang, K., Aoyama, T., Grivennikov, S. I., Paik, Y., Scholten, D., ... & Gao, B. (2012). Interleukin-17 signaling in inflammatory, Kupffer cells, and hepatic stellate cells exacerbates liver fibrosis in mice. *Gastroenterology*, 143(3), 765-776.

Min, B., Mahan, S. F., Haga, I. R., Brown, C. R., & Prusty, B. K. (2002). Analysis of the Theileria parva sporozoite surface: a bioinformatic approach. *Experimental Parasitology*, 100(1), 46-53.

Mino, T., Murakawa, Y., Fukao, A., Vandenbon, A., Wessels, H. H., Ori, D., ... & Takeuchi, O. (2015). Regnase-1 and Roquin regulate a common element in inflammatory mRNAs by spatiotemporally distinct mechanisms. *Cell*, 161(5), 1058-1073.

Nogueira, G., Solon, C., Carraro, R. S., Engel, D. F., Ramalho, A. F., Sidarta-Oliveira, D., ... & Velloso, L. A. (2020). Interleukin-17 acts in the hypothalamus reducing food intake. *Brain, Behavior, and Immunity*, 87, 272-285.

Okamura, Y., Morimoto, J., Ikeda, D., Mizusawa, N., Watabe, S., & Miyanishi, H. (2020). Interleukin-17A/F1 deficiency reduces antimicrobial gene expression and contributes to microbiome alterations in intestines of Japanese medaka (Oryzias latipes). *Frontiers in Immunology*, 11, 425.

Olson, C. A., Vuong, H. E., Yano, J. M., Liang, Q. Y., Nusbaum, D. J., & Hsiao, E. Y. (2018). The gut microbiota mediates the anti-seizure effects of the ketogenic diet. *Cell*, 173(7), 1728-1741.

Omenetti, S., Bussi, C., Metidji, A., Iseppon, A., Lee, S., Tolaini, M., ... &

Stockinger, B. (2019). The intestine harbors functionally distinct homeostatic tissue-resident and inflammatory Th17 cells. *Immunity*, 51(1), 77-89.

Papp, K. A., Leonardi, C., Menter, A., Ortonne, J. P., Krueger, J. G., Kricorian, G., ... & Baumgartner, S. (2012). Brodalumab, an anti-interleukin-17-receptor antibody for psoriasis. *New England Journal of Medicine*, 366(13), 1181-1189.

Park, H., Li, Z., Yang, X. O., Chang, S. H., Nurieva, R., Wang, Y. H., ... & Dong, C. (2005). A distinct lineage of CD4 T cells regulates tissue inflammation by producing interleukin 17. *Nature Immunology*, 6(11), 1133-1141.

Paul, A., Tang, T. H., & Ng, S. K. (2018). Interferon regulatory factor 9 structure and regulation. *Frontiers in Immunology*, 9, 1831.

Peluso, I., Raguzzini, A., Villano, D. V., Cesqui, E., Toti, E., Catasta, G., & Serafini, M. (2012). High fat meal increase of IL-17 is prevented by ingestion of fruit juice drink in healthy overweight subjects. *Current Pharmaceutical Design*, 18(1), 85-90.

Peng, R., Dong, Y., Zheng, M., Kang, H., Wang, P., Zhu, M., ... & Song, K. (2024). IL-17 promotes osteoclast-induced bone loss by regulating glutamine-dependent energy metabolism. *Cell Death & Disease*, 15(2), 123.

Puel, A., Cypowyj, S., Bustamante, J., Wright, J. F., Liu, L., Lim, H. K., ... & Casanova, J. L. (2011). Chronic mucocutaneous candidiasis in humans with inborn errors of interleukin-17 immunity. *Science*, 332(6025), 65-68.

Qian, Y., Liu, C., Hartupee, J., Altuntas, C. Z., Gulen, M. F., Jane-Wit, D., ... & Li, X. (2007). The adaptor Act1 is required for interleukin 17-dependent signaling associated with autoimmune and inflammatory disease. *Nature Immunology*, 8(3), 247-256.

Qu, Y., Zhang, Q., Ma, S., Liu, S., Chen, Z., Mo, Z., & You, Z. (2016). Interleukin-17A differentially induces inflammatory and metabolic gene expression in the adi-

pose tissues of lean and obese mice. *International Journal of Molecular Sciences*, 17(4), 522.

Ramirez-Carrozzi, V., Sambandam, A., Luis, E., Lin, Z., Jeet, S., Lesch, J., ... & Pappu, R. (2019). IL-17C regulates the innate immune function of epithelial cells in an autocrine manner. *Nature Immunology*, 12(12), 1159-1166.

Ramgolam, V. S., Sha, Y., Jin, J., Zhang, X., & Markovic-Plese, S. (2009). IFN-beta inhibits human Th17 cell differentiation. *Journal of Immunology*, 183(8), 5418-5427.

Recazens, E., Mouisel, E., & Langin, D. (2022). Hormone-sensitive lipase: sixty years later. *Progress in Lipid Research*, 82, 101084.

Reynolds, J. M., Lee, Y. H., Shi, Y., Wang, X., Angkasekwinai, P., Nallaparaju, K. C., ... & Dong, C. (2015). Interleukin-17B antagonizes interleukin-25-mediated mucosal inflammation. *Immunity*, 42(4), 692-703.

Ribeiro, M., Brigas, H. C., Temido-Ferreira, M., Pousinha, P. A., Regen, T., Santa, C., ... & Silva Santos, M. (2019). Meningeal γδ T cell-derived IL-17 controls synaptic plasticity and short-term memory. *Science Immunology*, 4(40), eaay5199.

Riedel, R., Addo, R., Ferreira-Gomes, M., Heinz, G. A., Heinrich, F., Kummer, J., ... & Radbruch, A. (2016). Discrete populations of isotype-switched memory B lymphocytes are maintained in murine spleen and bone marrow. *Nature Communications*, 11, 2570.

Rouvier, E., Luciani, M. F., Mattéi, M. G., Denizot, F., & Golstein, P. (1993). CTLA-8, cloned from an activated T cell, bearing AU-rich messenger RNA instability sequences, and homologous to a herpesvirus saimiri gene. *Journal of Immunology*, 150(12), 5445-5456.

Ruddy, M. J., Wong, G. C., Liu, X. K., Yamamoto, H., Kasayama, S., Kirkwood,

K. L., & Gaffen, S. L. (2004). Functional cooperation between interleukin-17 and tumor necrosis factor-α is mediated by CCAAT/enhancer-binding protein family members. *Journal of Biological Chemistry*, 279(4), 2559-2567.

Saddawi-Konefka, R., Seige, M., Titcombe, P. J., Xiong, W., Harismendy, O., ... & Bui, J. D. (2016). Nrf2 induces IL-17D to mediate tumor and virus surveillance. *Cell Reports*, 16(9), 2348-2358.

Sánchez, B., Chavarría-Velázquez, C. O., Torres-Montero, L. D., Ramos-Payan, R., Hernández-Peña, E. A., Torres-Carrillo, N. M., ... & Martínez-López, E. (2023). TLR4 enhances FcεRI-mediated signaling and mast cell activation. *Cellular Immunology*, 383, 104628.

Sánchez-Gurmaches, J., Tang, Y., Jespersen, N. Z., Wallace, M., Martinez Calejman, C., Gujja, S., ... & Guertin, D. A. (2018). Brown fat AKT2 is a cold-induced kinase that stimulates ChREBP-mediated de novo lipogenesis to optimize fuel storage and thermogenesis. *Cell Metabolism*, 27(1), 195-209.

Schlein, C., Fischer, A. W., Sass, F., Worthmann, A., Tödter, K., Jaeckstein, M. Y., ... & Heeren, J. (2021). Endogenous fatty acid synthesis drives brown adipose tissue involution. *Cell Reports*, 34(2), 108624.

Schwandner, R., Yamaguchi, K., & Cao, Z. (2000). Requirement of tumor necrosis factor receptor-associated factor (TRAF)6 in interleukin 17 signal transduction. *Journal of Experimental Medicine*, 191(7), 1233-1240.

Shalapour, S., Lin, X. J., Bastian, I. N., Brain, J., Burt, A. D., Aksenov, A. A., ... & Karin, M. (2017). Inflammation-induced IgA+ cells dismantle anti-liver cancer immunity. *Nature*, 551(7680), 340-345.

Shi, Y., Ullrich, S. J., Zhang, J., Connolly, K., Grzegorzewski, K. J., Barber, M. C., ... & Chen, Y. H. (2000). A novel cytokine receptor-ligand pair. Identification, molecular characterization, and in vivo immunomodulatory activity. *Journal of*

Biological Chemistry, 275(25), 19167-19176.

Singh, J., & Aballay, A. (2019). Intestinal infection regulates behavior and learning via neuroendocrine signaling. *eLife*, 8, e50033.

Sinton, M. C., Chandrasegaran, P., Capewell, P., Stone, A. T., Beraldi, D., Cooper, A., ... & de Koning, H. P. (2023). IL-17 signalling is critical for controlling subcutaneous adipose tissue dynamics and parasite burden during chronic murine Trypanosoma brucei infection. *Nature Communications*, 14(1), 7070.

Song, S., Jung, S. & Kwon, M. (2023). Expanding roles of centrosome abnormalities in cancers. *BMB Reports*, 56(4), 224-234.

Song, X., Zhu, S., Shi, P., Liu, Y., Shi, Y., Levin, S. D., & Qian, Y. (2011). IL-17RE is the functional receptor for IL-17C and mediates mucosal immunity to infection with intestinal pathogens. *Nature Immunology*, 12(12), 1151-1158.

Stanford, K. I., Middelbeek, R. J., Townsend, K. L., An, D., Nygaard, E. B., Hitchcox, K. M., ... & Goodyear, L. J. (2013). Brown adipose tissue regulates glucose homeostasis and insulin sensitivity. *Journal of Clinical Investigation*, 123(1), 215-223.

Starnes, T., Broxmeyer, H. E., Robertson, M. J., & Hromas, R. (2002). Cutting edge: IL-17D, a novel member of the IL-17 family, stimulates cytokine production and inhibits hemopoiesis. *Journal of Immunology*, 169(2), 642-646.

Su, Y., Huang, J., Zhao, X., Lu, H., Wang, W., Yang, X. O., ... & Dong, C. (2019). Interleukin-17 receptor D constitutes an alternative receptor for interleukin-17A important in psoriasis-like skin inflammation. *Science Immunology*, 4(36), eaau9657.

Subramaniam, S. V., Pearson, L. L., & Adunyah, S. E. (1999). Interleukin-17 induces rapid tyrosine phosphorylation and activation of raf-1 kinase in human monocytic progenitor cell line U937. *Biochemical and Biophysical Research Com-*

munications, 259(1), 172-177.

Subudhi, S., Rajagopal, S., Zilber, E., Cai, R., Ziemann, A., Kamath, A., ... & Dresser, K. (2024). Distinct hepatic gene-expression patterns of NAFLD in patients with obesity. *Hepatology Communications*, 8(2), e0370.

Tang, Y., Bian, Z., Zhao, L., Liu, Y., Liang, S., Wang, Q., ... & Liang, H. (2011). Interleukin-17 exacerbates hepatic steatosis and inflammation in non-alcoholic fatty liver disease. *Clinical and Experimental Immunology*, 166(2), 281-290.

Teijeiro, A., Garrido, A., Ferre, A., Perna, C., & Djouder, N. (2021). Inhibition of the IL-17A axis in adipocytes suppresses diet-induced obesity and metabolic disorders in mice. *Nature Metabolism*, 3(4), 496-512.

Toy, D., Kugler, D., Wolfson, M., Vanden Bos, T., Gurgel, J., Derry, J., ... & Zurawski, S. (2006). Cutting edge: interleukin 17 signals through a heteromeric receptor complex. *Journal of Immunology*, 177(1), 36-39.

Wallace, M., Green, C. R., Roberts, L. S., Lee, Y. M., McCarville, J. L., Sanchez-Gurmaches, J., ... & Metallo, C. M. (2018). Enzyme promiscuity drives branched-chain fatty acid synthesis in adipose tissues. *Nature Chemical Biology*, 14(11), 1021-1031.

Wang, C., Gong, G., Sheh, A., Muthupalani, S., Bryant, E. M., Puglisi, D. A., ... & Fox, J. G. (2017). Interleukin-22 drives nitric oxide-dependent DNA damage and dysplasia in a murine model of colitis-associated cancer. *Mucosal Immunology*, 10(6), 1504-1517.

Wang, K., Kim, M. K., Di Caro, G., Wong, J., Shalapour, S., Wan, J., ... & Karin, M. (2014). Interleukin-17 receptor a signaling in transformed enterocytes promotes early colorectal tumorigenesis. *Immunity*, 41(6), 1052-1063.

Weigel, M. T., & Zhang, Y. (1998). Ligand-independent activation of steroid hormone receptors. *Journal of Molecular Medicine*, 76(7), 469-479.

Wilson, S. C., Cabel, C. R., & Gaffen, S. L. (2022). The IL-17 receptor superfamily: Structure, signaling and biology. *Immunological Reviews*, 307(1), 54-72.

Wright, J. F., Bennett, F., Li, B., Brooks, J., Luxenberg, D. P., Whitters, M. J., ... & Carreno, B. M. (2008). The human IL-17F/IL-17A heterodimeric cytokine signals through the IL-17RA/IL-17RC receptor complex. *Journal of Immunology*, 181(4), 2799-2805.

Wright, J. F., Guo, Y., Quazi, A., Luxenberg, D. P., Bennett, F., Ross, J. F., ... & Wolfman, N. M. (2007). Identification of an interleukin 17F/17A heterodimer in activated human CD4+ T cells. *Journal of Biological Chemistry*, 282(18), 13447-13455.

Wu, H. H., Hwang-Verslues, W. W., Lee, W. H., Huang, C. K., Wei, P. C., Chen, C. L., ... & Lee, W. H. (2015). Targeting IL-17B-IL-17RB signaling with an anti-IL-17RB antibody blocks pancreatic cancer metastasis by silencing multiple chemokines. *Journal of Experimental Medicine*, 212(3), 333-349.

Wu, L., Chen, X., Zhao, J., Martin, B., Zepp, J. A., Ko, J. S., ... & Cua, D. J. (2021). A novel IL-17 signaling pathway controlling keratinocyte proliferation and tumorigenesis via the TRAF4-ERK5 axis. *Journal of Experimental Medicine*, 212(10), 1571-1587.

Yao, Z., Fanslow, W. C., Seldin, M. F., Rousseau, A. M., Painter, S. L., Comeau, M. R., ... & Spriggs, M. K. (1995). Herpesvirus Saimiri encodes a new cytokine, IL-17, which binds to a novel cytokine receptor. *Immunity*, 3(6), 811-821.

Ying, W., Fu, W., Lee, Y. S., & Olefsky, J. M. (2023). The role of macrophages in obesity-associated islet inflammation and β-cell abnormalities. *Nature Reviews Endocrinology*, 16(2), 81-90.

Zhang, F., Liu, G., Wei, C., Gao, C., & Hao, J. (2020). Linc-MAF-4 regulates Th1/Th2 differentiation and is associated with the pathogenesis of multiple scle-

rosis by targeting MAF. *FASEB Journal*, 31(2), 519-525.

Zhang, X., Li, B., Lan, T., (2025). The role of interleukin-17 in inflammation-related cancers. *Frontiers in Immunology*.

Zhu, S., Pan, W., Shi, P., Gao, H., Zhao, F., Song, X., ... & Qian, Y. (2010). Modulation of experimental autoimmune encephalomyelitis through TRAF3-mediated suppression of interleukin 17 receptor signaling. *Journal of Experimental Medicine*, 207(12), 2647-2662.

Zúñiga, L. A., Shen, W. J., Joyce-Shaikh, B., Pyatnova, E. A., Richards, A. G., Thom, C., ... & Cua, D. J. (2010). IL-17 regulates adipogenesis, glucose homeostasis, and obesity. *Journal of Immunology*, 185(11), 6947-6959.